

# A MICROPRISM ARRAY FOR LARGE-SCALE, WIDE-BAND INTERCONNECTION OF OPTOELECTRONIC SYSTEMS

## Final Report

Period of Performance: 02-18-93 to 02-17-95

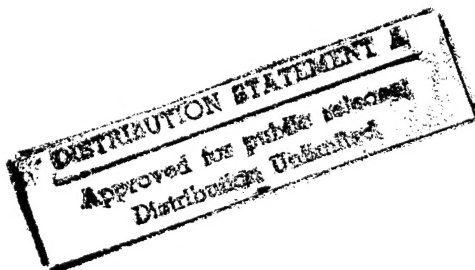
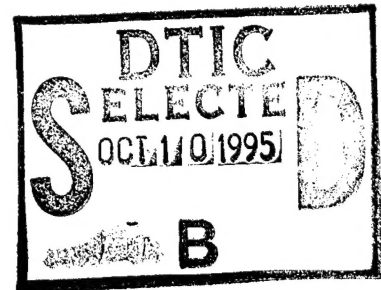
Contract No. DAAH04-93-C-0007

### Sponsored by:

U. S. Army Research Office  
P. O. Box 12211  
Research Triangle Park, NC 27709

### Technical Monitor:

Dr. James W. Mink  
(919) 549-4240



### Contractor:

Physical Optics Corporation  
Applied Technology Division  
2545 West 237th Street, Suite B  
Torrance, CA 90505

### Principal Investigator:

Tomasz Jannson, Ph.D.  
(310) 530-1416

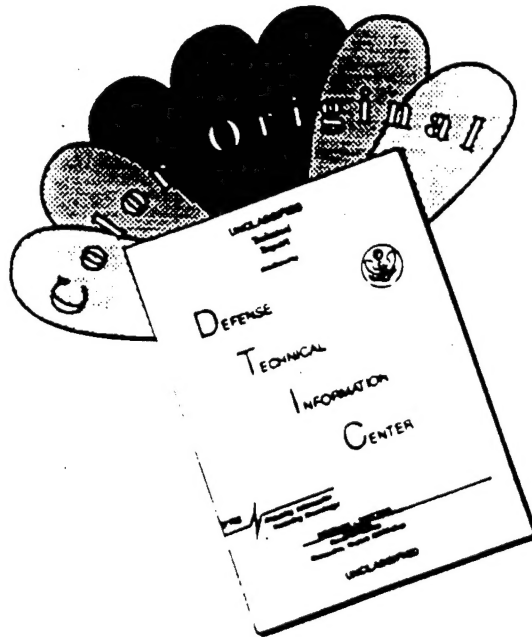
19951005 028

April 1995

DTIC QUALITY INSPECTED B

*The views, opinions and/or findings contained in this report are those of the author(s) and should not be construed as an official Department of the Army position, policy, or decision, unless so designated by other documentation.*

# DISCLAIMER NOTICE



THIS DOCUMENT IS BEST QUALITY AVAILABLE. THE COPY FURNISHED TO DTIC CONTAINED A SIGNIFICANT NUMBER OF COLOR PAGES WHICH DO NOT REPRODUCE LEGIBLY ON BLACK AND WHITE MICROFICHE.

REPORT DOCUMENTATION PAGE			Form Approved OMB No. 0704-0188	
Public reporting burden for this collection of information is estimated to average 1 hour per response, including the time for reviewing instructions, searching existing data sources, gathering and maintaining the data needed, and completing and reviewing the collection of information. Send comments regarding this burden estimate or any other aspect of this collection of information, including suggestions for reducing this burden to Washington Headquarters Services, Directorate for Information Operations and Reports, 1215 Jefferson Davis Highway, Suite 1204, Arlington, VA 22202-4302, and to the Office of Management and Budget, Paperwork Reduction Project (0704-0188), Washington, DC 20503.				
1. AGENCY USE ONLY (Leave blank)	2. REPORT DATE 4/17/95	3. REPORT TYPE AND DATES COVERED Final, 2/18/93 - 2/17/95		
4. TITLE AND SUBTITLE A Microprism Array for Large-Scale, Wide-Band Interconnection of Optoelectronic Systems		5. FUNDING NUMBERS DAAH04-93-C-0007		
6. AUTHOR(S) Tomasz Jannson, Andrew Kostrzewski, Dai Hyun Kim, Vladimir Katsman				
7. PERFORMING ORGANIZATION NAME(S) AND ADDRESS(ES) Physical Optics Corporation 2545 West 237th Street, Suite B Torrance, California 90505		8. PERFORMING ORGANIZATION REPORT NUMBER 3201		
9. SPONSORING / MONITORING AGENCY NAME(S) AND ADDRESS(ES) U. S. Army Research Office P. O. Box 12211 Research Triangle Park, NC 27709-2211		10. SPONSORING / MONITORING AGENCY REPORT NUMBER		
11. SUPPLEMENTARY NOTES The view, opinions and/or findings contained in this report are those of the author(s) and should not be construed as an official Department of the Army position, policy, or decision, unless so designated by other documentation.				
12a. DISTRIBUTION / AVAILABILITY STATEMENT  Approved for public release; distribution unlimited.		12b. DISTRIBUTION CODE		
13. ABSTRACT (Maximum 200 words) In this Phase II program, Physical Optics Corporation (POC) has completed the proposed optical communication/switching system based on a microprism array. Overall theoretical studies of various interconnect methods, such as free-space with fiber optic, free-space with diffraction elements, fiber waveguide and its coupling carried out. Additionally, microprism interconnect with dedicated packaging providing micromechanical tolerance was investigated. As specific fabrication, fiber optic free-space optical communication/switching system, a 3 x 3 microprism-based crossbar switch, was implemented. The demonstration of fan-out communication as well as channel switching were demonstrated.				
14. SUBJECT TERMS Microprism Array, Crossbar Switch, Optical Interconnect Optoelectronic System		15. NUMBER OF PAGES 76		
		16. PRICE CODE		
17. SECURITY CLASSIFICATION OF REPORT Unclassified	18. SECURITY CLASSIFICATION OF THIS PAGE Unclassified	19. SECURITY CLASSIFICATION OF ABSTRACT Unclassified	20. LIMITATION OF ABSTRACT SAR	

NSN 7540-01-280-5500

Standard Form 298 (Rev. 2-89)  
Prescribed by ANSI Std Z39-18  
298-102

## TABLE OF CONTENTS

1.0	INTRODUCTION AND EXECUTIVE SUMMARY .....	1
2.0	MICROPRISM DESIGN AND ITS PHYSICAL CHARACTERISTICS .....	1
2.1	Free-Space Microprism Interconnects .....	1
2.1.1	Free-Space Propagation of Fiber Optic Beam .....	1
2.2	Free-Space Interconnects with Diffraction (Lensing) Elements .....	4
2.3	Fiber-Waveguide Interconnection .....	7
2.3.1	Fiber-Waveguide Coupling .....	8
2.4	Microprism Interconnect with Dedicated Packaging Providing Micromechanical Tolerances .....	13
3.0	DESIGN OF THE OPTICAL INTERCONNECTION SYSTEM .....	17
3.1	Fiber Optic Free-Space Communication .....	17
3.2	Free-Space Diffractive Signal Router .....	19
4.0	DESIGN, PROTOTYPING AND OPTIMIZATION OF ELECTRONIC SYSTEM .....	20
4.1	Electronic System .....	21
4.1.1	Source Modulation .....	22
4.2	Modulator Circuit Design Considerations .....	22
4.3	Biasing Considerations .....	23
4.4	Electronic Encoder/Decoder Design .....	25
4.4.1	Data Encoding and Decoding .....	26
4.5	Transmitter Optimization .....	27
4.5.1	Simulation Analysis and Results .....	27
4.5.2	Transmitter Design Analysis .....	31
4.5.3	Experimental Setup and Results .....	32
5.0	BI-DIRECTIONAL OPTICAL BACKPLANE BUS .....	44
5.1	Fabrication Considerations for the Optical Backplane Bus .....	46
5.2	Analysis of Diffraction Conditions for the Holographic Bi-Directional Optical Backplane Bus .....	47
5.3	Optimization of the Five Channel Optical Backplane Bus .....	48
5.4	Project Specifications .....	54
5.5	Experimental Bottleneck: Minimum Modulated Input Power Required at 500 MHz .....	54
5.6	Experimental Results .....	55
6.0	DEMONSTRATION OF THE MICROPRISM ARRAY-BASED OPTOELECTRONIC INTERCONNECT SYSTEM .....	59
6.1	Fabrication of the Microprism-Based Optical Crossbar Switch .....	60
7.0	SUMMARY .....	66
8.0	REFERENCES .....	66
	APPENDIX A: FRESNEL NUMBER AND APERTURE DIFFRACTION .....	68
	APPENDIX B: INTEGRAL TRANSFORMATION FOR POYNTING VECTOR IN GEOMETRICAL OPTICS .....	69

<b>Accession For</b>	
NTIS GRA&I	<input checked="" type="checkbox"/>
DTIC TAB	<input type="checkbox"/>
Unannounced	<input type="checkbox"/>
Justification	
By	
Distribution/	
Availability Codes	
Dist	Avail and/or Special
A-1	



## LIST OF FIGURES

2-1	Illustration of Fiber-to-Fiber Coupling Geometry .....	3
2-2	Illustration of Two Board-to-Board Interconnect Geometries Including (a) Waveguide/Prism/Free-Space Propagation Scheme with Reflection Lensing Element and (b) Lensless Waveguide/Prism/Free-Space Propagation Scheme .....	5
2-3	Illustration of Fiber-to-Fiber Free-Space Interconnect with Reflection Lensing Element.....	6
2-4	Angular Tolerance, $\delta\theta = 10^{-4}$ for Lensing Element with $D = 5$ cm .....	7
2-5	An Example of an Optical Backplane Providing Waveguide/Fiber/Prism/Free-Space Interconnection Between Boards.....	8
2-6	(a) Approximate Single-Mode Fiber/Waveguide Coupling Loss (Excluding Fresnel Loss) as a Function of Laser Mode Spot Size, $W_f$ , Horizontal Waveguide Mode Spot Size, $W_x$ , and Vertical Waveguide Mode Spot Size, $W_y$ . (b) Blow up of the minimum loss which deviates around 1.....	10
2-7	A GaAs Single-Mode Ridge Channel Waveguide Cross Section with Vertical Thickness $T = 4 \mu\text{m}$ ; Including Cover with Refractive Index, $n_c$ (Air); Film with Refractive Index, $n_f$ , (Intrinsic (i) GaAs; Substrate with Refractive Index, $n_s$ (i AlGaAs) and Under Substrate (Semi-Insulating (SI) GaAs) .....	11
2-8	Non-Proper Adjustment of Phase-Space Areas for $T_z = \epsilon T_2$ , Assuming That $T_1 \Delta k_{x1} = T_2 \Delta k_{y2}$ . In this Case, the Coupling Efficiency is Reduced From 1 to $\epsilon$ .....	13
2-9	Interconnect Microprism Star Coupler (MSC) Providing Highly Parallel Fan-In and Fan-Out .....	14
2-10	Illustration of Fiber Cross Section at Fiber Array Front Plane .....	15
3-1	Schematic Diagram of the Optical Communication Channel Between Two Processing Nodes .....	18
3-2	Photograph Showing Collimation Accuracy of the Collimated Fiber Array. ....	18
3-3	Fan-out Operation (Top View of the Fiber-Grating Arrangement).....	19
3-4	Duplication (fan-out) of Optical Input Beam into Set of Five Outputs Each beam produced by the diffraction grating is redirected by a microprism array to provide normal incidence on a spatial light modulator (SLM) .....	19
3-5	The Interconnection Pattern is Established by the Spatial Light Modulator (SLM) Inserted into the Path of the Input Beams .....	20
4-1	Block Diagram of the Transmission System.....	21
4-2	Typical Small Signal Response of a Laser Diode .....	22
4-3	Schematic of the Direct Current Modulator Circuit .....	23
4-4	Laser and Light Current Characteristics with Bias ( $I_b$ ) and Drive Current ( $I_{\text{mod}}$ ) Superimposed .....	24
4-5	Investigated Circuit for the Single-Loop Feedback .....	25
4-6	Block Diagram of Optical Communications Using the Multiplexing of a 32 bit Bus.....	26
4-7	Block Diagram of the Hot Rod™ (a) Transmitter and (b) Receiver.....	26
4-8	Simulated Circuit of the Modulator With the Laser Diode Represented As a 10 Ohm Resistor.....	28

## LIST OF FIGURES(CONT)

4-9	Change in Modulation Current With Time For the Pure Resistor Model.....	28
4-10	Input and Output Voltage Levels (ECL) For the Pure Resistor Model.....	29
4-11	Simulated Circuit of the Modulator With the Laser Diode Represented as a Resistor-Inductor-Capacitor Combination.....	29
4-12	Change in Modulation Current With Time For the Model in Figure 4-12 .....	30
4-13	Input and Output Voltage Levels (ECL) For the Model in Figure 4-11 .....	30
4-14	Block Diagram of the Transmitter.....	31
4-15	Circuit Diagram of the Transmitter.....	32
4-16	Layout of the Printed Circuit Board .....	33
4-17	(a) Photograph of the Experimental Setup for Measuring the Data Rates; (b) Photograph of the Experimental Setup for Measuring the Optical Spectrum .....	34
4-17	(c) Closeup Photograph of the Portion of the Setup, Showing the Transmitter Module, Collimating and Focusing Lenses and the Optical to Electrical Converter.(d) Photograph Showing the Packaging of the Laser Diode and the Ferrule into which the Light from the Laser Diode is Coupled.....	35
4-18	Transmitter Output at Different Data Rates.....	39
4-19	Schematic Depicting the Presence of 2 Data Bits in One Time Period of a Square Wave.....	40
4-20	Optical Output Spectrum at Different Data Rates: (a) Continuous Wave; (b) 200 Mbits/sec .....	41
4-20	Optical Output Spectrum at Different Data Rates (c) 400 Mbits/sec, (d) 600 Mbits/sec .....	42
4-20	Optical Output Spectrum at Different Data Rates (e) 800 Mbits/sec, (f) 1 Gbit/sec .....	43
4-20	Optical Output Spectrum at Different Data Rates (g) 1.2 Gbits/sec and (h) 2 Gbits/sec. ....	44
5-1	Optical Equivalent of a Section of a Single Bi-Directional Electronic Backplane Bus Line.....	45
5-2	Schematic of the Optical Bi-Directional Backplane Bus in a Multi-Processor System.....	46
5-3	Diffraction Mechanism of Light in by Two Sets of Hologram Gratings Recorded on A Glass Substrate .....	48
5-4	Schematic of the 5-Channel Bi-Directional Backplane Optical Bus.....	49
5-5	Ratio Between the Maximum and Minimum Fanout Intensities as a Function of Coefficients A and B.....	53
5-6	Demonstration of the Functionality of Bi-Directional Optical Backplane Bus .....	55
5-7	Diffraction Mechanism of Light in by Two Sets of Hologram Gratings Recorded on a Glass Substrated .....	56
5-8	An Array of Pictures of the Fanout Configurations, Taken on the Signal-Incident Side of the Backplane, with the (a) 1st. (b) 2nd, (c) 3rd. and (d) rth Channel as the Input Coupler in the 1-to-7 bi-Directional Cascaded Fanout Optical Backplane Bus.....	56
5-9	Experimental Setup with the Bi-Directional Optical Backplane Bus Integrated with Transmitter and Receiver.....	57

## LIST OF FIGURES(CONT)

5-10	Receiver Output From the Setup in Figure 5-9 for a 1.2 Gbit/s Input Signal.....	57
5-11	Experimental and Theoretical Plots Showing the Relationship Between Angular Misalignment and Diffraction Efficiency.....	58
5-12	Schematic Showing the Related Parameters for Surface-Normal and Intra-Guiding-Plate Optical Interconnects.....	59
6-1	Schematic Diagram of the Demonstration Architecture .....	60
6-2	Schematic Diagram of the Microprism-Based Optical Crossbar Switch (Top View) .....	60
6-3	Optical Crossbar Router.....	61
6-4	Photograph of the 3x3 Optical Router.....	62
6-5	(a) Photograph of the Input Fibers Attached to the Diffraction Gratings; and (b) The Three Diffractor Gratings Formatted as the Input Fibers.....	64
6-6	The Crossbar Switching Diagram by the SLM.....	64
6-7	SLM Switching Configuration .....	65
6-8	Results of Fan-Out Broadcasting Interconnect .....	65
6-9	Photograph of the Focusing Lens with SLM and Output Fiber Attached with Coupling GRIN Lens .....	66
B-1	Geometry of the Problem .....	69

## LIST OF TABLES

4-1	8B/10B Encoding Example.....	27
4-2	List of all the Equipment Used in the Experimental Setup .....	36
5-1	Optimized Fan-out Distribution .....	53

## **1.0 INTRODUCTION AND EXECUTIVE SUMMARY**

In this program, Physical Optics Corporation (POC) proposed to develop an optical communication/switching system with data speeds well beyond any state-of-the-art electronic board-to-board computer interconnect. This interconnect is based on the use of microprism arrays to achieve large-scale, wideband interconnections for optoelectronic systems.

The main problem studied in this Phase II program was the current limitations of purely electronic interconnects, such as wide interconnection time bandwidths, large clock skew, and large RC time constants. These limitations cause serious bottlenecks in even the most advanced electronic board-to-board interconnects. This report presents the results of POC's investigation, and the implementation of the proposed microprism array-based optoelectronic system in this Phase II program.

In Phase II, the major accomplishments of the investigation and implementation were:

- Design of microprism arrays and electronic transceiver modules for the proposed optoelectronic interconnect system.
- Design of the optical interconnect system.
- Design, prototyping, and optimization of the transceiver modules.
- Design of the bi-directional optical backplane bus architecture.
- Optimization of the 5-channel optical backplane bus.
- Implementation and demonstration of a 3×3 microprism-based optoelectronic crossbar interconnect system.

## **2.0 MICROPRISM DESIGN AND ITS PHYSICAL CHARACTERISTICS**

The microprism free-space/fiber optic interconnect combined with channel waveguide interconnects is critical for this program. POC has designed the microprism and investigated its physical characteristics based on the general photonic product development philosophy, which always emphasizes the importance of critical optical and electrooptic components and subsystems.

In this section, we present the results of our theoretical analysis of fiber optic free-space communications using microprism interconnects, free-space propagation of fiber optic beams, free-space interconnects with diffraction elements, fiber-waveguide coupling and interconnects, and microprism interconnect packaging.

### **2.1 Free-Space Microprism Interconnects**

#### **2.1.1 Free-Space Propagation of Fiber Optic Beam**

Consider the free-space propagation of an optical beam emitted from a multi-mode fiber with a core diameter,  $d$ , a cladding diameter,  $D$ , and a numerical aperture, NA. The typical values for this type of fiber are:  $d = 62.5 \mu\text{m}$ ,  $D = 125 \mu\text{m}$ , and  $\text{NA} = 0.35$  (i.e., for 62.5/125  $\mu\text{m}$  fiber). For  $\lambda = 1 \mu\text{m}$ , the phase-space volume is

$$\Omega = \left( \frac{\pi d \text{NA}}{2\lambda} \right)^2 (2\pi)^2 = 1179(2\pi)^2 \quad (2-1)$$

Each mode occupies the elementary phase space volume of  $(2\pi)^2$ , and in this case the total number of modes is

$$M = \frac{\Omega}{(2\pi)^2} = 1179 \quad (2-2)$$

For monochromatic light, these modes create a speckle pattern with an average speckle size of

$$\delta = \frac{\lambda}{\theta} \quad (2-3)$$

where  $\theta$  is the angle of observation. For the distance from the fiber into the observation plane,  $z$ , the average speckle size is

$$\delta = \frac{\lambda z}{d} \quad (2-4)$$

Taking  $z = 10$  cm,  $d = 100$   $\mu\text{m}$ , and  $\lambda = 1$   $\mu\text{m}$ , we obtain  $\delta = 1$  mm (i.e., quite a large speckle size). In order to evaluate the diffraction region, we calculate the Fresnel number,  $F$ , in the form (see Appendix A)

$$F = \frac{k d^2}{8z} = \frac{\pi d^2}{4\lambda z} \quad (2-5)$$

where  $k = 2\pi/\lambda$ . For example, for  $d = 100$   $\mu\text{m}$ ,  $\lambda = 1$   $\mu\text{m}$ , and  $F = 10$  cm,  $F \approx 0.1$ ; i.e., for a 10 cm distance, we obtain the Fresnel diffraction region. We will use the geometrical optics approximation (which holds for  $F \gg 1$ ), a conservative assumption for the estimations made below. Here, we assume a simplified model that does not require any ray tracing. A more precise model is presented in Appendix B.

Considering the geometrical optics approximation, we assume that the fiber output is a uniform Lambertian source with limited angular sizes, as defined by the fiber's NA. In such a case, the total power of the fiber optic beam is

$$P = \int J d\Omega = \iint J_0 \cos \theta d\Omega \quad (2-6)$$

where  $J$  is the radiant intensity,  $\theta$  is the spherical angle (in Figure 2-1),  $d\Omega$  is the solid angle element, and the Lambertian Law is assumed to be

$$J = J_0 \cos \theta \quad (2-7)$$

where  $J_0$  is the radiant intensity (in W/star) at normal incidence ( $\theta = 0$ ), and the solid angle element is

$$d\Omega = \sin \theta d\theta d\phi \quad (2-8)$$

where  $\phi$  is the second spherical angle (Figure 2-1).

Substituting Eq. (2-8) into Eq. (2-6) and integrating angle  $\phi$  between 0 and  $2\pi$ , and angle  $\theta$  between 0 and  $\theta_0$ , where  $NA = \sin \theta_0$ , we obtain

$$p = J_0 \pi \sin^2 \theta_0 = J_0 \pi (NA)^2 \quad (2-9)$$

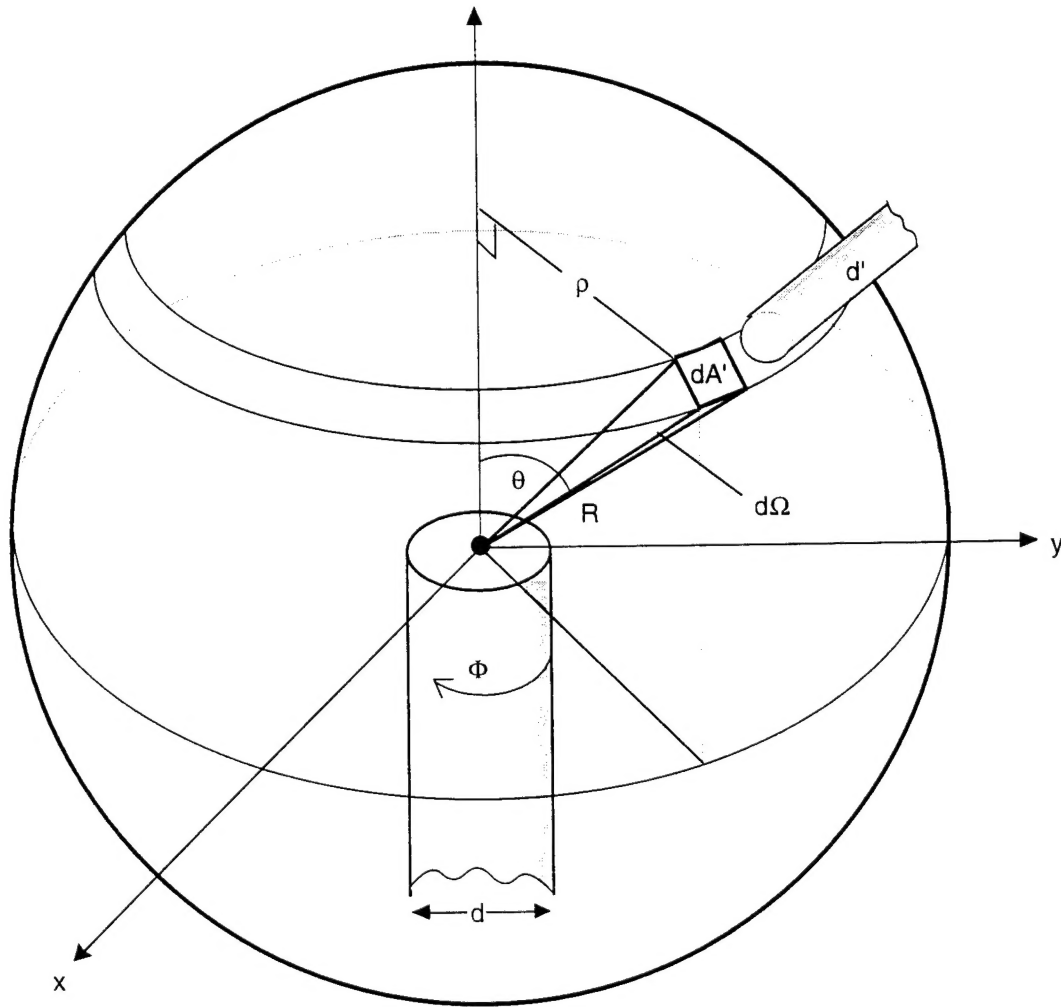


Figure 2-1  
Illustration of Fiber-to-Fiber Coupling Geometry.  $d$  is the diameter of the input fiber,  $d'$  is the diameter of the output fiber,  $(\theta, \rho)$  are the spherical angles,  $R$  is the fiber-to-fiber distance,  $d\Omega$  is the solid angle element, and  $\rho = R \sin \theta$ .

According to Figure 2-1, the area element is

$$dA' = \rho \, d\rho \, R \, d\theta = R^2 \sin \theta \, d\theta \, d\phi = R^2 \, d\Omega \quad (2-10)$$

and the power,  $\Delta p$ , received by the output fiber is

$$\Delta P = J_o \cos \theta \frac{\Delta A'}{R^2} \quad (2-11)$$

where

$$\Delta A' = \frac{\pi d'^2}{4} = \pi r'^2 \quad (2-12)$$

Therefore, the power fraction received by the output fiber is

$$\frac{\Delta P}{P} = \frac{J_o \cos \theta}{J_o \pi (NA)^2} \frac{\Delta A'}{R^2} = \frac{\cos \theta}{(NA)^2} \frac{r'^2}{R^2} \quad (2-13)$$

Assuming that both fibers are identical (i.e.,  $r' = d/2$ ), we finally obtain

$$\frac{\Delta P}{P} = \frac{\cos \theta}{(NA)^2} \frac{d^2}{4R^2} \quad (2-14)$$

For example, for normal incidence ( $\theta = 0$ ) (the best case),  $NA = 0.35$ ,  $d = 62.5 \mu\text{m}$ , and  $R = 10 \text{ cm}$ , we obtain

$$\frac{\Delta P}{P} < 10^{-7} \quad (2-15)$$

i.e., more than a 70 dB loss. Note that this result was obtained under the geometrical optics approximation, which gives better results (i.e., lower loss) than in reality, where the Fresnel diffraction approximation *should* be used. Considering our optical power budget, which usually accepts less than a 20 dB loss, this result is unacceptable. Therefore, we will discuss options other than of the full free-space interconnection (i.e., without lensing elements).

## 2.2 Free-Space Interconnects with Diffraction (Lensing) Elements

According to Section 2.1, Eq. (2-15), the optical power budget of the free-space interconnect is prohibitive, a > 70 dB propagation loss is obtained using a typical multi-mode fiber-to-fiber free-space interconnect. Therefore, other options must be considered. One alternative combines waveguide propagation, free-space propagation, prism-coupling, and a reflection lensing element (Figure 2-2(a)). The simple lensless waveguide/prism/free-space propagation scheme is also shown for comparison purposes (Figure 2-2(b)).

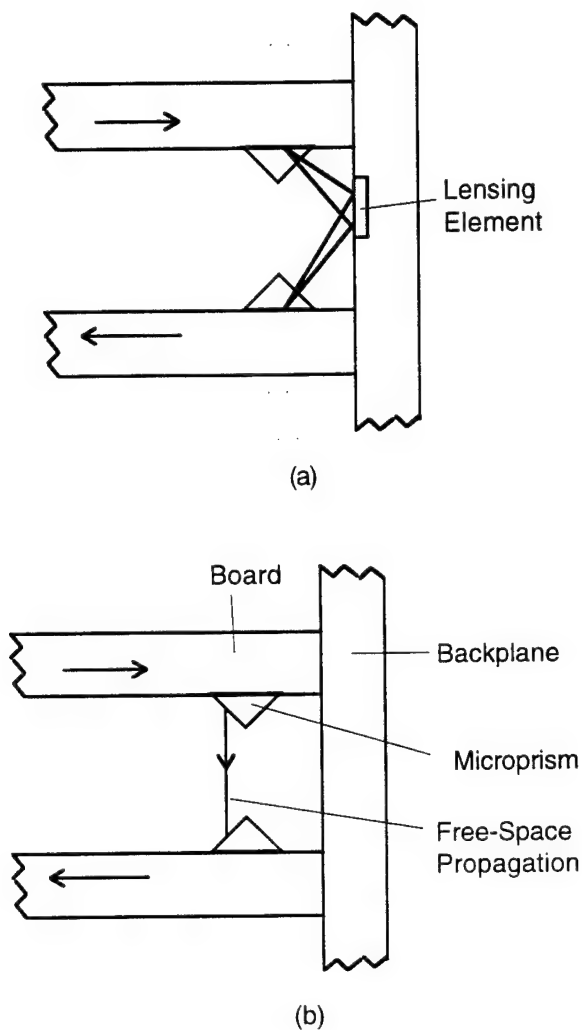


Figure 2-2  
Illustration of Two Board-to-Board Interconnect Geometries Including (a)  
Waveguide/Prism/Free-Space Propagation Scheme with Reflection Lensing Element  
and (b) Lensless Waveguide/Prism/Free-Space Propagation Scheme

For simplicity, we consider a fiber-to-fiber interconnect, as shown in Figure 2-3 (this analysis also applies to waveguide-to-waveguide interconnects).



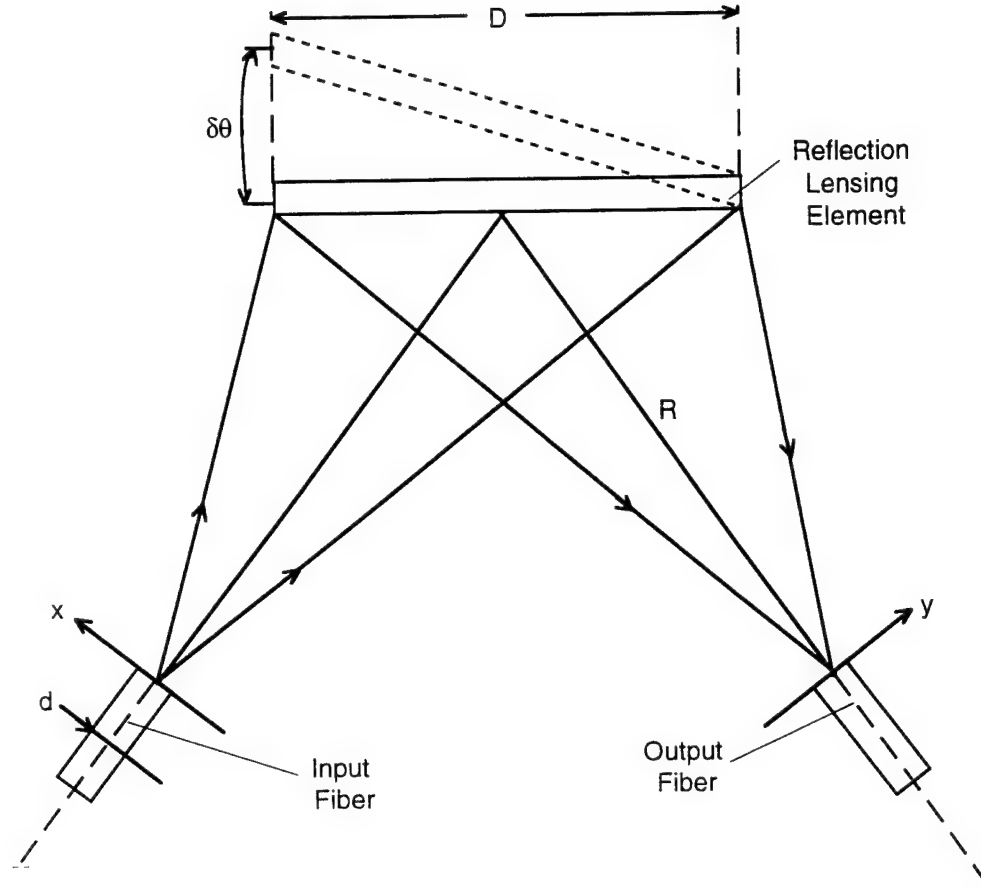


Figure 2-3  
Illustration of Fiber-to-Fiber Free-Space Interconnect with Reflection Lensing Element

Notice that the angular tilt of the reflection lensing element  $\delta\theta$  creates a rotation of the reflected beam in the output fiber front plane,  $y$ . This tilt must be smaller than

$$\delta\theta \leq \frac{0.1 d}{R} \quad (2-16)$$

in order to obtain a  $\delta y$  shift that is smaller than  $0.1 d$ .  $\delta y$  shifts of  $> 0.1 d$  can create significant coupling losses. Assuming  $d = 100 \mu\text{m}$  and  $R = 10 \text{ cm}$ , we obtain

$$\delta\theta \leq \frac{0.1 \times 100 \mu\text{m}}{10 \text{ cm}} = 10^{-4} \approx 0.005^\circ \quad (2-17)$$

Furthermore, the minimum size of the lensing element,  $D$ , should be about  $2R \times \text{NA}$  (i.e., for  $\text{NA} = 0.3$  and  $R = 10 \text{ cm}$ , we obtain  $D \sim 6 \text{ cm}$ ).

According to Eq. (2-17), the angular tolerance,  $\delta\theta$ , of the lensing element tilt is very demanding. To illustrate this, consider such a tilt at a  $5 \text{ cm}$  length (Figure 2-4).

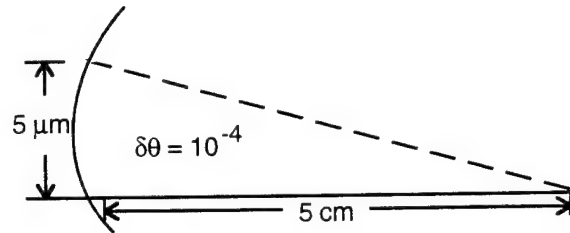


Figure 2-4  
Angular Tolerance,  $\delta\theta = 10^{-4}$  for Lensing Element with  $D = 5$  cm

Notice that in order to preserve the angular tolerance ( $\delta\theta$ ) of  $10^{-4}$  for a lensing element with  $D = 5$  cm, we need to keep the vertical dimensions within a  $5 \mu\text{m}$  tolerance. This requirement is unrealistic for macromechanical, multi-board geometries, leading us to the search for new types of packaging that can preserve these tolerances.

### 2.3 Fiber-Waveguide Interconnection

The fiber-waveguide interconnection is important in this program, primarily because we needed to provide a special (dedicated) package that can satisfy the challenging angular tilt tolerances. Furthermore, this package should preserve a satisfactory optical power budget, because the majority of digital data transmission systems cannot have a power budget that exceeds 20 dB total interconnection loss. The package should allocate space for the microprism and lensing elements in a micromechanically-controlled environment, which must be isolated from the regular macromechanical, board-to-board interconnection architecture.

In this program, we found that the most promising candidate for special packaging is based on the optical backplane. This combines fiber interconnects, free-space interconnects, transmission lensing elements, and multi-faceted microprisms within a micromechanically controlled dedicated packaging architecture. Outside of the optical backplane, the input/output fibers must be connected to board channel waveguides through either microprisms or directly with fibers; thus, the board channel waveguide interconnect architecture is isolated from the optical backplane architecture, and both architectures can be separately analyzed. In fact, the board channel waveguide interconnect architecture was investigated theoretically and experimentally under a subcontract awarded to Dr. Ray Chen at the University of Texas, Austin. The optical backplane architecture was investigated by POC in-house.

An example of an optical backplane architecture is illustrated in Figure 2-5. In this specific case, we use direct (transversal) fiber-waveguide coupling, which will be discussed in detail in the subsection below. The optical backplane design will be discussed in a separate technical chapter.

In Figure 2-5, the intra-board interconnects are made up of waveguide interconnects. They are connected to the fiber interconnects through either prism coupling or direct transversal coupling. In both cases, the fiber-waveguide coupling analysis presented in the next subsection holds true. The fiber interconnects are connected through the fiber array with free-space/microprism interconnects, combined with a transmission lensing element. This geometry enables the microprism interconnects to be isolated within the dedicated

packaging with micromechanical tolerances. These microprism interconnects provide highly parallel fan-in and fan-out in a sophisticated interconnect configuration.

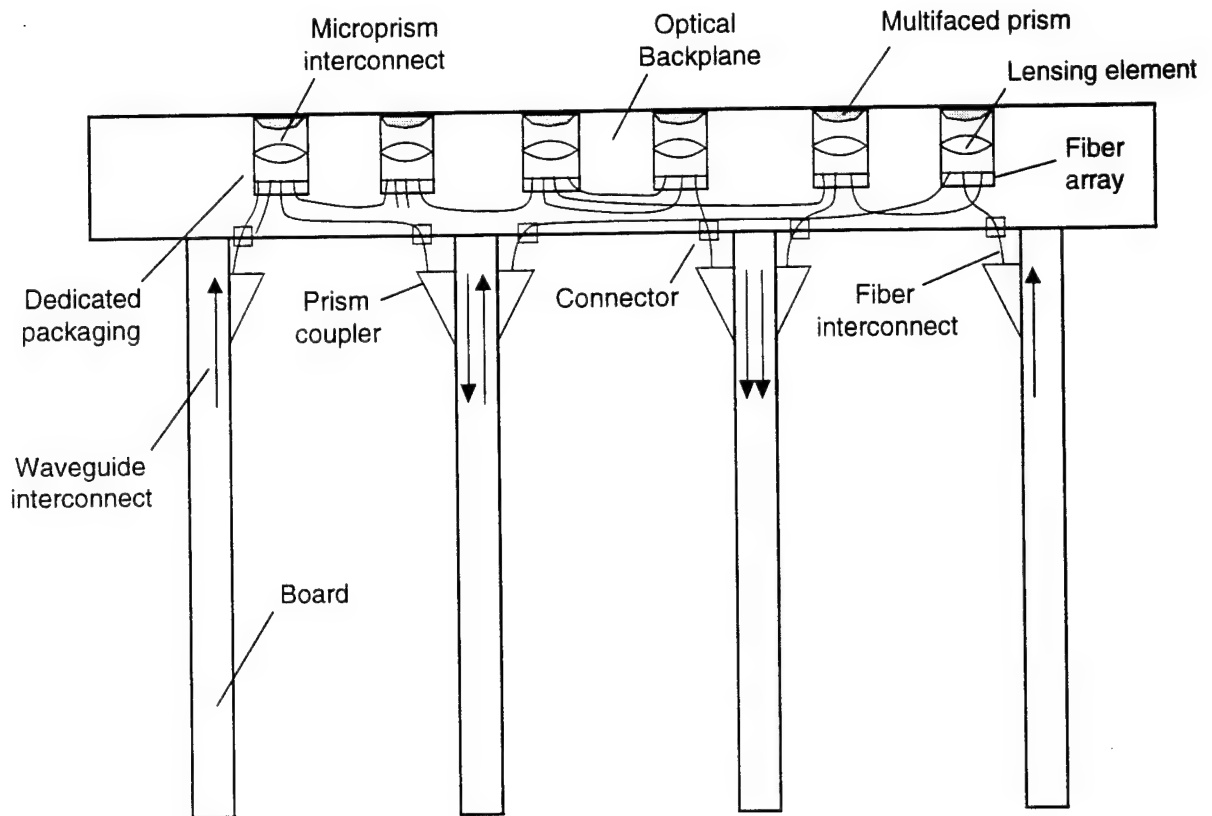


Figure 2-5  
An Example of an Optical Backplane Providing Waveguide/Fiber/Prism/Free-Space Interconnection Between Boards.

### 2.3.1 Fiber-Waveguide Coupling

Fiber-waveguide coupling for optical interconnects is important for two reasons. First, some integrated optical devices (such as modulators, switches, etc.) can be vital components in fiber optic communication systems. For example, high speed ( $> 10$  GHz) integrated optic modulators are usually required in order to transmit an optical beam through a fiber modulated by a microwave signal. Second, LD-waveguide coupling can also be realized indirectly; i.e., in two steps: LD-to-fiber and fiber-to-waveguide.

In the case of single-mode fiber-waveguide coupling, the phase-space volumes for a fiber beam and a waveguide beam occupy the same elementary cell  $\Omega_0 = (2\pi)^2$ , independent of their specific single-mode structure. In particular, the single-mode fiber beam in a near field approximation (i.e., just behind the fiber) occupies the phase-space volume,  $\Omega_f$ , in the form:

$$\Omega_f = \left[ \pi k_o^2 (NA)_f^2 \right] \left( \frac{\pi}{4} W_f^2 \right) \equiv (2\pi)^2 \quad (2-18)$$

where  $W_f$  is the beam's spot size (or diameter), which is approximately equal to the fiber core's diameter,  $d$ , (4 to 10  $\mu\text{m}$ ) and  $(NA)_f$  is the single-mode beam's numerical aperture. It should be emphasized that the  $(NA)_f$  parameter is not equal to the multimode fiber's numerical aperture, as defined by the fiber's refractive indices, because the single-mode beam is spatially coherent. Its space and frequency domain are not independent, but instead are related by the Heisenberg principle. On the other hand, a multimode beam is spatially incoherent, and its space and frequency domain remain independent (the fiber's diameter is independent of its numerical aperture).

Analogously, the phase-space volume of a single-mode waveguide beam  $\Omega_w$  also occupies the elementary cell,  $\Omega_o$ :

$$\Omega_w = \Omega_{wx} \times \Omega_{wy} \equiv (2\pi)^2 \quad (2-19)$$

where

$$\Omega_{wx} = \Delta k_x \cdot W_x \equiv 2\pi \quad (2-20a)$$

and

$$\Omega_{wy} = \Delta k_y \cdot W_y \equiv 2\pi \quad (2-20b)$$

where  $W_x$  and  $W_y$  are the spot sizes of the vertical beams, and are horizontal, and  $\Delta k_x$  and  $\Delta k_y$  are their (single-mode) numerical apertures, respectively.

It is sufficient in the single-mode coupling case to compare the beam sizes,  $W_f$ ,  $W_x$ , and  $W_y$ , since their angular sizes are automatically determined by the Heisenberg relations. This same elementary principle holds for a Gaussian beam, which approximates single-mode waveguide beams according to Eqs. (2-18) and (2-19),  $\Omega_w = \Omega_f = \Omega_o$ . Then, ignoring Fresnel reflection loss, almost 100% coupling efficiency can be achieved, according to the Liouville theorem. Therefore, when  $W_f \neq W_x \neq W_y$ , a suitable lens system can always be designed to obtain:

$$W_f = W_x = W_y \quad (2-21)$$

which guarantees almost 100% coupling efficiency. Here, "almost" means that the waveguide beam profile can be adjusted as quadratic but not circular. When Eq. (2-21) is satisfied, we do not need to worry about separate numerical aperture adjustments, since they are automatically computed using Eqs. (2-20a) and (2-20b). Because the fabrication of single-mode lensed fibers for improving coupling efficiency is difficult, especially for a highly anisotropic waveguide beam profile, we must accept some discrepancy between the fiber and the waveguide beam profiles. We do this by using a fiber-waveguide butt coupling procedure, which drops the coupling efficiency. Based on a Gaussian approximation of single-mode waveguide beams (shown in Figure 2-6), the coupling loss was plotted as a function of laser mode spot size,  $W_f$ , horizontal waveguide mode spot size,  $W_x$ , and vertical mode spot size,  $W_y$ . The amount of coupling loss depends only on the ratios  $W_x/W_f$  and  $W_y/W_f$  when the beams are centered. In this case, we have ignored the asymmetry of the waveguide beam profile, due to the possibly nonsymmetrical

waveguide geometry. This creates an 0.1 - 0.2 dB error. The coupling loss curves illustrated in Figure 2-6 are invariant with respect to permutation between  $W_x$  and  $W_y$ .

As an example, consider the cross section geometry of the GaAs single-mode ridge channel waveguide illustrated in Figure 2-7, with  $W_x = 10 \mu\text{m}$ ,  $W_y = 3 \mu\text{m}$ , and  $W_f = 8 \mu\text{m}$ . Thus,  $W_x/W_f = 1.25$  and  $W_y/W_f = 0.38$ . Using the permutation rule previously mentioned, we obtain a coupling loss of 1.7 dB (shown in Figure 2-6(a)). Without anti-reflection coatings, we need to add approximately 2 dB for Fresnel reflection loss.

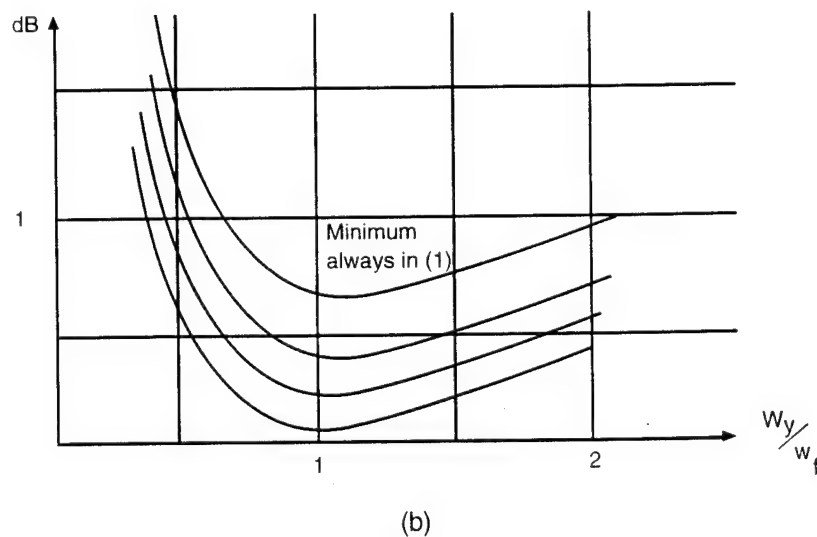
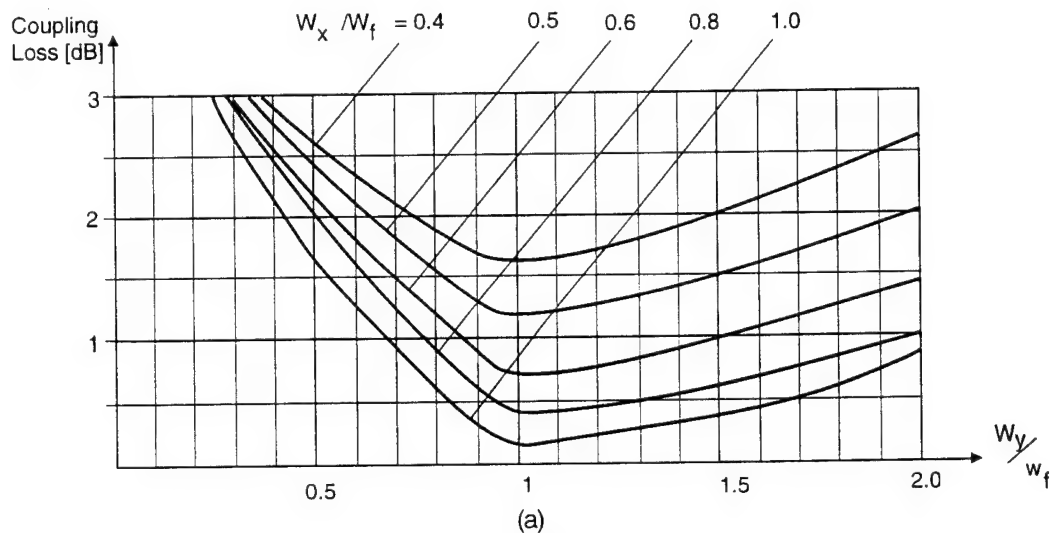


Figure 2-6  
(a) Approximate Single-Mode Fiber/Waveguide Coupling Loss (Excluding Fresnel Loss) as a Function of Laser Mode Spot Size,  $W_f$ , Horizontal Waveguide Mode Spot Size,  $W_x$ , and Vertical Waveguide Mode Spot Size,  $W_y$ . (b) Blow up of the minimum loss which deviates around 1.

The eigenvalues and eigenfunctions for both the fiber and the channel waveguides need to be numerically solved in order to maximize the overlap integral characterizing the mode field matching condition. This approach was used for titanium-diffused LiNbO<sub>3</sub> channel waveguides [1]. In this waveguide architecture, a single-mode fiber with a very small core diameter ( $d = 5 \mu\text{m}$  in Ref. [1]) was chosen. The modal field distributions of both the fiber and waveguide were compared in a free-space near-field zone in order to maximize the overlap integral and, in turn, the mode coupling efficiency. To make this maximization successful, the mode eigenequations for both the fiber and the waveguide were solved numerically to obtain a proper theoretical match. Then, the diffusion process for waveguide fabrication was tuned to fit with the theoretical predictions for a z-plate cut.

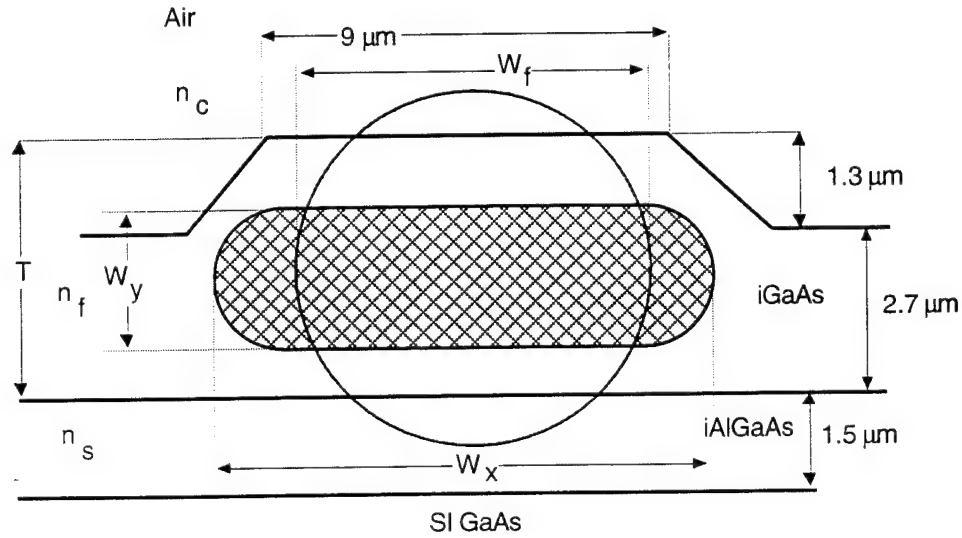


Figure 2-7

A GaAs Single-Mode Ridge Channel Waveguide Cross Section with Vertical Thickness  $T = 4 \mu\text{m}$ ; Including Cover with Refractive Index,  $n_c$  (Air); Film with Refractive Index,  $n_f$ , (Intrinsic (i) GaAs; Substrate with Refractive Index,  $n_s$  (i AlGaAs) and Under Substrate (Semi-Insulating (SI) GaAs). The channel waveguide single-mode spot area (hatched) computed on the basis of eigenfunction analysis has horizontal size,  $W_x = 10 \mu\text{m}$  and vertical size  $W_y = 3 \mu\text{m}$ . The single mode fiber beam spot near-field area with size  $W_f = 8 \mu\text{m}$  (representing step index single-mode 8/125  $\mu\text{m}$  fiber) is also included. This cross section is a fragment of channel waveguide linear array with 50  $\mu\text{m}$  pitch. (Made at POC).

The calculation of the coupling efficiency of multi-mode fiber-to-waveguide coupling is based on the Liouville theorem:

$$\eta_c = \frac{\Omega_{\text{output}}}{\Omega_{\text{input}}} = \frac{(2\pi)^2 M_{\text{output}}}{(2\pi)^2 M_{\text{input}}} = \frac{M_{\text{output}}}{M_{\text{input}}} \quad (2-22)$$

where  $\Omega_{\text{input}}$  is the phase-space volume of the input waveguide (fiber) and  $\Omega_{\text{output}}$  is the phase-space volume that can be accepted by the output waveguide. Since these volumes are proportional to the number of modes, we obtain the following fundamental theorem: *The coupling efficiency is equal to the ratio of the number of modes accepted by the output waveguide to the number of modes that propagate in the input waveguide.*

The phase-space volumes are separated into the products of space domains and frequency domains. For fiber we have

$$\Omega_f = \left( \frac{\pi d^2}{4} \right) \left[ \pi k_o^2 (NA)_R^2 \right] \quad (2-23)$$

where  $d$  and  $(NA)_R$  are the fiber's diameter and numerical aperture, respectively. For a channel waveguide, we have

$$\Omega_w = (W \cdot T) \left[ 4k_o^2 (NA)_x (NA)_y \right] \quad (2-24)$$

where  $W$  and  $T$  are horizontal and vertical waveguide sizes, and  $(NA)_x$  and  $(NA)_y$  are numerical apertures. According to the Liouville theorem, if  $\Omega_w \geq \Omega_f$ , then 100% coupling efficiency is achievable. But, if  $\Omega_w < \Omega_f$ , then the coupling efficiency's theoretical limit is

$$(\eta_c)_{\max} = \frac{\Omega_w}{\Omega_f}; \text{ and } \eta_c \leq \eta_{\max} \quad (2-25)$$

where the  $\Omega_f$  and  $\Omega_w$  parameters are defined by Eqs. (2-23) and (2-24). In order to maximize the coupling efficiency, we must design the lens system so that  $\Omega_{\text{output}} = \Omega_w$ . To illustrate, when

$$W(NA)_x = T(NA)_y = d(NA)_R \quad (2-26)$$

but  $W \neq T \neq d$ . According to Eqs. (2-23) and (2-24),  $\Omega_w > \Omega_f$ , and 100% coupling efficiency is achievable. In order to do this, we need to design the lens system so that it transforms the circular fiber beam spot with diameter  $d$  into an elliptical spot with axes  $a$  and  $b$  and with dimensions:  $a = W$ ,  $b = T$ . According to Eq. (2-26) then,  $(NA)_a = (NA)_x$  and  $(NA)_b = (NA)_y$ ; thus,

$$a(NA)_a = b(NA)_b = d(NA)_R \quad (2-27)$$

and 100% coupling efficiency is achieved.

In general, the lens system should provide the transformation that makes the input and output space and frequency domain as similar as possible. With butt coupling, we must compute the overlap areas in the space/frequency domain. In order to do this, we need to be able to evaluate the fiber beam spots projected at the front plane of the waveguide. In this case, the near field approximation works only if the Fresnel number,  $F$ , satisfies the condition:

$$F \gg 1, \quad \text{where } F = \frac{k_o d^2}{2z} \quad (2-28)$$

where  $z$  is the distance between the fiber and waveguide. For example, for  $d = 50 \mu\text{m}$ ,  $z = 100 \mu\text{m}$ , and  $\lambda = 1.3 \mu\text{m}$ , we obtain  $F = 60$ ; i.e., the condition in Eq. (2-28) is satisfied.

The coupling system transfers the light from the LDs into a single-mode 8/125  $\mu\text{m}$  fiber array, and from there into a single-mode channel waveguide array. The beams are again transferred to a 8/125  $\mu\text{m}$  fiber array, and finally into a photodetector (PD) array. A moderate 3 dB coupling loss between the single-mode fiber and waveguide can be achieved (see Figure 2-6).

When using multi-mode waveguide-to-waveguide transversal coupling, we maximize the coupling efficiency in the same way as in Section 2.3.1. An improper adjustment of the phase-space volume is shown in Figure 2-8 for the 1-D case. Even if both the output and input phase-space domains have the same phase-space volume, the coupling efficiency,  $\eta$ , is far less than 100%. Using Eq. (2-22), we obtain

$$\eta_1 = \frac{\text{overlap area}}{\text{input area}} = \varepsilon \quad (2-29)$$

where  $T_z = \varepsilon T_1$ .

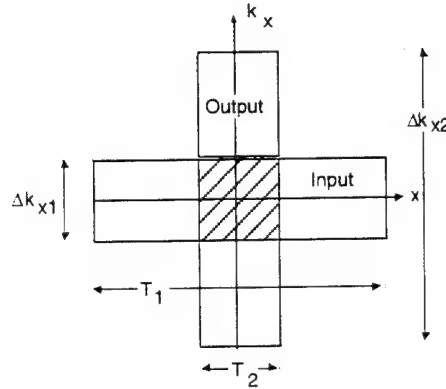


Figure 2-8

Non-Proper Adjustment of Phase-Space Areas for  $T_z = \varepsilon T_2$ , Assuming That  $T_1 \Delta k_{x1} = T_2 \Delta k_{x2}$ . In this case, the coupling efficiency is reduced from 1 to  $\varepsilon$ .

## 2.4 Microprism Interconnect with Dedicated Packaging Providing Micromechanical Tolerances

In this section, we investigate a microprism interconnect with dedicated packaging providing micromechanical tolerances, previously illustrated in Figure 2-5. This Microprism Star Coupler (MSC) can provide highly parallel fan-in and fan-out, combining free-space propagation from the fiber array through a transmission lensing element with that from a multi-faceted microprism reflection element.

According to Figure 2-9, the NA of multimode fiber is

$$\text{NA} = \sin \alpha_M \quad (2-30)$$

and the distance of parallel rays from the inter-facet boundary areas are in the paraxial approximation:



$$\rho_1 = f \sin \alpha_1 \quad (2-31a)$$

$$\rho_M = f \sin \alpha_M \quad (2-31b)$$

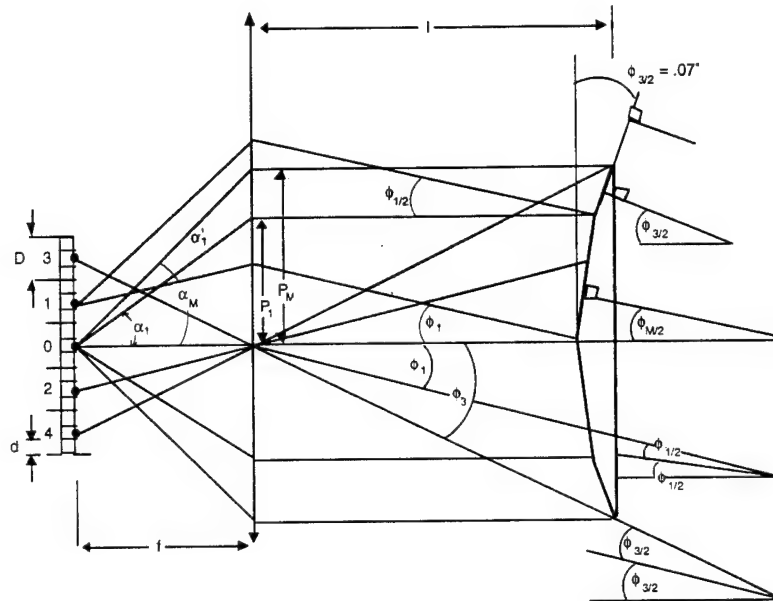


Figure 2-9

Interconnect Microprism Star Coupler (MSC) Providing Highly Parallel Fan-In and Fan-Out. It combines free-space propagation from fiber array (with core diameter,  $d$ , and cladding diameter,  $D$ ) through transmission lensing element with focal length,  $f$ , and four-facet microprism reflection element with facet angles,  $\phi_{1/2}$ ,  $\phi_{2/2}$ ,  $\phi_{3/2}$ , and  $\phi_{4/2}$ , ( $\phi_1 = \phi_2$  and  $\phi_3 = \phi_4$ ), at the distance,  $\ell$ , from the lens.

In the fan-out mode, the input beam from the central (0) fiber propagates at a  $\alpha_M$  maximum angle through the lens into the four-facet microprism reflection element. All of the fibers are identical and have core diameters,  $d$ , and cladding diameters,  $D$ . They are closely located within the fiber array, which is located at the focal plane of the lens. Therefore, the lens with focal length,  $f$ , transforms the spherical input beam into a collimated beam. This beam is geometrically reflected by four cylindrical plane microprism facets, under angles  $\phi_1$ ,  $\phi_2$ ,  $\phi_3$ , and  $\phi_4$ , ( $\phi_1 = \phi_2$ ,  $\phi_3 = \phi_4$ ). Therefore, the focal angles must be

$$\frac{\phi_1}{2}, \frac{\phi_2}{2}, \frac{\phi_3}{2}, \frac{\phi_4}{2} \quad (\phi_1 = \phi_2, \phi_3 = \phi_4) \quad (2-32)$$

These beams will be accepted by output fibers (1,2,3,4) only if their divergence ( $\alpha_1'$ , etc.) is less than  $\alpha_M$ . The geometrical construction needed to construct the angles determined by Eq. (2-32) is illustrated in Figure 2-9. According to this construction, the microprism's multi-faceted angles are ( $\phi_{1/2}$ ,  $\phi_{2/2}$ ,  $\phi_{3/2}$ , and  $\phi_{4/2}$ ), where

$$\phi_1 = \arctan\left(\frac{D}{f}\right) \quad (2-33a)$$

$$\phi_2 = \phi_1 \quad (2-33b)$$

$$\phi_3 = \arctan\left(\frac{2D}{f}\right) \quad (2-33c)$$

$$\phi_4 = \phi_3 \quad (2-33d)$$

For example, for POC's packaging with  $d = 62.5 \mu\text{m}$ ,  $D = 125 \mu\text{m}$ , and  $f = 6.8 \text{ mm}$ , we obtain  $\phi_1 = 1.05^\circ$  and  $\phi_2 = 2.1^\circ$ ; thus,

$$\frac{\phi_1}{2} = \frac{\phi_2}{2} = 0.52^\circ \quad (2-34a)$$

and

$$\frac{\phi_3}{2} = \frac{\phi_4}{2} = 1.05^\circ \quad (2-34b)$$

In order to calculate the angular tolerances of the facets, consider the fiber cross sections illustrated in Figure 2-10.

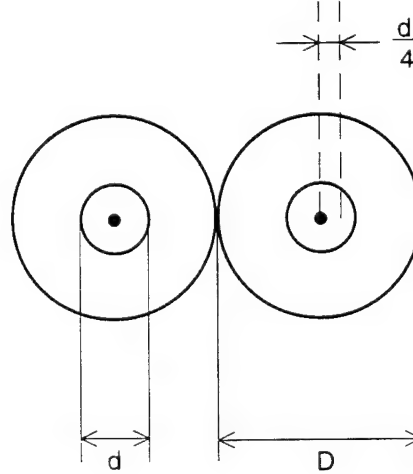


Figure 2-10  
Illustration of Fiber Cross Section at Fiber Array Front Plane

In order to preserve a reasonable power budget (i.e., a coupling loss less than 2 dB), we assume that the beam center cannot shift more than  $d/4$  (Figure 2-10). Therefore, the angular facet tolerance,  $\delta\theta$ , can be calculated from the following relation:

$$\delta\theta = \frac{d}{4D} \times \Delta\theta \quad (2-35)$$

where  $\Delta\theta$  is angular separation between facet angles (in our example,  $0.52^\circ$ ).

For our design ( $d = 62.5 \mu\text{m}$ ,  $D = 125 \mu\text{m}$ ,  $\Delta\theta = 0.52^\circ$ ), we obtain

$$\delta\theta = 0.06^\circ \quad (2-36)$$

thus, Eq. (2-34) must be modified into the following relations

$$\begin{aligned}\frac{\phi_1}{2} = \frac{\phi_2}{2} &= 0.52^\circ \pm 0.06^\circ \\ \frac{\phi_3}{2} = \frac{\phi_4}{2} &= 1.05^\circ \pm 0.06^\circ\end{aligned}\tag{2-37}$$

i.e., about 10% accuracy.

When the fibers are not closely located in the general case, the relation in Eq. (2-35) must be replaced by the formula

$$\delta\theta = \frac{d}{4b} \times \Delta\theta\tag{2-38}$$

where  $b$  is the distance between fibers. However, Eq. (2-33) must also be replaced by the formula with the  $b$  parameter instead of the  $D$  parameter. For example, assume that we located additional "dark" (unused) fibers between the active fibers. In such a case,  $b = 2D$ , and, instead of Eq. (2-34), we obtain  $\phi_{1/2} = 1.05^\circ$  and  $\phi_{3/2} = 2.1^\circ$ ; thus,  $\Delta\theta = 2.1^\circ$  and Eq. (2-38) provides again the same result:  $\delta\theta = 0.06^\circ$ . Therefore, the more extended geometries do not help, and the angular tolerance remains  $0.06^\circ$ . Nevertheless, the relative tolerance reduces from approximately 10% to 5%.

Our final concern is that we cannot assume that off-the-shelf lenses will always have the same focal length,  $f$ . Therefore, we need to consider here the significant differences between the *R&D* case (which we can design to a specific focal length), and the *commercial* case, where we need to assume some focal length tolerances.

During our inquiries, we found that plastic lens tolerances  $\delta f/f$  are  $> 10\%$ , ruling out the plastic lens technology for this case. However, glass lenses give us

$$\frac{\delta f}{f} = 3\%\tag{2-39}$$

Therefore, for the mass production case, we need to modify Eq. (2-38) into the formula

$$\frac{\delta x}{x} = \frac{\delta f}{f} + \frac{\delta\phi}{\phi}\tag{2-40}$$

where  $\delta x/x$  is the minimum shift tolerance of the beam spot at the fiber array front plane. We apply here the approximate relation, valid at the paraxial approximation

$$x \equiv f \sin \phi \equiv f\phi\tag{2-41}$$

In our case, we have

$$\frac{\delta x}{x} = \frac{\frac{d}{4}}{D} = \frac{d}{4D} = \frac{62.5 \mu\text{m}}{4 \times 125 \mu\text{m}} = \frac{1}{8} \quad (2-42)$$

and for  $\delta f/f = 0.03$ , we obtain  $\delta\phi/\phi = 0.095$ ; i.e., about 10% accuracy.

In general, a tilt accuracy of  $< 0.1^\circ$  is difficult to achieve using the standard optical lens/prism technology currently available. Therefore, technologies such as plastic/molding, glass, metal, etc. should be considered. This is important, because the successful fabrication of the MSCs could significantly improve the technology of advanced board-to-board interconnects.

### 3.0 DESIGN OF THE OPTICAL INTERCONNECTION SYSTEM

After the successful theoretical analysis of the feasibility of fiber optic free-space communications using microprism arrays, POC began formulating the optical interconnection architecture and system design. This included the design of the final demonstration units – both optical and electronic systems. The detailed results of a multi-microprocessor system using optical interconnects, including system architecture, communication scheme, and a specific fiber optic free-space interconnect, named a free-space diffractive signal router, are presented in this section.

#### 3.1 Fiber Optic Free-Space Communication

POC's proposed system combines fiber optics and free-space optical communications. Initially, the encoded data from each data channel is sent to a transmitter, where it is converted to an optical signal and sent over an optical fiber to an optical switch, which uses free-space multiplexing to redirect the signal to another microprocessor. The redirected light is launched into a receiving fiber of the receiving data channel, where it is reconverted to an electrical signal by a photodetector. The transmitter system modulates the intensity of the laser diode (SHARP, 780 nm). Light from the LD is coupled into the optical fiber using a 0.25 pitch graded-index (GRIN) rod. The fiber used in the demonstration unit is a graded index fiber with a 62.5  $\mu\text{m}$  core diameter. To show the feasibility of the proposed concept, the light from the other end of the fiber was collimated by a 3 mm diameter GRIN rod. Figure 3-1 shows a schematic diagram of one optical communication channel. Similar procedures were followed to implement the fiber optic transmitter for other microprocessors. In the actual system demonstration, POC used a 3x3 crossbar switch to demonstrate a video transmission application. The collimation accuracy was in the range of  $2.6^\circ$  (divergence of the collimated beam).

In order to assure proper collimation before the integration of the entire system, we tested the divergence of the collimated beams. Figure 3-2 shows four collimated beams on a test screen. The distance between the GRIN rod array and the screen was approximately 2 inches. The spot size was approximately 2.2 mm. The photograph was obtained from a TV screen connected to a CCD camera without an IR filter.

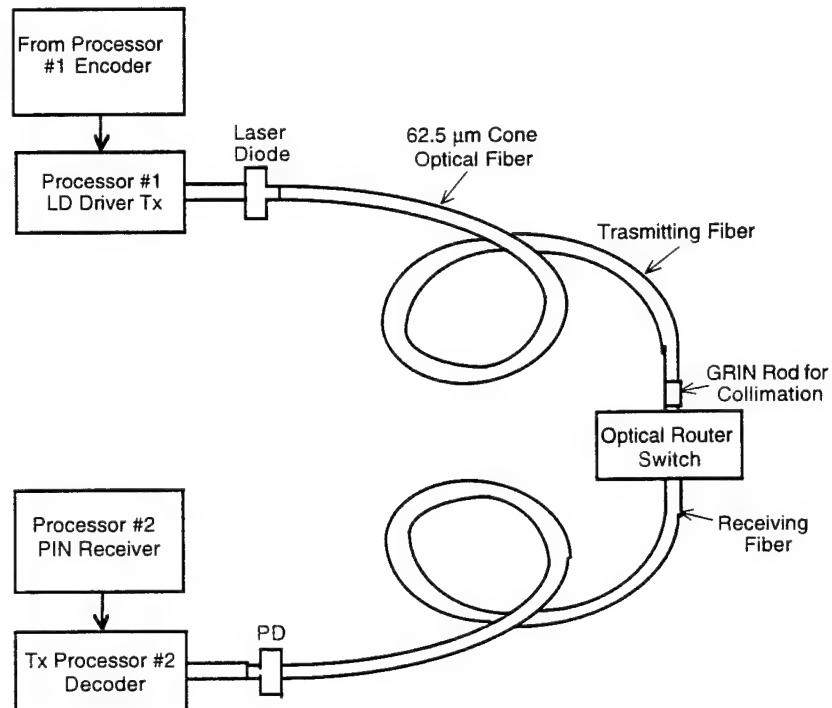


Figure 3-1  
Schematic Diagram of the Optical Communication Channel Between Two Processing Nodes

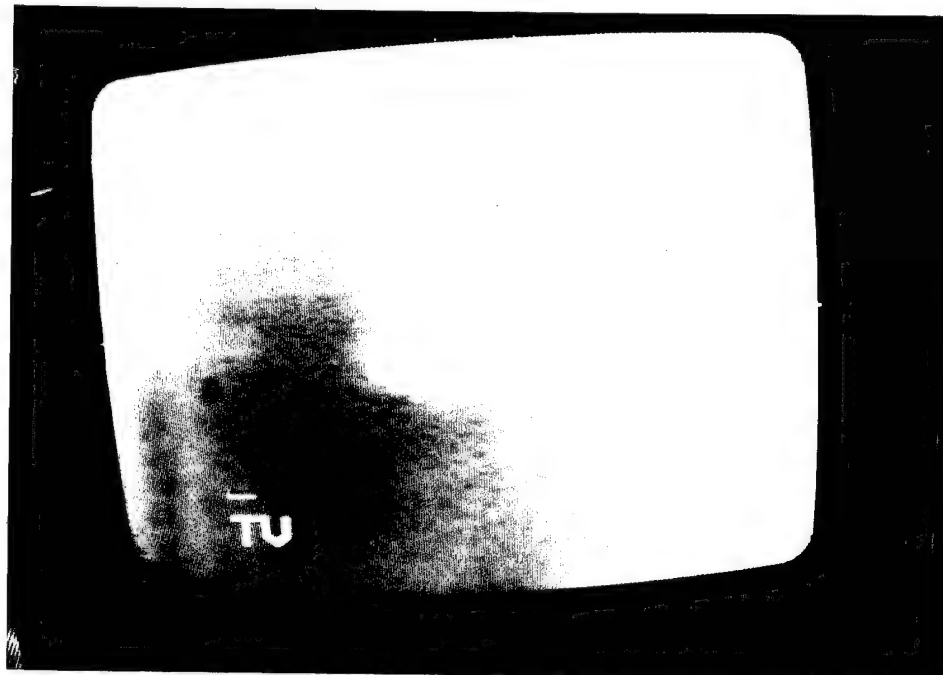


Figure 3-2  
Photograph Showing Collimation Accuracy of the Collimated Fiber Array.

### 3.2 Free-Space Diffractive Signal Router

Signal routing is provided using diffractive optical elements (DOEs), such as a one-dimensional grating, which provides the necessary fan-out operation for the input array of the optical fiber illuminator. Each input beam is broadcast into four spatial locations. The top view of the grating's fan-out operation is shown in Figure 3-3. Each of the four beams is angularly multiplexed, and represents a data transfer to a different receiving data channel. The fan-out operation is shown in Figure 3-4.

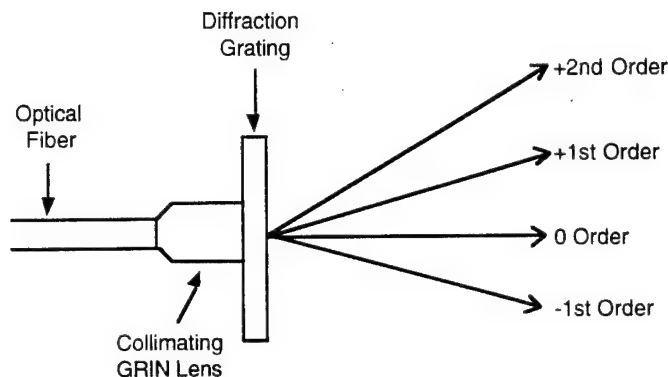


Figure 3-3  
Fan-out Operation (Top View of the Fiber-Grating Arrangement)

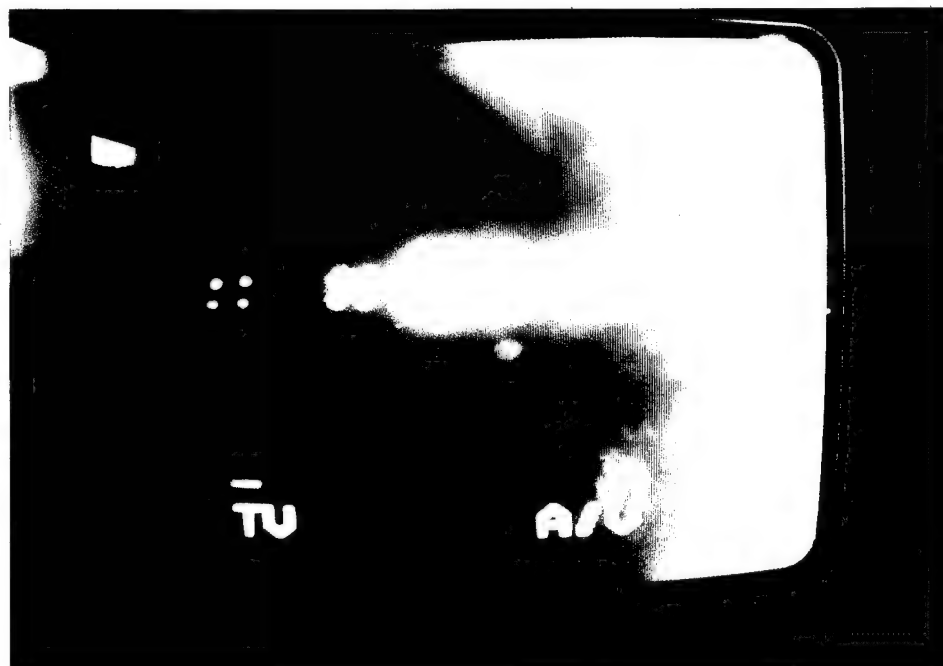


Figure 3-4  
Duplication (fan-out) of Optical Input Beam into Set of Five Outputs

Each beam produced by the diffraction grating is redirected by a microprism array to provide normal incidence on a spatial light modulator (SLM). Four different prisms are used, each for a single fan-out operation. The interconnection pattern is established by the spatial light modulator (SLM) inserted in the path of the input beams (Figure 3-5). The experimental results are provided in Section 6.0.

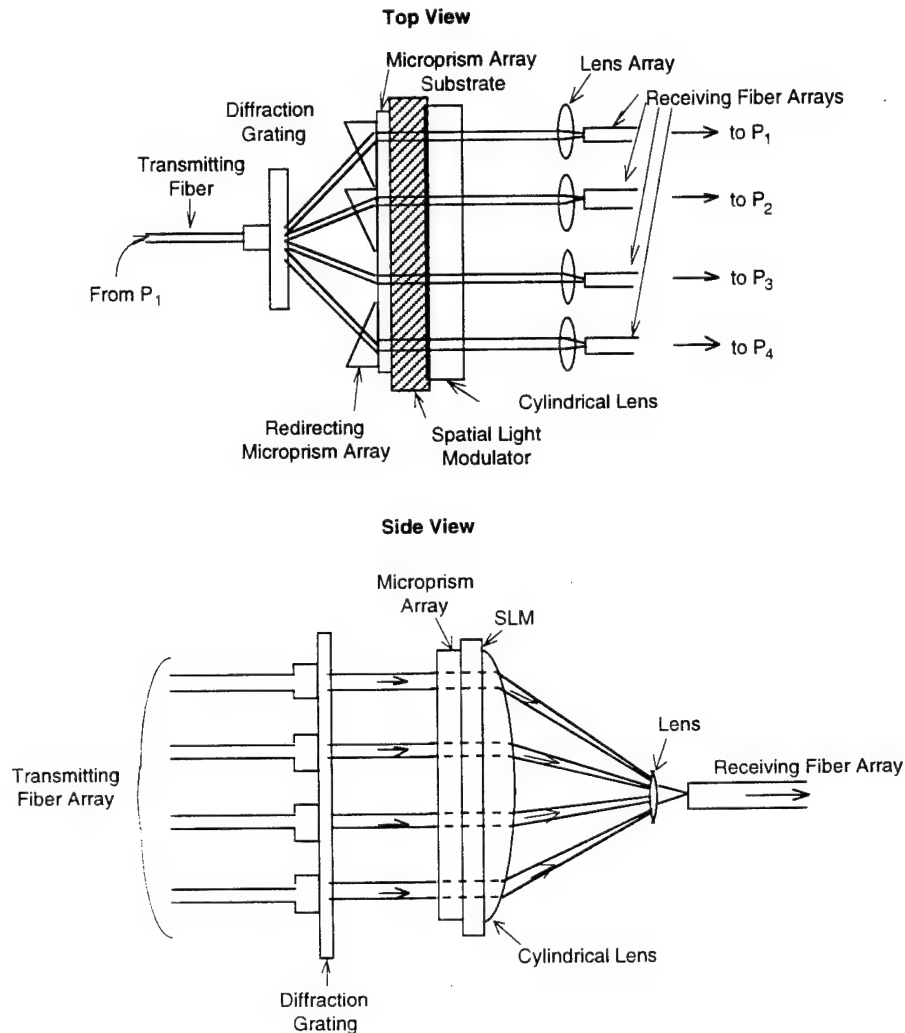


Figure 3-5  
The Interconnection Pattern is Established by the Spatial Light Modulator (SLM) Inserted into the Path of the Input Beams

#### 4.0 DESIGN, PROTOTYPING AND OPTIMIZATION OF ELECTRONIC SYSTEM

Following the design of the optical interconnect system, we next designed, prototyped, and optimized the electronic systems. This effort included the design of the high speed laser diode drivers, transmitters and receivers, and parallel-to-serial/serial-to-parallel converters. This section details this effort.

#### 4.1 Electronic System

Serial communications utilizing time division multiplexing (TDM) require high speed digital links operating in the range of 1 Gb/s. This report discusses our design of a 1 Gb/s optical transmitter. This includes the design of the transmitter, receiver, and the optical bus, which provide the interconnection between the transmitter and receiver modules. The transmitter is compatible with ECL logic. The optical bus is an efficient combination of integrated optics, holographic or prism interconnects, and optoelectronic processing. This optical bus removes the bottlenecks encountered in electrical data buses as a result of wide interconnection time bandwidths, large clock skew, and large RC time constants. Low material dispersion and low propagation losses result in high data acquisition and processing rates.

Figure 4-1 shows the basic block diagram for the transmission system. As in any transmitter, the modulation of the information source is a very important criterion. In our case, the source is a laser diode operating at a wavelength of 1300 nm.

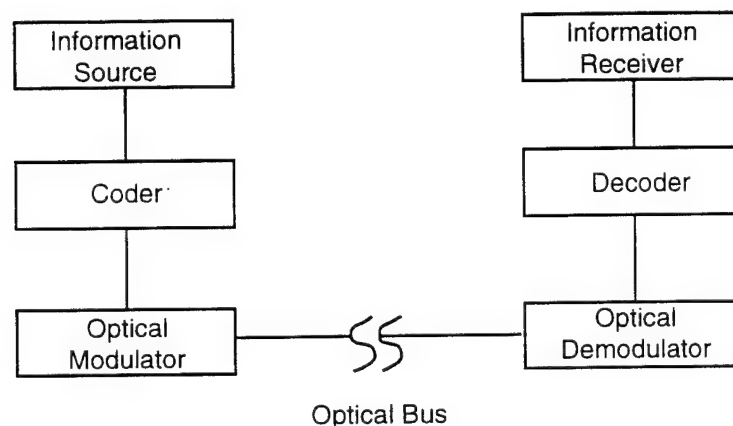


Figure 4-1  
Block diagram of the transmission system

The typical spectral width of the laser diode that we used is about 2 nanometers. The ultimate modulation rate of any lightwave system is limited by the modulation bandwidths of the source, the interconnect medium, and the detectors [2].

The power from the laser diode that can be coupled into the optical bus is much greater than the power from a light emitting diode (LED). This increased power output from the transmitter (when compared to a conventional LED) reduces the constraints on the receiver design, and detection is much easier because of it. The high speed optical transmitter can find use in many digital applications, including video systems, where high data rates are needed, or PFM transmission of TV signals. In addition, it can be used in digitized video data streams and in digitized high definition TV applications. The transmitter can also be used in high-speed computer interconnects [3].



#### 4.1.1 Source Modulation

The performance of any light wave transmission system depends heavily on the efficiency of the source modulation. When the laser diode is operating above its threshold current, it exhibits a small signal response (as shown in Figure 4-2). The relaxation effects are suppressed to the gigahertz region, as the signal response indicates, because of the very short carrier lifetime and photon lifetime [2]. The carrier lifetime  $t_c$  is around  $10^{-11}$  seconds, and the photon lifetime  $t_p$  is around  $10^{-11}$  seconds in the presence of simulated radiation. Relaxation effects are observed beyond the resonance frequency, and are given by the following relation:

$$\omega_r = [(1/t_c t_p) \{ (I_m/I_{th}) - 1 \}]^{1/2} \quad (4-1)$$

where  $I_m$  is the dc current applied to bias the laser above its threshold current,  $I_{th}$ .

The frequency response and the shape of the resonance curve can vary, depending on the laser structure and the amount of spontaneous light coupled into the lasing modes. The modulation of the laser diode is limited by the turn-on delay, which in turn can be minimized by biasing the laser diode at, or slightly above, its threshold [4]. Relaxation oscillations become a limiting factor for the modulation rate of the laser transmitters as the data rate approaches the relaxation frequency  $\omega_r$ .

The RC time constant of the electrical circuit must be minimized in order to increase the modulation rate of the transmitter. Reducing the RC time constant increases the speed of the electrical circuit, thus improving the modulation characteristics of the transmitter.

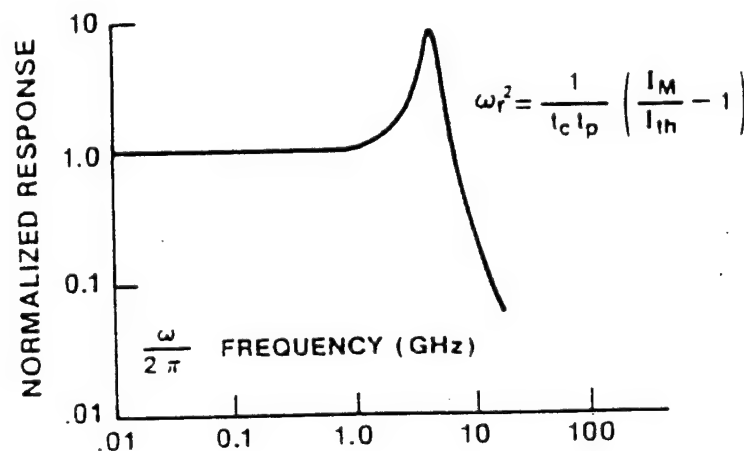


Figure 4-2  
Typical Small Signal Response of a Laser Diode

#### 4.2 Modulator Circuit Design Considerations

The modulator used in Phase II was an emitter-coupled current routing switch; a modification of the common emitter driver. It is operated in the switching mode. In spite

of being overdriven at the input, it is not saturated, resulting in fast switching speeds [2]. The operating principle of this direct current modulator follows.

$Q_3$  is a constant current source, and as a result, no transients severe enough to affect performance during switching are obtained.  $R_3$  can be adjusted to control the modulation current. Current magnitude from  $Q_3$  is limited by the voltage drop across the laser diode. The laser diode can be easily directly biased by adding the bias at the n contact of the laser diode (node B in Figure 4-3).  $Q_2$  and  $Q_3$  form a nonsaturating current switch, implying that  $Q_2$  is always in its active region, and its switching action is not affected by the added dc current source. This differential switch can be used with an input logic gate, which is useful as a line receiver for the coded data stream and to compensate for any initial timing delay in the transmitter circuits.

The circuit in Figure 4-3 has an ECL gate and level shifting resistors  $R_1$  and  $R_2$ . This satisfies the requirements for a "high" to "low" swing of -0.8V to -1.8V for ECL logic (an approximately 2V drop across the laser diode) and the grounding of its p contact.

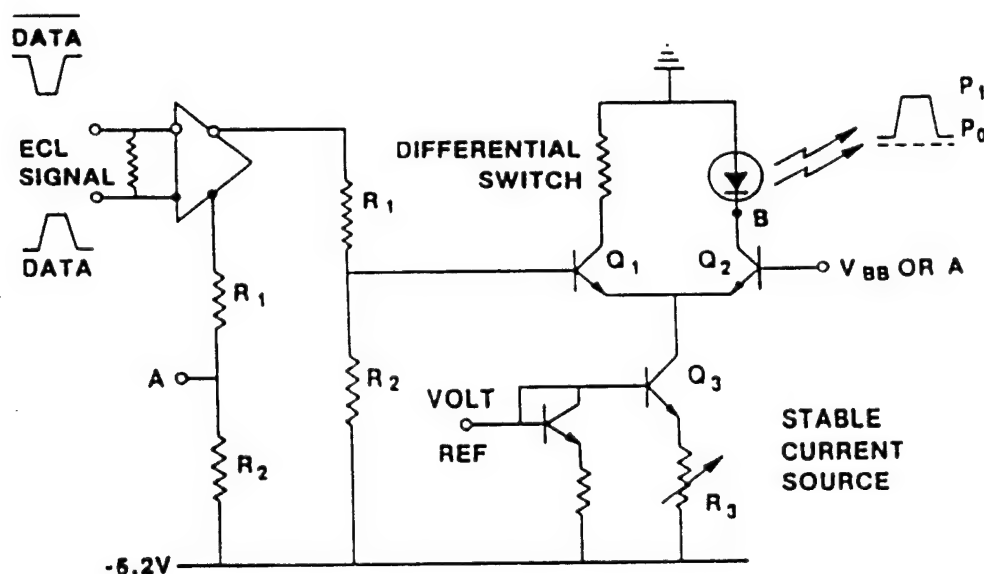


Figure 4-3  
Schematic of the Direct Current Modulator Circuit

$Q_2$  has the laser diode in its collector circuit, and can be switched against a fixed voltage,  $V_{BB}$ , set between the "high" and "low" logic levels. Alternatively, it may be switched with a signal complementary to that imposed at the base of  $Q_1$  ("node A" for example). This results in faster switching.

### 4.3 Biasing Considerations

The biasing circuit of the modulator is actually added to the basic modulator circuit in order to complete the transmitter design. The biasing circuit employs a dc bias current,  $I_B$ , with a chosen value close to that of  $I_{th}$  (Figure 4-4). The bias  $I_b$  and drive current  $I_{mod}$  are

superimposed in the input current to produce the output light. The dc bias is always under feedback control in order to keep  $I_B/I_{th}$  close to unity with changes in  $I_{th}$  or  $\eta$  (the differential quantum efficiency). The modulator and the biasing circuit together form the transmitter.

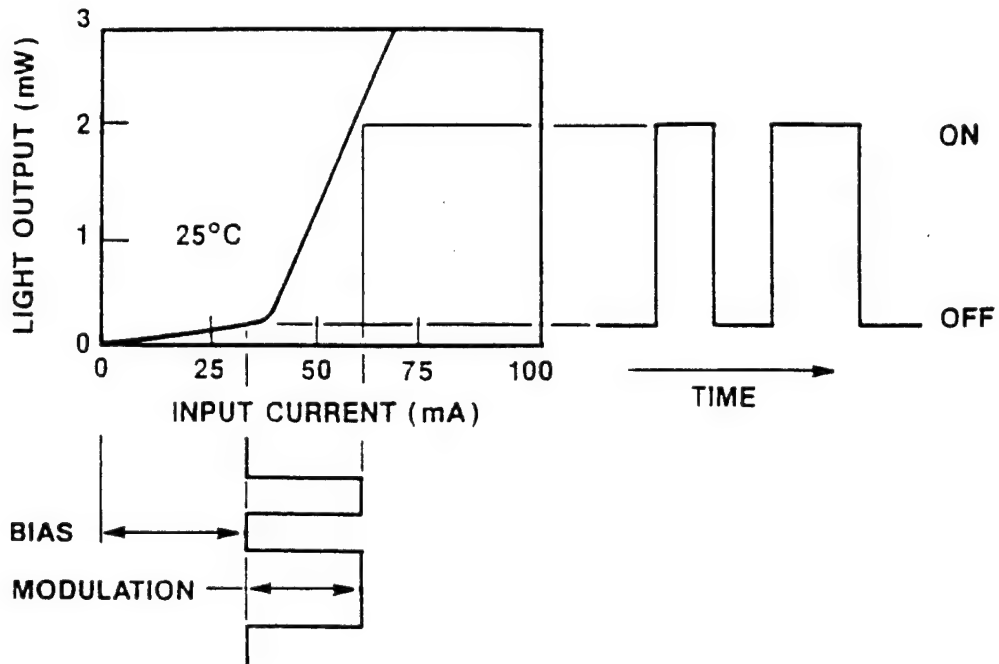


Figure 4-4  
Laser and Light Current Characteristics with Bias ( $I_b$ ) and Drive Current ( $I_{mod}$ )  
Superimposed

A single loop feedback transmitter design for average optical power control was considered in this program (Figure 4-5). The biasing keeps the bias point  $I_B/I_{th}$  between 0.8 and 1. The operational amplifier  $A_1$  in Figure 4-5 compares the average current of the monitoring photodiode (dc component) with a preset reference current  $I_{REF}$ . When the optical output changes,  $A_1$  changes the dc biasing current,  $I_B$ , from the current source  $Q_4$ , until the output power level is re-established. Two methods being explored for deriving a value for  $I_{REF}$  include a second emitter coupled switch or a "Data Reference" (Figure 4-5). This ensures that the  $I_B$  setting is unaffected by random fluctuations in the data stream or the duty cycle. If the temperature and aging characteristics of the laser diode are favorable, this may be a very efficient transmitter design. The typical "Mean Time Between Failure" for the laser diode that we are using is approximately 700 kHrs at 25°C, and about 420 kHrs at 45 °C. This implies that the temperature and aging characteristics are very good for the laser diode being employed.

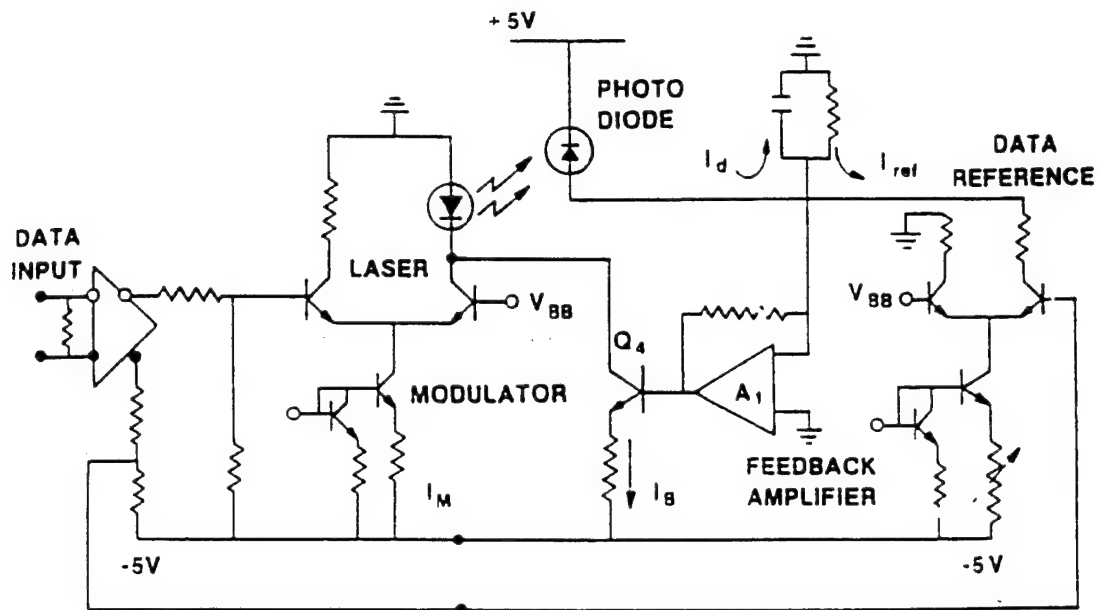


Figure 4-5  
Investigated Circuit for the Single-Loop Feedback. Transmitter for average optical power control.

#### 4.4 Electronic Encoder/Decoder Design

Recently, the speed of electronic serial data transmission lines has increased to over 1 Gb/s. Thus, it is now economical to multiplex a longer number of logic lines (~32 bit bus) onto a single high speed line. Conventional parallel data links are inefficient for this task, especially when considering the cost/performance issues of costly multi-conductor cables, radio frequency interference (RFI) suppressers, and bit-to-bit skew.

Recent technological advances have altered the cost/performance trade-offs between serial and parallel data transfer techniques. A new chip set from TriQuint semiconductor, called Hot Rod™, can achieve very high-speed data rates (over 1 Gb/s). The Hot Rod™ chip set provides the means to establish a transparent high-speed serial link between two high performance parallel buses. The chip set provides parallel-to-serial and serial-to-parallel conversion, with the addition of a 8B/10B coding scheme and serial transmission rates between 200 Mbit/sec to 1 Gb/s. The chip set also has the capacity to multiplex up to 40 bus lines. Assuming a standard 32 bit data bus, the single bus speed can be as high as 33 MHz and still be carried on a single optical line.

A schematic diagram of the communication system is shown in Figure 4-6.

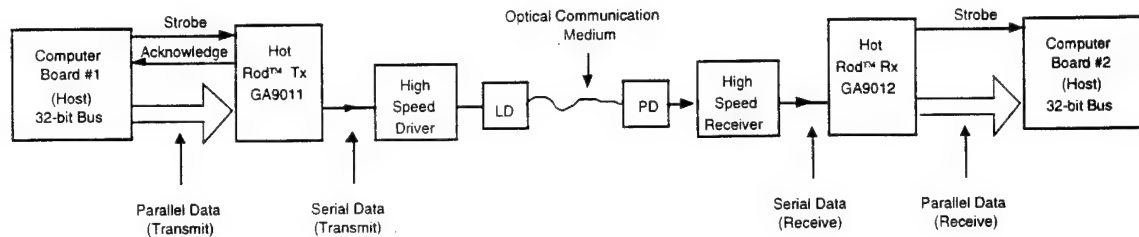


Figure 4-6  
Block Diagram of Optical Communications Using the Multiplexing of a 32 bit Bus

Each Hot Rod™ chip set contains one Hot Rod™ transmitter and one Hot Rod™ receiver, and provides a unidirectional 1 Gbit/sec communication capability. The chip set can be considered as a 40 bit parallel register. The transmitter accepts a 40 bit word of TTL-level data, and then multiplexes and encodes it on a single serial output. The receiver decodes the data and provides serial-to-parallel conversion, and finally outputs the 40 bit parallel word on its TTL level bus. All of these operations, as well as the serial interface, are transparent to the system. The data transformations are shown in Figure 4-7(a) for the transmitter and 4-7(b) for the receiver.

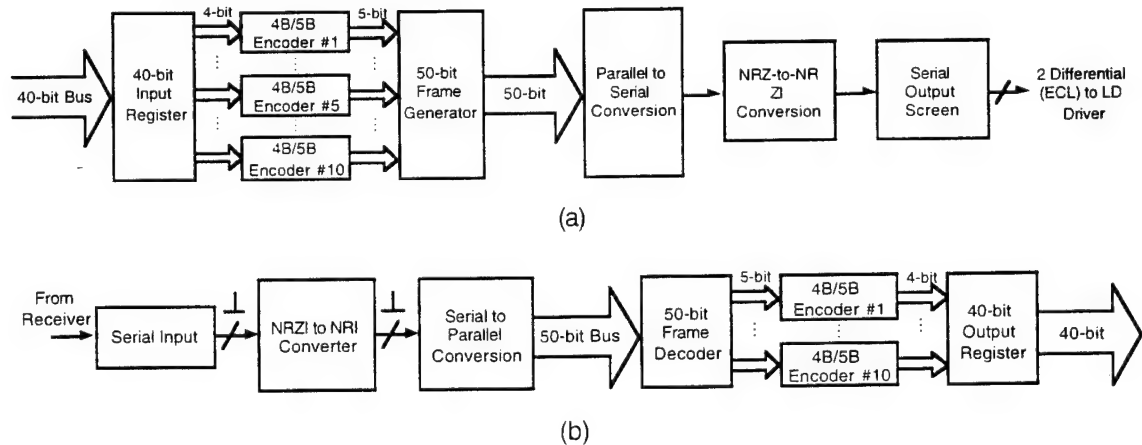


Figure 4-7  
Block Diagram of the Hot Rod™ (a) Transmitter and (b) Receiver

#### 4.4.1 Data Encoding and Decoding

Encoding and decoding of the non-return to zero (NRZ) data stream is required in order to provide clock recovery for high speed data rates. Most data transmission chip sets use codes such as 4B/5B, 8B/10B and 10B/12B. Here we present basics of 8B/10B encoding, available on the TriQuint chip set.

8B/10B encoding is performed in the subblocks, 5B/6B and 3B/4B. A block code of 8 bits of user data is divided into 5 bit and 3 bit subblocks. The blocks are code words for serial transmission. The user data is divided into 4 bit (3 bit) subblocks, where each subblock is encoded into 5 bit (4 bit) NRZ code words. Each encoded subblock code word can have

an equal number of ones and zeros (disparity = 0), more ones than zeros (disparity +2), and more zeros than ones (disparity -2).

The running disparity rule requires that the 4B/5B codes encode the user data in such a way that

1. a code word with disparity = 0 is used to uniquely represent a data segment, and
2. a code word with disparity +2 is its binary complement (with disparity -2) one used together to represent one segment of data.

The 8B/10B encoding example is shown in Table 4-1:

Table 4-1. 8B/10B Encoding Example

HEX user data:	72	10
Binary user data:	ABCDEFGH	ABCDEFGH
	01110010	00010000
Bit definitions	abcdefghij	abcdefghij
Initial RD	(-1)	
5B/6B Encode	010011 (-1)	
3B/4B Encode	1100 (-1)	
5B/6B Encode		01101 (+1)
3B/4B Encode		0100 (+1)
Final (RD)	(-1)	
Serial bit stream:	01001111000110110100	

The encoded serial data has 10 zeros and 10 ones, with a recurring disparity (RD) equal to -1.

#### 4.5 Transmitter Optimization

The heart of any transmitter is the power source and the modulation circuit. The speed of modulation is the most important criterion that determines the speed of the transmitter. In order to reduce power dissipation in an optoelectronic modulator circuit, the threshold current must be small. In addition, a wide bandwidth is necessary for multi-gigabit direct modulation [5].

##### 4.5.1 Simulation Analysis and Results

The circuit used in the simulation process is very close to the one shown in Figure 4-3 (the actual simulated circuit is shown in Figure 4-8). The ECL input is fed to the base of transistor Q<sub>1</sub>. Here, the laser diode is modeled as a pure resistance value of 10 ohms [6]. This model is a good approximation for frequencies of up to 500 MHz, but breaks down for very high frequencies where inductances and capacitances play an important role [6].

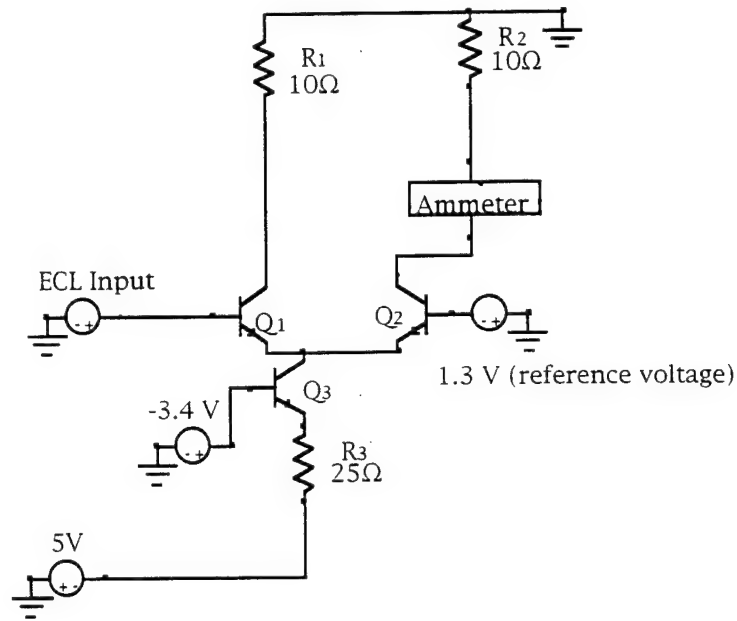


Figure 4-8  
Simulated Circuit of the Modulator With the Laser Diode Represented As a 10 Ohm Resistor

The change in modulation current with time is shown in Figure 4-9. The plot indicates that the modulation speed can be as high as 2 GHz. The peak value of the modulation current is close to 30 mA [6]. Figure 4-10 shows the ECL input and output voltages in a worst case scenario with the maximum value of the resistance of the laser diode chosen (10 ohms). Also note that the model is much more accurate, because the resistance value here is for a packaged laser diode (since the laser diode can be well approximated by a 5-to-10 ohm resistor [6])

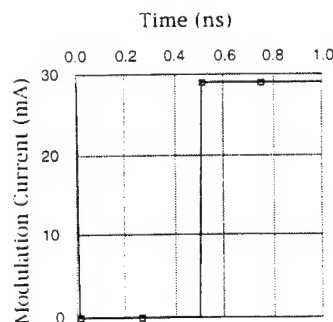


Figure 4-9  
Change in Modulation Current With Time For the Pure Resistor Model

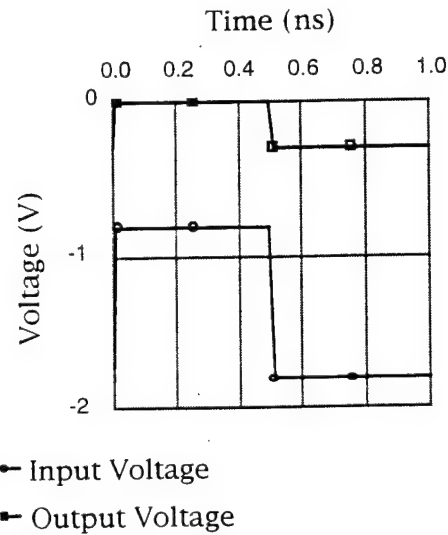


Figure 4-10  
Input and Output Voltage Levels (ECL) For the Pure Resistor Model

A second simulated example has the laser diode modeled as a combination of a 10 ohm resistor in series with an inductor, and in parallel with a capacitor (Figure 4-11). The values of the inductor and capacitor are chosen so that a 2 GHz modulation speed can be achieved, in order to obtain a model with a modulation speed of at least twice the value we need for our actual transmitter. Note that the inductor and capacitor values can be tailored to obtain even higher modulation speeds. Figure 4-12 shows the variation of the modulation current with time. The maximum modulation current is 30 mA.

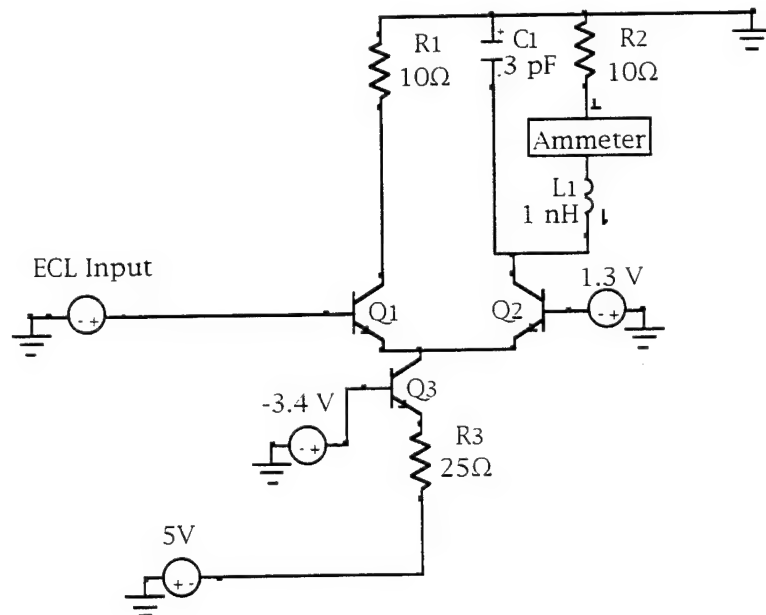


Figure 4-11  
Simulated Circuit of the Modulator With the Laser Diode Represented as a Resistor-Inductor-Capacitor Combination



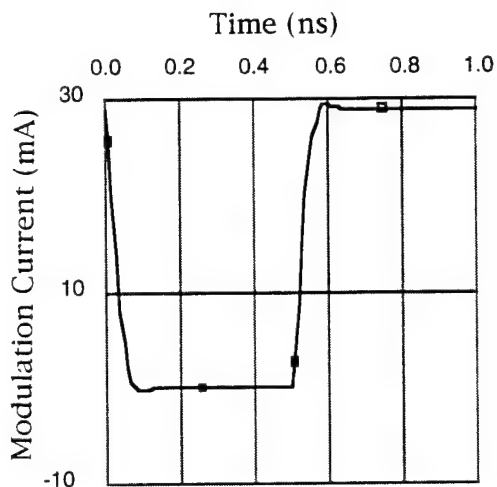


Figure 4-12  
Change in Modulation Current With Time For the Model in Figure 4-12

Notice that there is a slight overshoot of the modulation current beyond 0 mA, an indication of ringing in the circuit (Figure 4-12). Ringing is the overshooting of the current beyond its maximum or minimum value, due to impedance mismatches in the circuit. Care must be taken to minimize this effect in order to enhance modulator performance and efficiency. Frequency-related effects result in increasing the rise time of the modulation current when compared to the pure resistor model. This model is much closer to the real case, where the inductive and capacitive effects affect transmitter performance. As mentioned before, the input voltage is between -0.8 V and -1.8 V (ECL). Figure 4-13 shows how the output voltage tracks the input voltage.

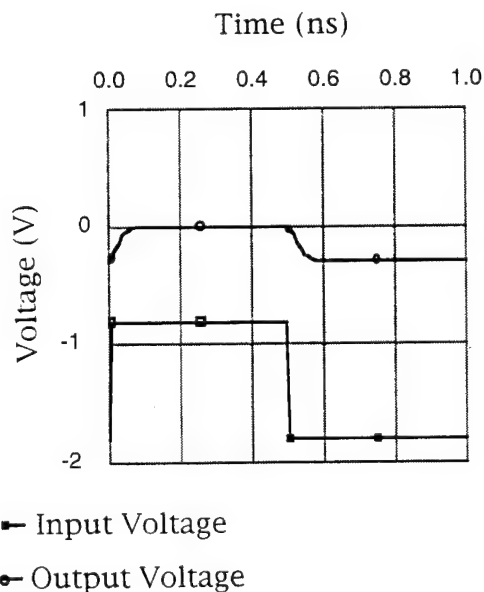


Figure 4-13  
Input and Output Voltage Levels (ECL) For the Model in Figure 4-11

#### 4.5.2 Transmitter Design Analysis

The block diagram of the transmitter shown in Figure 4-14 contains both modulation and optical output automatic power control (APC) circuitry. The data is input to the laser diode, then quantized by the modulation circuitry. The quantized data is then fed to the data reference generator and the laser driver, both of which are part of the modulation circuitry. The modulator circuit has a provision for providing a data reference signal to the APC circuit.

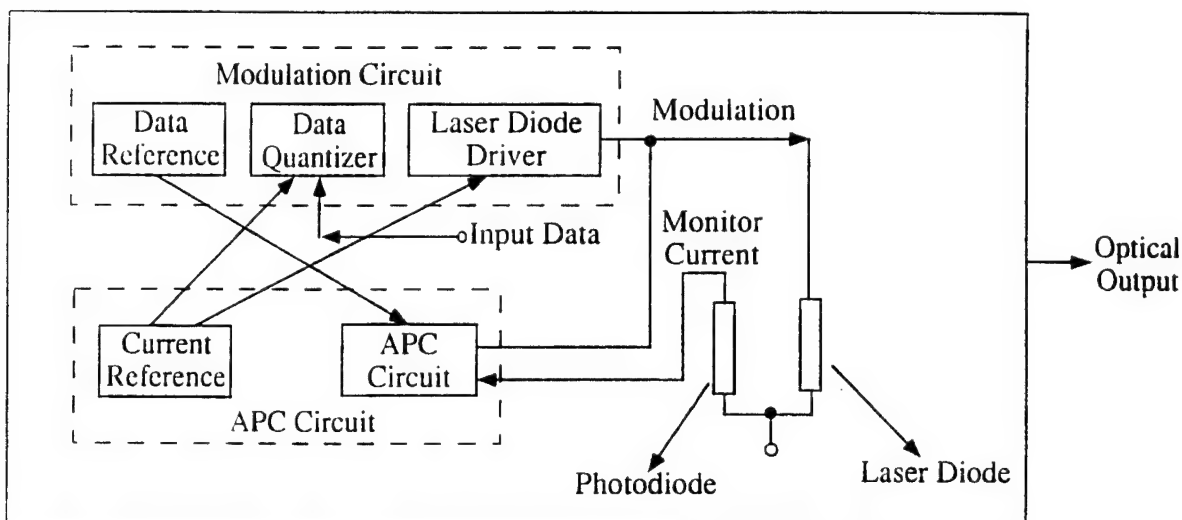


Figure 4-14  
Block Diagram of the Transmitter

There is a reference current that is supplied by the APC circuit to the modulator circuit. The APC circuit provides the bias for the laser diode. The modulation speed of the laser diode is limited by the turn-on delay, which can be minimized by biasing the laser diode at, or slightly above, the threshold current [4]. The optical output is monitored by a photodiode, whose output photocurrent is fed back to the APC circuit. The circuit diagram of the transmitter in Figure 4-15 clearly shows that the transmitter circuit is nothing but an extension of the direct current modulator. The automatic power control (APC) feedback loop on the bias current ( $I_B$ ) is additionally incorporated to monitor and control the optical output power. Op-amp  $A_1$  compares the monitoring photodiode's average current ( $I_d$ ) with a preset reference current  $I_{ref}$ . When the optical output changes,  $A_1$  alters the dc bias current  $I_B$  from the current source  $Q_4$ , until the output power is returned to its previous value. The modulated optical output can be used for any desired communication application.

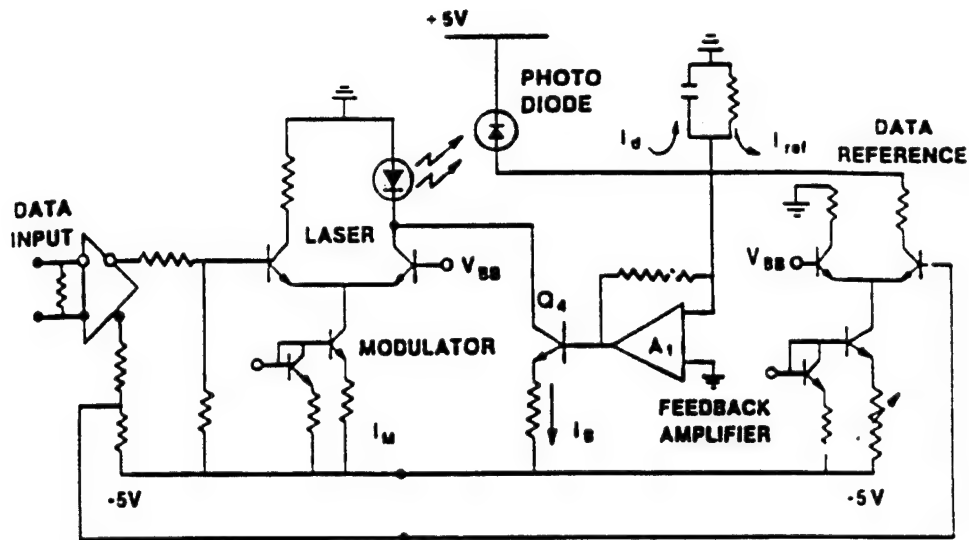
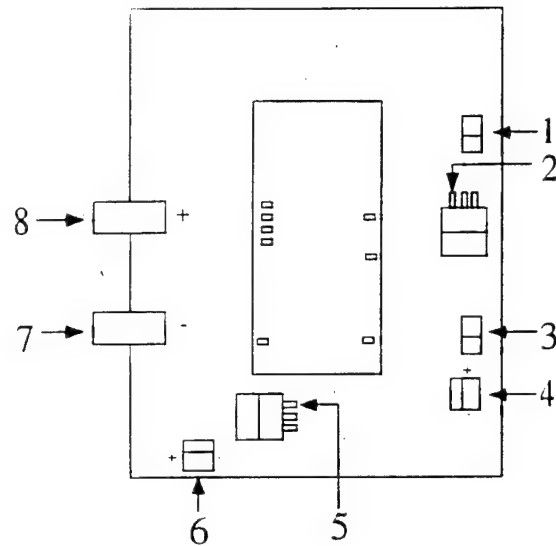


Figure 4-15  
Circuit Diagram of the Transmitter

#### 4.5.3 Experimental Setup and Results

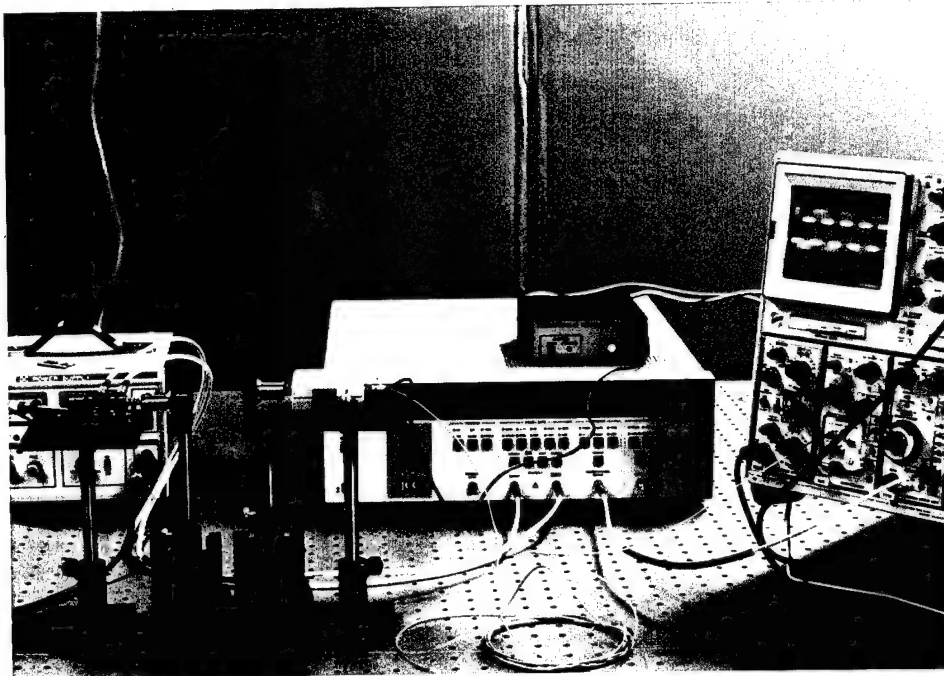
The transmitter module was integrated based on the design shown in Figure 4-15, and was then mounted on a printed circuit board (PCB) using the circuit diagram shown in Figure 4-16. The transmitter module is inserted into sockets on the board. The board has interfacing circuitry to ensure efficient operation. The design of the board, including connections to the power supply and the differential ECL data input are explained in Figure 4-16.



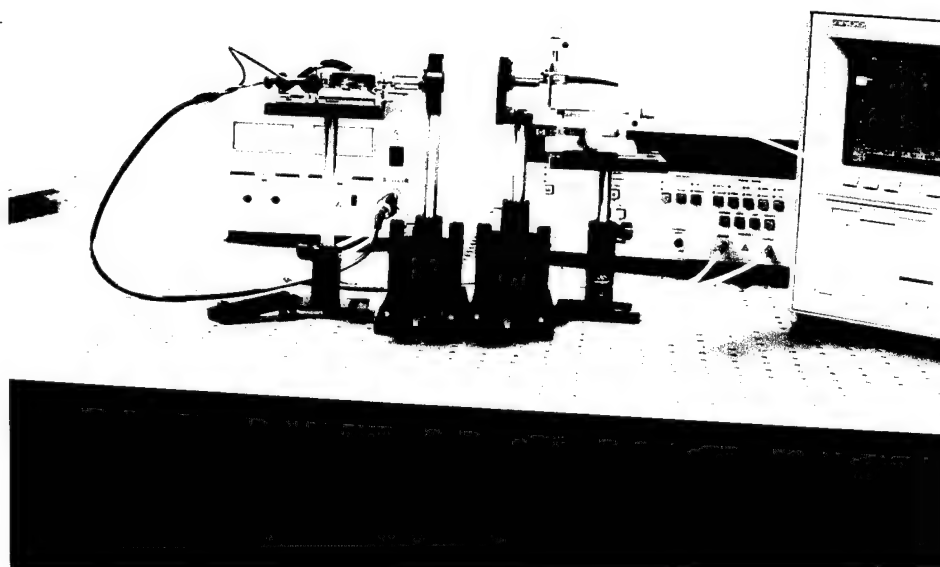
- 1 -2 Volt supply interrupt
- 2 Internal -2 Volt regulator output
- 3 -5.2 Volt supply interrupt
- 4 -10 Volt input
- 5 Internal -5.2 Volt regulator output
- 6 ECL reference generator output (-1.3 Volts nominal)
- 7 Negative differential ECL data input
- 8 Positive differential ECL data input

Figure 4-16  
Layout of the Printed Circuit Board

The transmitter needs a -10 Volt power supply for its operation. The input data is differential ECL, and is fed into the transmitter via SMA connectors from a HP-8133A pulse generator. The optical output is fed into a Tektronix SA-42 optical-to-electrical converter. It should be noted that the optical-to-electrical converter has a very reliable output response up to 2 GHz. The converter output is given to a high speed S-6 sampling head, which is plugged into a 7904 Tektronix oscilloscope. Figure 4-17(a) is a photograph of the setup that was used to measure the data rates (electrical domain), and Figure 4-17(b) is a photograph of the setup that was used to measure the optical spectrum (optical domain). The output from the laser diode is collimated using an objective lens, then the light is focused onto the optical-to-electrical converter input using a second objective lens. Figure 4-17(c) is a close-up photograph of the transmitter module, the collimating and focusing lenses, and the optical-to-electrical converter (receiver). Figure 4-17(d) is a photograph of the magnified image, and shows the laser diode and the ferrule of the module shown in Figure 4-17(c). The light from the diode is coupled into the ferrule. Because the alignment between the laser diode and the ferrule is not perfect (Figure 4-17), there is a significant amount of coupling loss, and the output power is considerably reduced as a result. Table 4-2 lists all equipment used in the experimental setup.



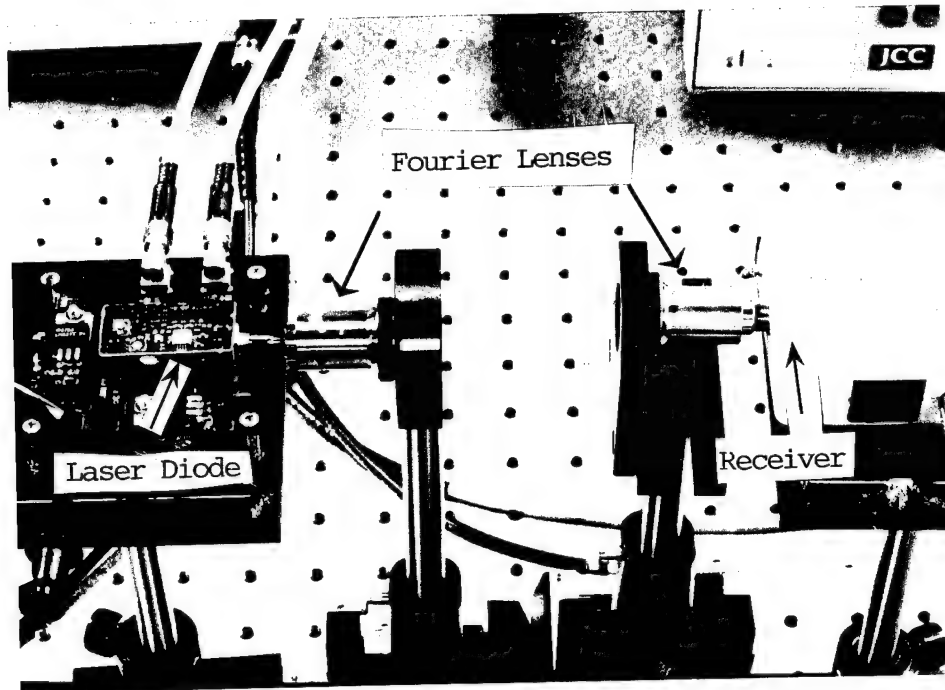
(a)



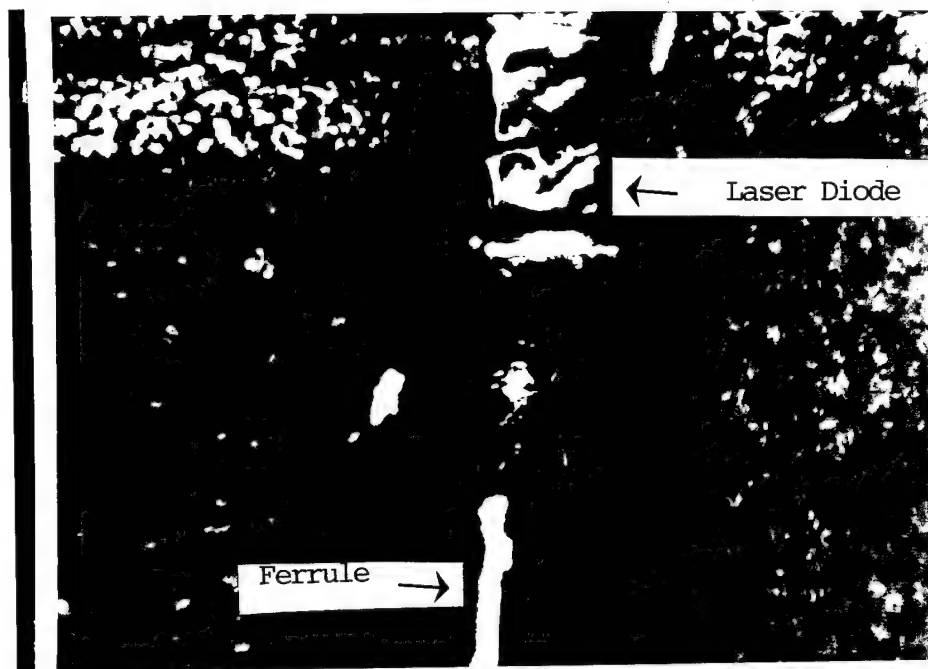
(b)

Figure 4-17

(a) Photograph of the Experimental Setup for Measuring the Data Rates; (b) Photograph of the Experimental Setup for Measuring the Optical Spectrum



(c)



(d)

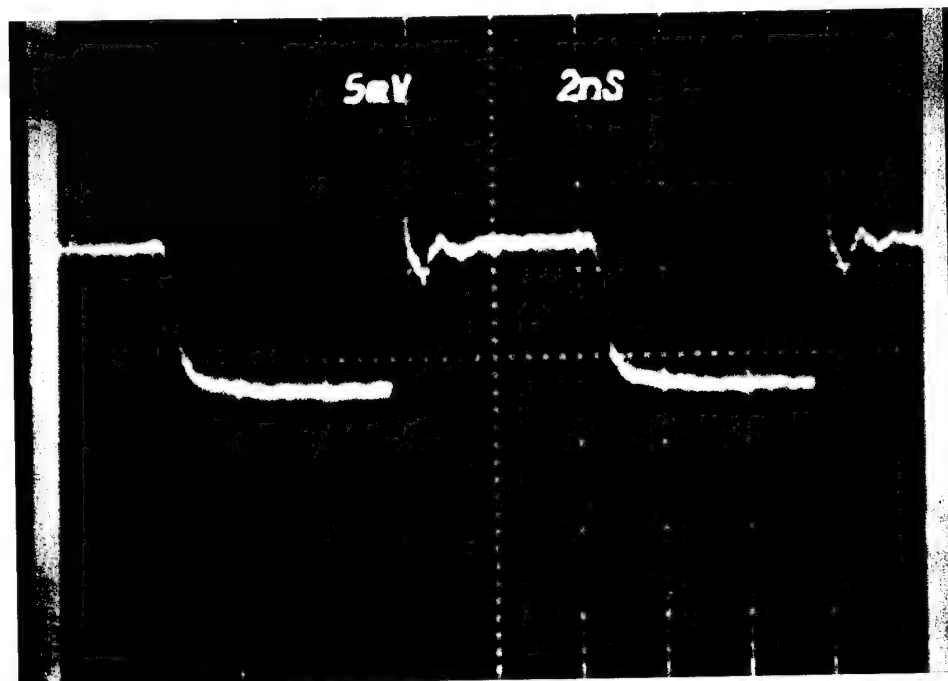
Figure 4-17

(c) Closeup Photograph of the Portion of the Setup, Showing the Transmitter Module, Collimating and Focusing Lenses and the Optical to Electrical Converter. (d) Photograph Showing the Packaging of the Laser Diode and the Ferrule into which the Light from the Laser Diode is Coupled.

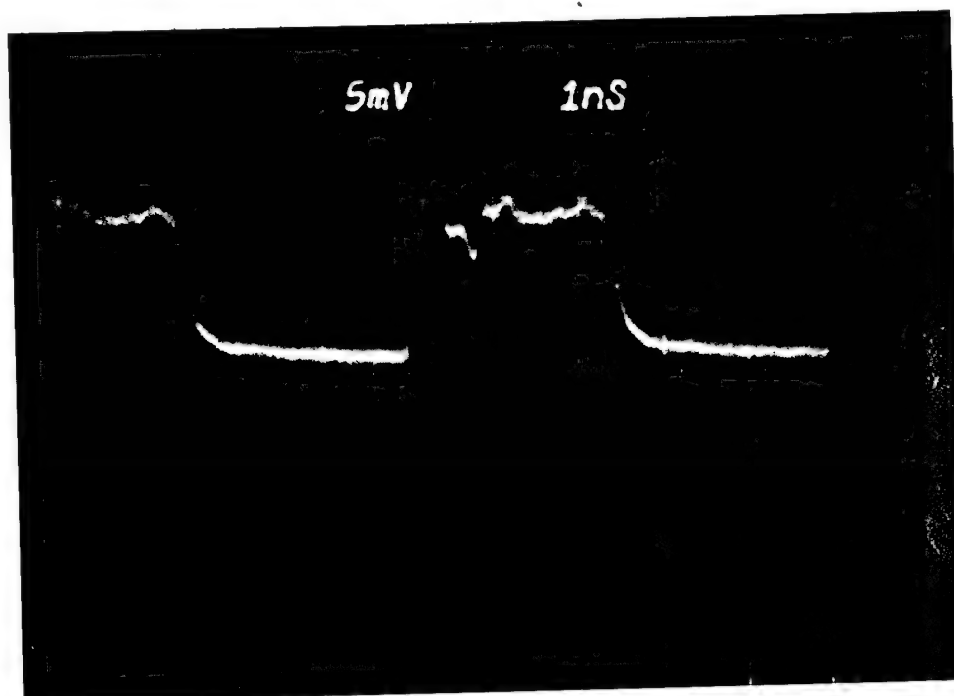
Table 4-2. List of all the Equipment Used in the Experimental Setup.

Equipment Used in the Experimental Setup
HP- 8133A Pulse Generator
Tektronix SA-42 Optical to Electrical Converter
Transmitter Module
Printed Circuit Board
-10 Volt Power Supply
7904 Tektronix Scope with S-6 Sampling Head
ANDO-AQ-6312B Optical Spectrum Analyzer
HP-8152A Optical Average Power Meter
SMA, BNC, SC and FC Connectors and Cables

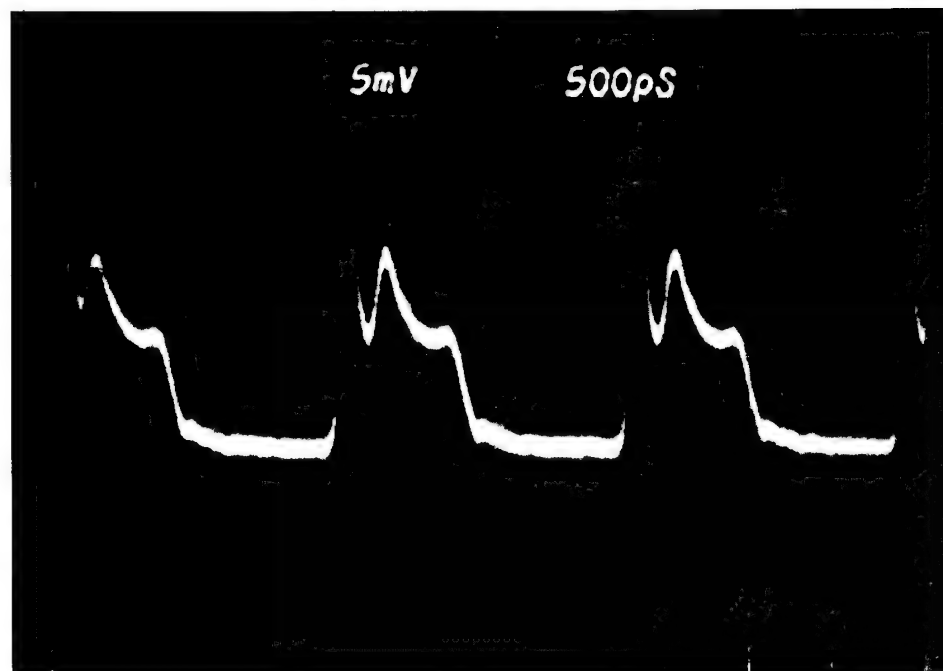
A Polaroid camera was employed to photograph the output waveforms from the oscilloscope CRT screen. Photographs at different data rates (200 Mb/s, 400 Mb/s, 600 Mb/s, 800 Mb/s, 1 Gb/s, 1.2 Gb/s and 2 Gb/s) are shown in Figures 4-18 (a-g). Since the input is a square wave, one period corresponds to two data bits (Figure 4-20), implying that a 500 MHz square wave corresponds to a data rate of 1 Gbit/s for Non Return to Zero (NRZ) binary signals. The maximum optical output power (continuous wave) from the laser diode in the transmitter is 180  $\mu$ W (-7.5 dBm). This was measured using an HP-8312A optical average power meter.



(a) 200 Mb/s

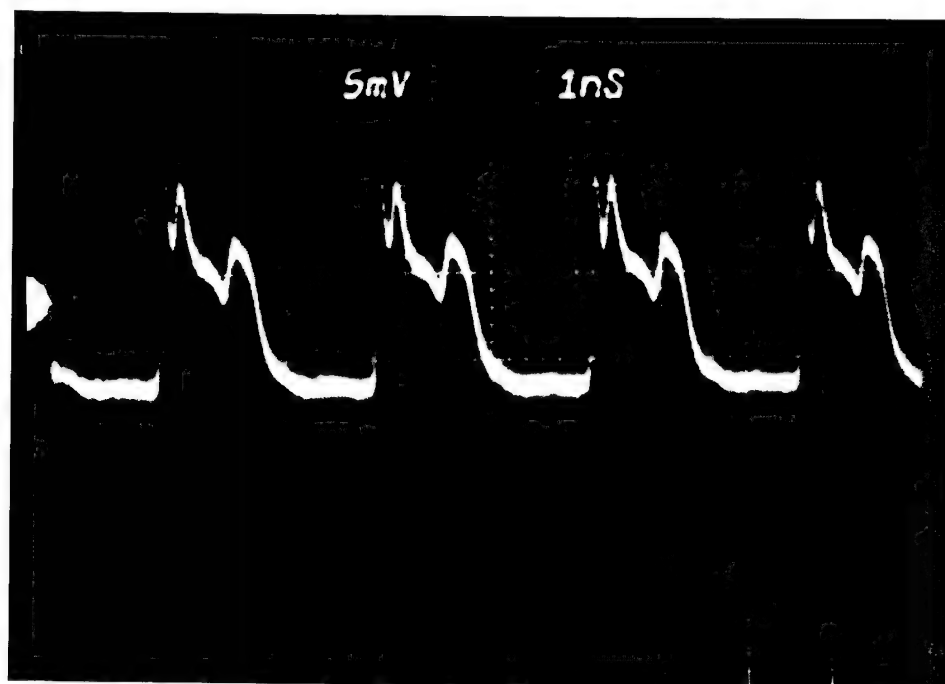


(b) 400 Mb/s

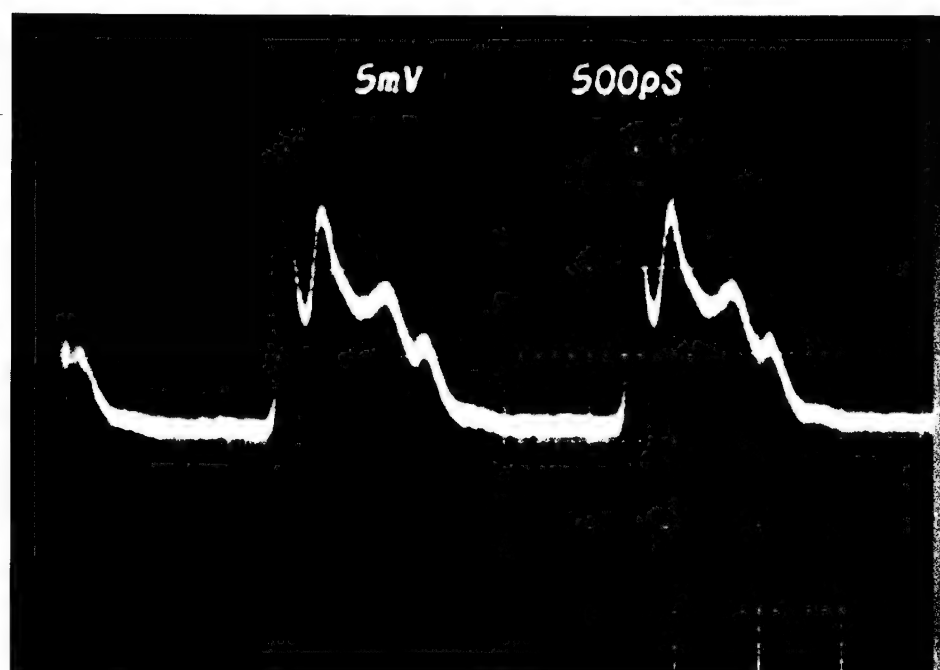


(c) 600 Mb/s

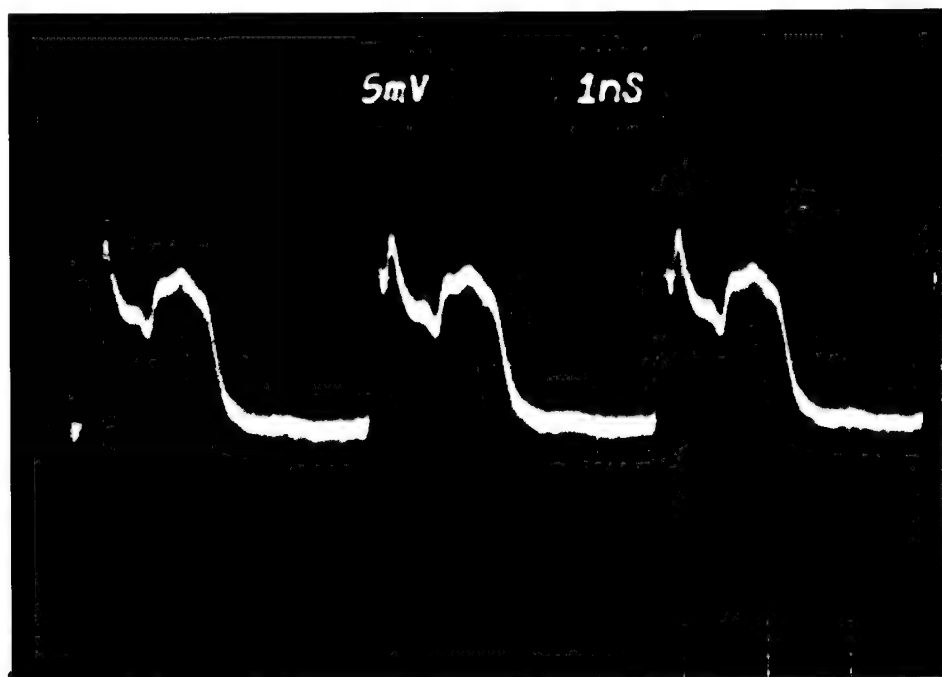




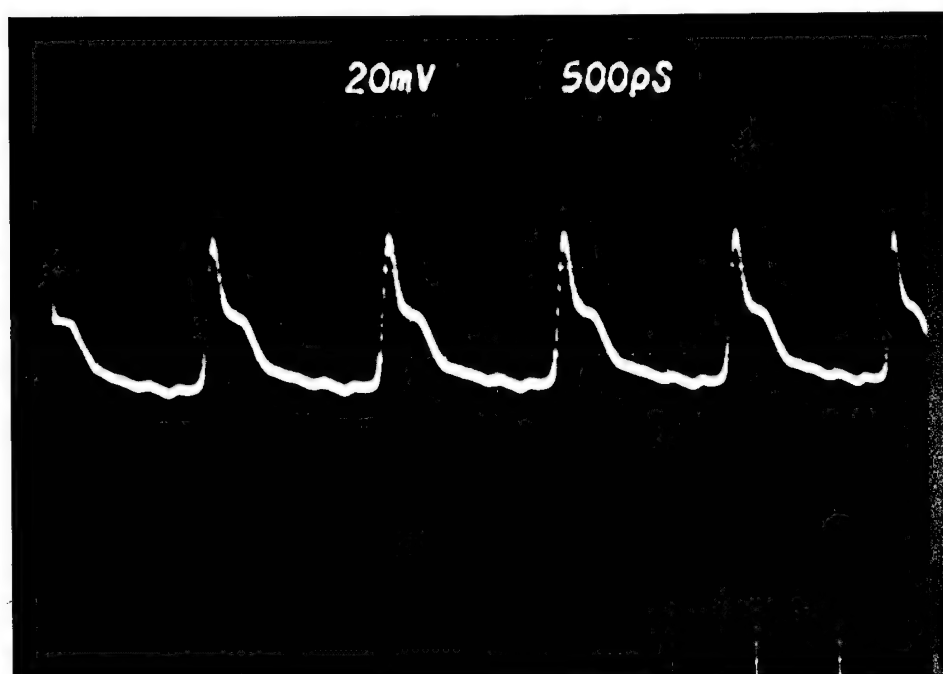
(d) 800 Mb/s



(e) 1 Gb/s



(f) 1.2 Gb/s



(g) 2 Gb/s

Figure 4-18  
Transmitter Output at Different Data Rates

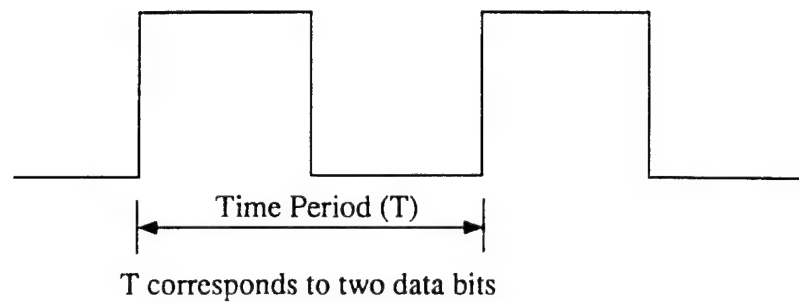
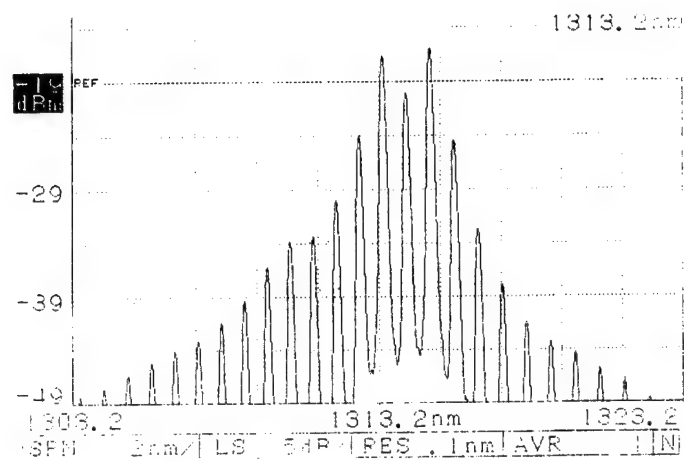
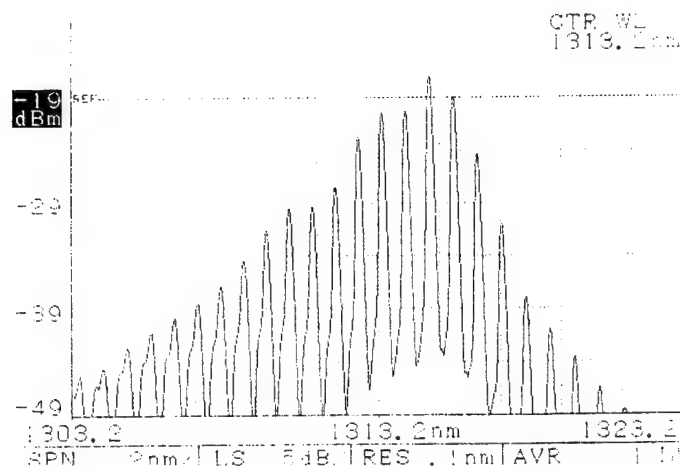


Figure 4-19  
Schematic Depicting the Presence of 2 Data Bits in One Time Period of a Square Wave

A spectral analysis of the transmitter output was also performed using an optical spectrum analyzer (ANDO-AQ-6312B) to observe changes in the output spectrum with changes in the modulation frequency. The optical spectrum showing the wavelength distribution without any modulation was observed (Figure 4-20(a)). Later, the optical output spectra at 100 MHz, 200 MHz, 300 MHz, 400 MHz, 500 MHz, 600 MHz, and 1 GHz was tested (Figure 4-20(b-h)). Shifts in the center wavelength can be clearly seen as the modulation speed increases.

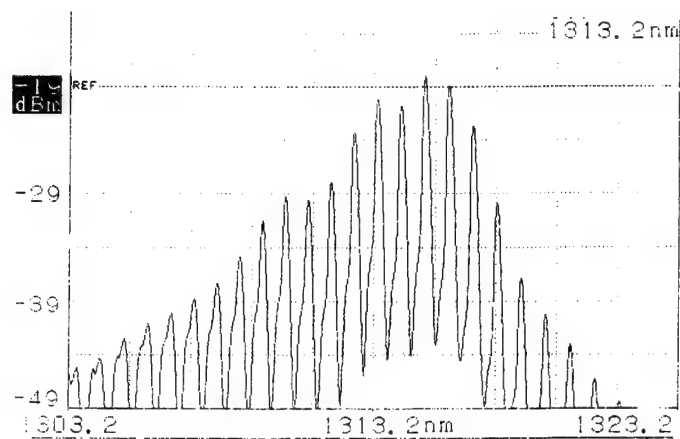


(a)

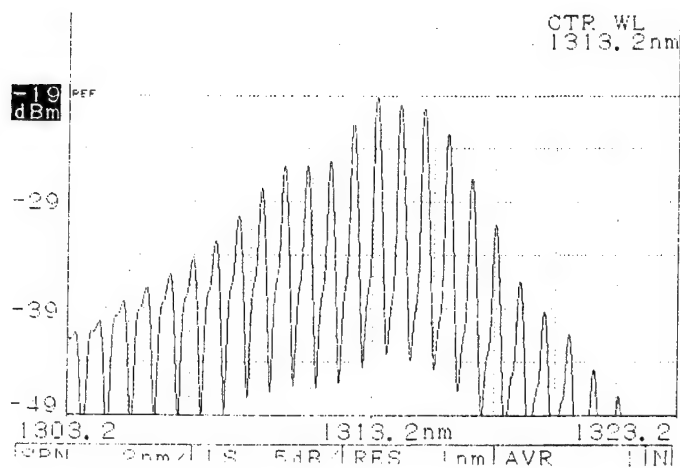


(b)

Figure 4-20  
Optical Output Spectrum at Different Data Rates. (a) Continuous Wave; (b)  
200 Mbits/sec

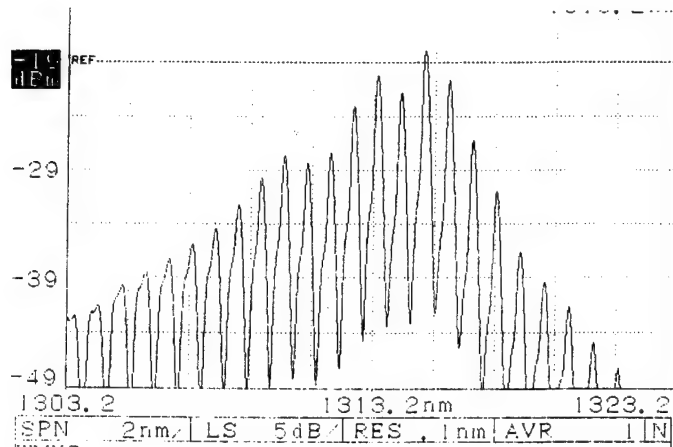


(c)

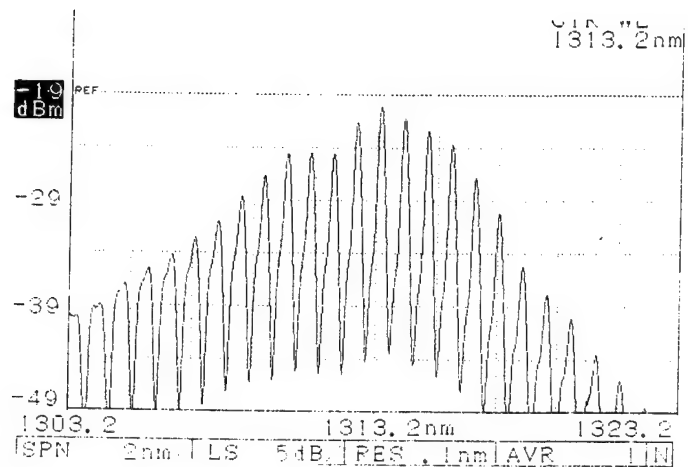


(d)

Figure 4-20  
Optical Output Spectrum at Different Data Rates. (c) 400 Mbits/sec, (d) 600 Mbits/sec

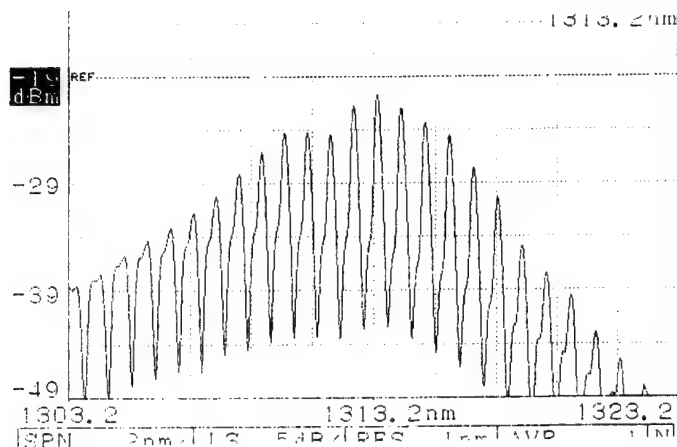


(e)

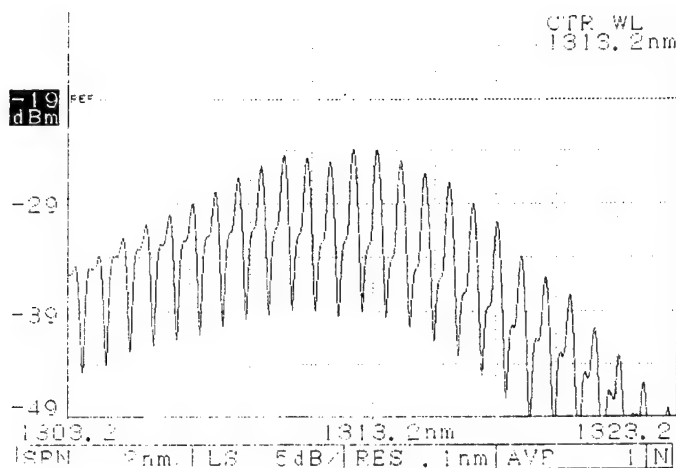


(f)

Figure 4-20  
Optical Output Spectrum at Different Data Rates. (e) 800 Mbits/sec, (f) 1 Gbit/sec



(g)



(h)

Figure 4-20  
Optical Output Spectrum at Different Data Rates.  
(g) 1.2 Gbits/sec and (h) 2 Gbits/sec.

## 5.0 BI-DIRECTIONAL OPTICAL BACKPLANE BUS

The limitations of current computer backplane buses stem from their purely electronic interconnects. In massively parallel architectures, the performance is limited by the limited bandwidth of currently available interconnection networks [7]. The results of important

design considerations, such as architecture, actual fabrication considerations, analysis of the holographic diffraction condition, and fan-out intensity optimization for the bi-directional optical backplane bus are presented in this section. The power budget constraints of a transceiver that incorporates a bi-directional optical backplane bus operating at 500 MHz are also discussed.

Figure 5-1 shows the optical equivalent of a single bi-directional electronic bus line. The drive current provided by each optoelectronic transceiver powers the corresponding laser diode, whose output is bi-directionally coupled through a multiplexed waveguide hologram and into the substrate, which itself is optically transparent and therefore functions as the medium for the backplane bus array. The surface-normal fan-out is provided by a linear hologram array located between the backplane and the processor/memory boards. Each photodiode associated with a transceiver detects light from either hologram array. This is because the light travels in both directions in the waveguiding plate shown in Figure 5-1.

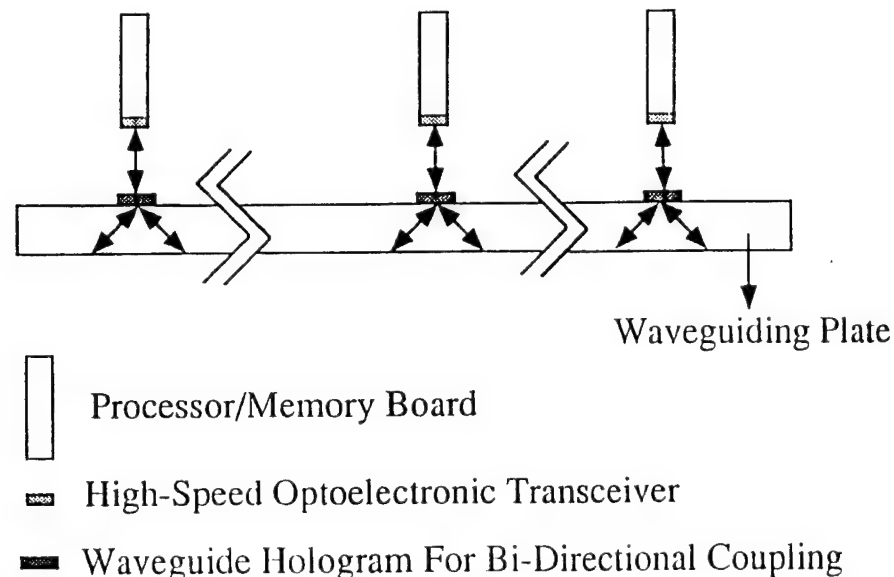


Figure 5-1  
Optical Equivalent of a Section of a Single Bi-Directional Electronic Backplane Bus Line

Figure 5-2 shows the optical bus used as a backplane in a high performance multi-processor optoelectronic computer. There must be bi-directional signal flow between the backplane and the processor/memory boards, where the multichip modules (MCMs) are located. The design we employed in this program enables the optical bus to serve as a bi-directional backplane. Multiplexed waveguide holograms are employed to facilitate two-way communication between boards connected to the backplane. The enlarged portion of Figure 5-2 shows a section of three bus lines bi-directionally interconnected through arrays of multiplexed waveguide holograms, where the bi-directionality of the interconnect is depicted.



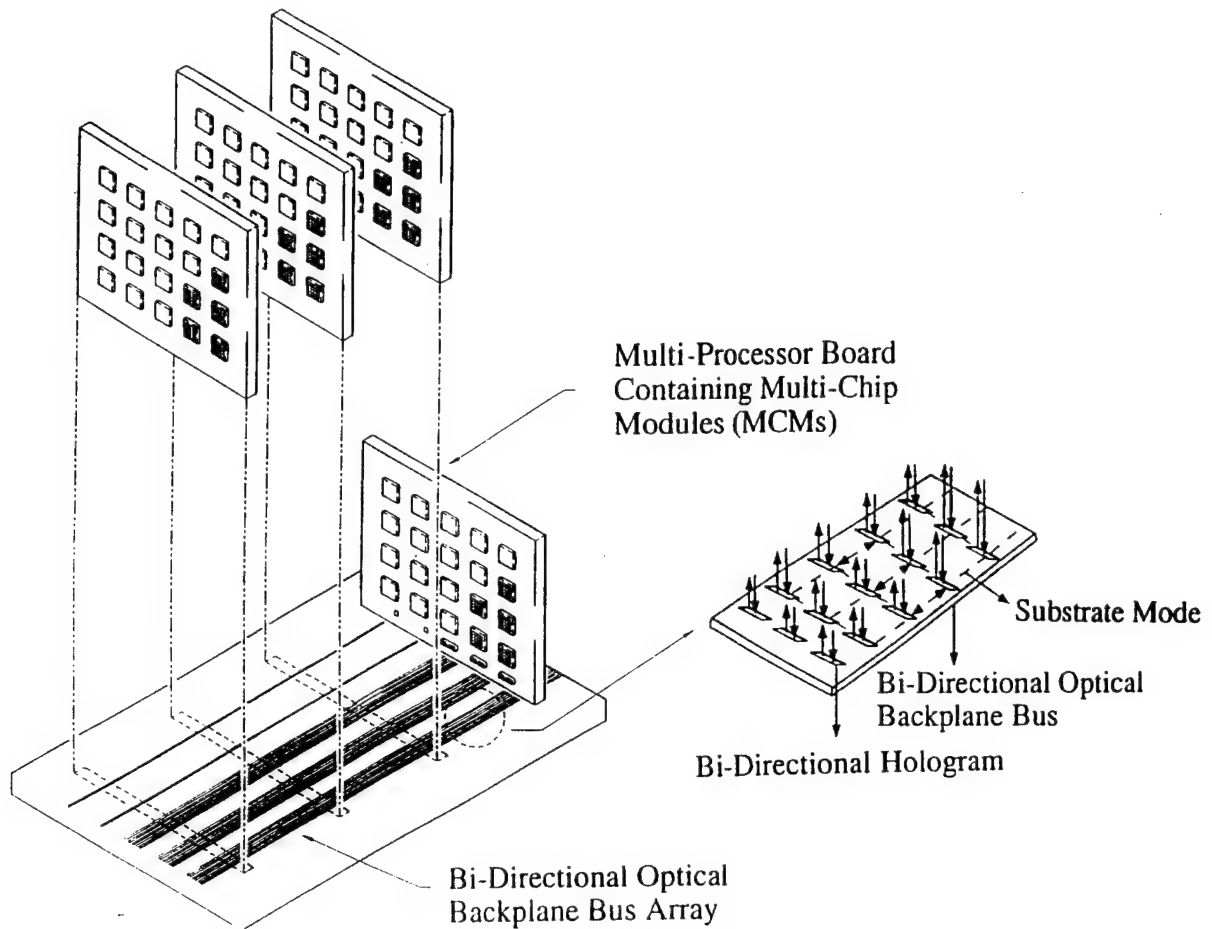


Figure 5-2  
Schematic of the Optical Bi-Directional Backplane Bus in a Multi-Processor System

The desired signal is coupled into the backplane bus through a TIR hologram, which is designed to provide a total internal reflected beam within the guiding plate. An array of fan-in/fan-out holograms are recorded along each line (Figure 5-2).

The functionality of the bi-directional backplane bus is well understood by its application in a transceiver system. By employing the holographic bi-directional bus, each cardboard can send and receive information to and from every other cardboard in the system. Note that cascaded fan-out is employed in all of the communications. The control and data signals are broadcast to all of the cardboards associated with the high performance, multi-processor computer. The correct response from another processor or memory board is based on address identification.

### 5.1 Fabrication Considerations for the Optical Backplane Bus

The physical layer of the optical backplane bus is essentially a thin waveguiding plate with a set of 1-D holograms integrated on its surface. The substrate serves as the light-guiding medium. We experimented using Dichromated Gelatin (DCG) and DuPont photopolymer in conjunction with the substrate. DCG processing after recording is wet [5], while the

DuPont polymer is a dry process [8]. The recording wavelength used is 488 nm. The device operates at 850 nm.

An array of multiplexed waveguide holograms is employed to provide a fully interconnected bi-directional optical bus. A total internal reflection (TIR) hologram is designed to couple the surface normal laser beam into a substrate guided beam with a pre-designed bounding angle (45° in our case). The second type of hologram couples an array of substrate guided beams into a 1-D array of surface-normal fan-out beams [9] with a specific coupling efficiency.

## 5.2 Analysis of Diffraction Conditions for the Holographic Bi-Directional Optical Backplane Bus

A volume holographic grating is described as a grating that produces Bragg diffraction and exhibits strong angular and wavelength selectivity [10]. For a light beam with a wave vector  $\bar{k}$  incident on a grating with grating vector  $\bar{K}$ , efficient wavefront reconstruction occurs if

$$\bar{k} = \bar{k} - \bar{K} \quad (5-1)$$

where  $\bar{k}$  is the wavevector of the diffracted beam.

Light propagation in the optical backplane bus is actually a series of consecutive diffraction and reflection processes. After recording the two sets of hologram arrays, two grating vectors,  $\bar{K}_1$  and  $\bar{K}_2$ , are formed in the film (see Figure 5-3(a)). When a surface-normal light beam with wavevector  $\bar{k}$  is incident onto the surface of the film, the two Bragg diffraction conditions occur if

$$\bar{k}_1 = \bar{k} - \bar{K}_1 \quad (5-2)$$

$$\bar{k}_2 = \bar{k} - \bar{K}_2 \quad (5-3)$$

where  $\bar{k}_1$  and  $\bar{k}_2$  are two diffracted beams generated by the two sets of holographic gratings. The incident light beam is then converted into two substrate modes propagating in two opposite directions (Figure 5-3(b)).

However, when the substrate guided waves interact with the gratings on the upper surface as shown in Figure 5-3(c), they also satisfy the Bragg condition for one set of the gratings. As a result, a portion of the light beam will be diffracted out of the substrate, giving rise to a surface-normal fan-out beam  $\bar{k}_{upper}$  (Figure 5-3(c)). The other portion continues to propagate within the substrate, hitting another set of hologram gratings, resulting in another downward, surface-normal fan-out  $\bar{k}_{down}$ . The zig-zag guided substrate waves go through many iterations of this cascaded fan-out process until they hit the last holographic element.

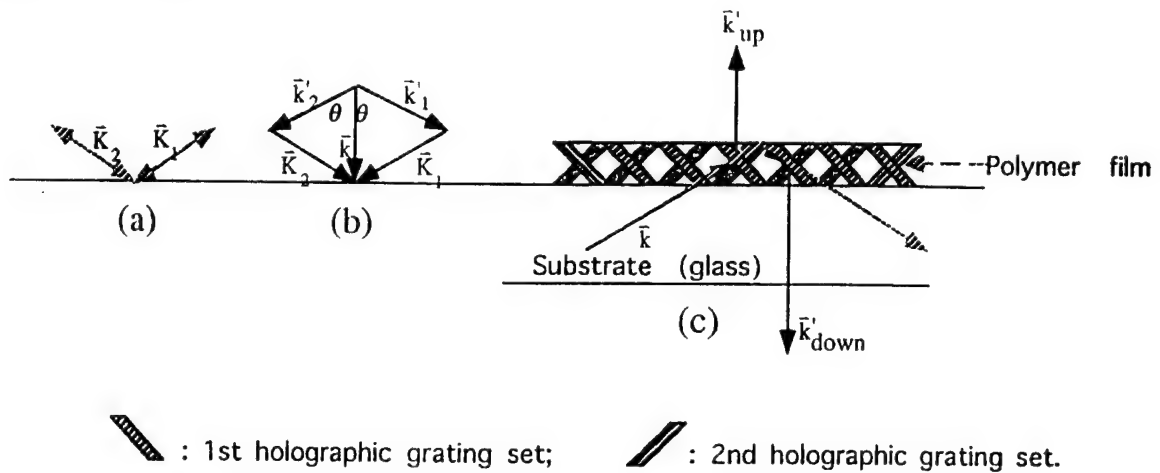


Figure 5-3

Diffraction Mechanism of Light in by Two Sets of Hologram Gratings Recorded on A Glass Substrate. (a) Two grating vectors recorded; (b) light diffraction geometry by the gratings; and (c) light transmission, diffraction and reflection inside the bi-directional backplane bus.

From the the above analysis, the bi-directionality of the optical bus is obvious. We also see that the fan-out intensity distribution should have a cascaded fan-out nature, away from the incident channel.

### 5.3 Optimization of the Five Channel Optical Backplane Bus

As the substrate guided waves propagate forward, their intensities will decrease after each fan-out. The intensity of each surface-normal fanout is determined by the diffraction efficiency of the corresponding holographic grating. By changing the diffraction efficiency distribution of the holographic grating arrays, we can manipulate the fan-out intensity distribution. It is impossible to achieve a uniform fan-out intensity distribution for all cases where the modulated optical signals are incident from different channels, because of the inherent bi-directionality of the optical bus. For example, a multi-processor system containing MCM modules requires  $n(n-1)$  interconnects to fulfill the broadcasting nature of the backplane bus protocols. Each module must be interconnected with the other  $n-1$  modules. A uniform fan-out intensity in the first module (which acts as the input module, and the rest as receiving ports) will make the power budget worse when this is reversed and the  $n$ th module is treated as the input and all the other ones as the outputs. In other words, the optimal design should provide us with minimized power fluctuations rather than equalized power distribution among  $n(n-1)$  interconnect scenarios.

Figure 5-4 shows a schematic of the bi-directional optical bus with 5 boards on side of the substrate. In both this figure and Figure 5-3(c), we assume that the diffraction efficiencies of the first hologram array, from left to right, is  $\eta_1, \eta_2, \dots$  and  $\eta_N$  from right to left. Note that  $N = 5$  in our case. To provide the optimized power budget, we must impose the following criteria:  $\eta_1 = 1$  and  $\eta_N = 0$ ; i.e., there is only one hologram at the first and the  $N$ th channels. If we denote  $P_{ij}$  to be the output power at the  $j$ th channel when light is incident from the  $i$ th channel, and the same holds for  $P_{ji}$ , except that they have a reversed propagating direction (Figure 5-4), we thus have

$$P_{ij} = 0 \quad (5-4)$$

whenever  $i = j$ .

$$P_{i1} = P_{iN} = 0 \quad (5-5)$$

where  $i = 1, \dots, N$ .

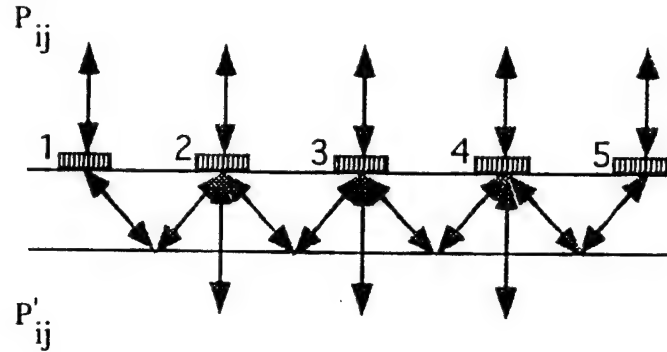


Figure 5-4  
Schematic of the 5-Channel Bi-Directional Backplane Optical Bus

Furthermore, the nature of the fan-out symmetry of the backplane bus also suggests that we shall consider only  $P_{ij}$  with  $i = 1, \dots, M$  ( $M = N/2$  when  $N$  is an even number, and  $M = (N + 1)/2$  when  $N$  is an odd number). According to the above mentioned analysis, for a digital optical signal incident from channel 1, the fanout intensities  $P_{ij}$  can be written as

$$\begin{aligned} P_{11} &= 0, \\ P_{12} &= \eta_1 \eta_{N-1}, \\ P_{13} &= (\eta_1 - P_{12} - P'_{12}) \eta_{N-2}, \\ &\dots \dots \\ P_{ij} &= \left[ \eta_1 - \sum_{k=2}^{j-1} (P_{1k} + P'_{1k}) \right] \eta_{(N+1)-j} \quad j = 3, \dots, N, \end{aligned} \quad (5-6)$$

while

$$\begin{aligned} P_{11} &= 0, \\ P_{12} &= (\eta_1 - P_{12}) \eta_2 \\ P_{ij} &= \left( \eta_1 - \sum_{k=2}^j P_{1k} - \sum_{k=2}^{j-1} P'_{1k} \right) \eta_j \quad j = 2, \dots, N-1, \\ P'_{1N} &= 0 \end{aligned} \quad (5-7)$$

Similarly, we can write the general expressions for  $P_{ij}$  and  $P'_{ij}$ ,  $i = 1, \dots, M$ ,  $j = 1, \dots, N$ ,

$$\begin{aligned}
 P_{im} &= \left[ \eta_{(N+1)} - \sum_{k=1-1}^{m+1} (P_{ik} + P'_{ik}) \right] \eta_m \quad m = i-1, i-2, \dots, 1, \\
 &\dots \dots \\
 P_{i(i-1)} &= \eta_{(N+1)-1} \eta_{i-1} \\
 P_{ii} &= 0 \\
 P_{i(i+1)} &= \eta_i \eta_{(N+1)-(i+1)} \\
 &\dots \dots
 \end{aligned}
 \tag{5-8}$$

$$P_{in} = \left[ \eta_i - \sum_{k=i+1}^{n-1} P_{ik} (P_{ik} + P'_{ik}) \right] \eta_{(N+1)-n} \quad n = i+1, \dots, N$$

and

$$\begin{aligned}
 P'_{i1} &= 0 \\
 P'_{im} &= \left( \eta_{(N+1)-i} - \sum_{k=i-1}^m P'_{ik} \right) \eta_{(N+1)-m} \quad m = i-1, i-2, \dots, 2 \\
 &\dots \dots \\
 P'_{ij} &= 1 - \eta_i - \eta_{(N+1)-i} \\
 &\dots \dots \\
 P'_{in} &= \left( \eta_i - \sum_{k=i+1}^n P_{ik} - \sum_{k=i+1}^{n-1} P'_{ik} \right) \eta_n \quad n = i+1, \dots, N-1 \\
 P'_{in} &= 0
 \end{aligned}
 \tag{5-9}$$

The optimization problem can now be stated. Our goal is to find a distribution of diffraction efficiencies which will lead to a fan-out intensity distribution as uniform as possible, regardless of which channel the light is incident. In the jargon of optimization theory, this wish (or goal) is called the objective function [11]. By optimizing (minimizing or maximizing) the objective function subject to certain constraints, a well balanced fan-out distribution can be reached. For our problem, an obvious objective function is the sum of the square value of the differences between the fan-out intensities and their average. If we assume the intensity of the incident beam is 1, and then taking into account of Eqs. (5-4) and (5-5), the average fan-out intensity should be

$$\bar{P} = \frac{1}{2N-3} \tag{5-10}$$

The objective functions are given below in Eqs. (5-11) and (5-12):

$$E_1 = \sum_{i=1}^M \left[ \sum_{\substack{j=1 \\ j \neq i}}^N W_{1ij} \left( \frac{P_{ij}}{\bar{P}} - 1 \right)^2 + \sum_{j=2}^{N-1} W'_{1ij} \left( \frac{P'_{ij}}{\bar{P}} - 1 \right)^2 \right] \quad (5-11)$$

and  $P_{ij}$  and  $P'_{ij} \geq \bar{P}$ .

$$E_2 = \sum_{i=1}^M \left[ \sum_{\substack{j=1 \\ j \neq i}}^N W_{2ij} \left( \frac{\bar{P}}{P_{ij}} - 1 \right)^2 + \sum_{j=2}^{N-1} W'_{2ij} \left( \frac{\bar{P}}{P'_{ij}} - 1 \right)^2 \right] \quad (5-12)$$

$$W_{1ij}^{(')} = \exp \left[ A \left( \frac{P_{ij}^{(')}}{\bar{P}} - 1 \right) \right] \quad (5-13)$$

$$W_{2ij}^{(')} = \exp \left[ B \left( \frac{\bar{P}}{P_{ij}^{(')}} - 1 \right) \right] \quad (5-14)$$

$W_{1ij}^{(')}$  is a weight factor,  $W_{2ij}^{(')}$  is a weight factor, and  $P_{ij}^{(')}$  is the general expression for the primed and unprimed power. A and B are iteration factors. The final objective function is the sum in Eqs. (5-11) and (5-12).

$$E = E_1 + E_2 \quad (5-15)$$

We know that by multiplying an appropriate statistical weight before each term of Eqs. (5-11) and (5-12), the square value of the difference between  $P_{ij}$  (or  $P'_{ij}$ ) and  $\bar{P}$  can be enlarged. After optimization, this difference can be brought down much more than the terms with a small statistical weight. That is, adding a statistical weight should give us a more optimized result. After comparing all the results thus obtained, we find the most optimized result. This idea can be realized by just assuming in Eqs. (5-11) and (5-12) that  $A \geq 0$  and  $B \geq 0$ , and alternatively changing the values of A and B.

An optimized fan-out distribution should result in a minimum value in the objective function E. Mathematically, this means that the first derivatives of E with respect to  $\eta_i$  ( $i=2, \dots, N-1$ ) are equal to zero; i.e.,

$$\frac{\partial E}{\partial \eta_i} = 0 \quad (5-16)$$

where  $i = 2, \dots, N-1$ .

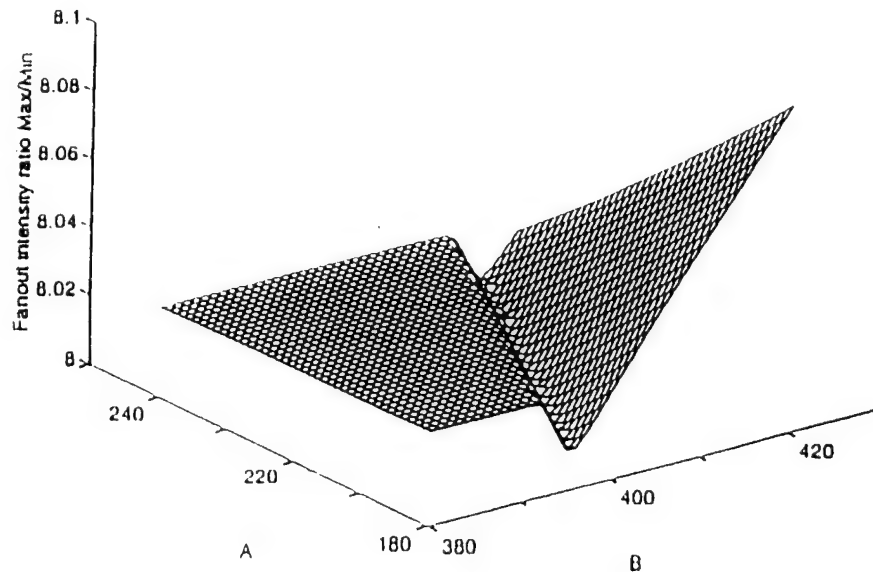
We have optimized the fan-out distribution for the case in which  $N = 5$ . A computer program has been implemented that computes the fan-out intensities and their first derivatives. The three nonlinear equations (Eq. (5-16)) are then numerically solved using the Levenberg-Marquardt algorithm and a finite-difference approximation to the Jacobian [9-12], subject to the constraints that

$$0 < \eta_2, \dots, \eta_4 < 1 \quad (6-17)$$

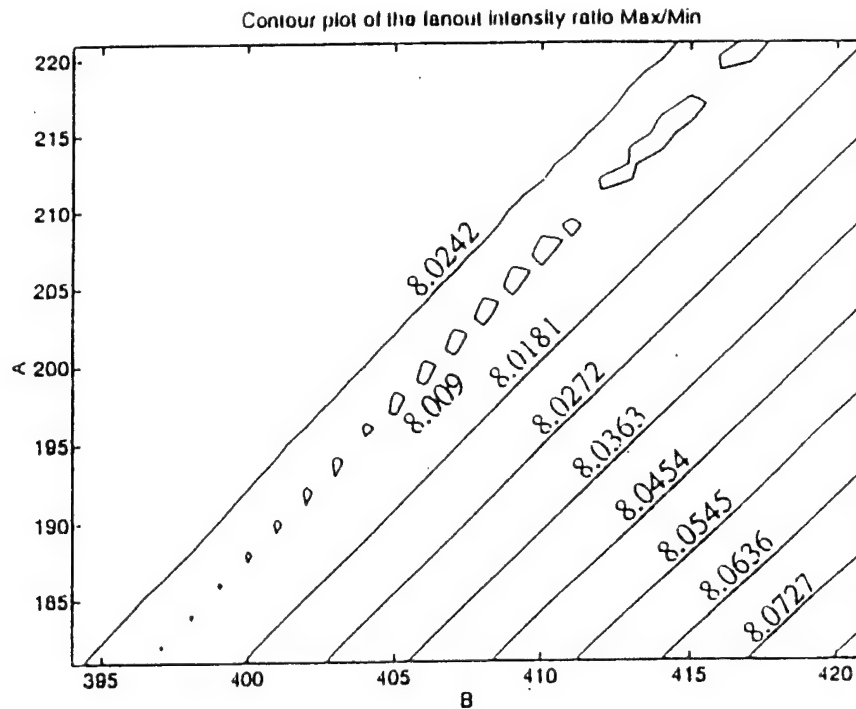
The change of the statistical weight is carried out in our calculation by alternatively increasing the  $A(\geq 0)$  and  $B(\geq 0)$  values. In Figure 5-5, we give the variation of the ratio between the maximum and minimum fan-out intensities with  $A$  and  $B$ . These values are obtained by comparing the "optimized"  $P_{ij}$ 's ( $i=1, \dots, 3, j=1, \dots, 5, i \neq j$ ) and  $P'_{ij}$ 's ( $i=1, \dots, 3, j=2, \dots, 4$ ) under a certain pair of  $A$  and  $B$ . With the limitation of our objective function  $E$  (Eq. (5-15)), the minimum value of this ratio will give us a globally optimized result (GOR). From Figure 5-5, we can see that our GOR should lie in the "valley" of this butterfly-shaped surface. By comparing the values at the bottom of this valley, we find that the optimization occurs at  $A = 210$  and  $B = 408$  with a max/min fan-out ratio of 8.009. The optimized diffraction efficiency distribution is calculated as

$$(\eta_1, \eta_2, \dots, \eta_5) = (1.0, 0.3336, 0.2500, 0.4992, 0.0) \quad (6-5)$$

and the optimized fan-out intensities are given in Table 5-1, in which  $P_1(i, j)$ 's are our  $P_{ij}$ 's, and  $P_2(i, j)$ 's are  $P'_{ij}$ 's. Because the average value of the fan-out intensities (from Eq. (5-10)) is 0.06667, we see that the minimum value of the fan-outs is very close to average. Furthermore, the maximum has more difference from it, due to the bi-directionality of the optical bus.



(a)



(b)

Figure 5-5  
Ratio Between the Maximum and Minimum Fanout Intensities as a Function of Coefficients A and B.

Table 5-1. Optimized Fan-out Distribution

Fan-out j	$P_{1j}$	$P'_{1j}$	$P_{2j}$	$P'_{2j}$	$P_{3j}$	$P'_{3j}$
1	0.0	0.0	0.4992	0.0	0.0835	0.0
2	0.4992	0.1671	0.0	0.1672	0.0834	0.08318
3	0.835	0.0626	0.0834	0.0626	0.0	0.4999
4	0.0626	0.0624	0.0626	0.0624	0.10834	0.0832
5	0.627	0.0	0.0626	0.0	0.0835	0.0

\*  $P_1(i,j) = P_{ij}$  and  $P_2(i,j) = P'_{ij}$

In the proposed bi-directional optical bus architecture, each board is affiliated with an optoelectronic transceiver. Each transceiver contains a laser diode that provides the input signal for the backplane bus, and a photodiode that receives the surface-normal fan-out signal from the backplane bus. The sensitivity of a photodiode detector is a function of laser power, modulation speed, bit error rate, and the wavelength of the signal carrier. For a PIN-FET photodiode with a quantum efficiency of 50% at 1.3 $\mu$ m, a data transfer rate of 1.2 Gb/s, and the required error probability after amplification of the detected signal of less than  $10^{-9}$ , the minimum modulated power required at the detector site is determined to be



$5.08 \times 10^{-5} \text{ W}$  [12]. For the optimized bi-directional optical bus, the simulation result gives an output efficiency of *about* 6.3%, which requires a minimum modulated input power of 0.8 mW.

#### 5.4 Project Specifications

The underlying specification of the project is to incorporate a 5 channel bi-directional optical backplane bus in a transceiver system. The basic idea is to couple a modulated light signal into the device through a particular channel and couple it out through a separate, different channel. The modulation frequency is specified to be 500 MHz.

#### 5.5 Experimental Bottleneck: Minimum Modulated Input Power Required at 500 MHz

The input into the holographic backplane bus is from a transmitter with a laser source operating at 850 nm. The modulating signal is a 500 MHz differential ECL (Emitter Coupled Logic) signal supplied by a high speed function generator. The output from the backplane bus is coupled into a receiver, whose output is in turn fed into an oscilloscope to observe the output waveform.

The calculations below illustrate that, with the provided input device, it is impossible to achieve the minimum required modulated input optical power for the successful operation of the device. In fact, even the unmodulated input power is so low that coupling enough light into the backplane bus in order to couple light out of even a single channel is impossible. The maximum unmodulated optical power from the transmitter is 130  $\mu\text{W}$ , far below the required amount to realize the device.

The signal-to-noise ratio (SNR) at the detector site is given by:

$$i_s / \langle i_n \rangle = P_s e \eta / h \nu / (4 k T_e \Delta \nu / R_L)^{1/2} \quad (5-19)$$

$P_s$  is the minimum value of the signal power required at the detector,  $e$  is the magnitude of the electronic charge,  $\eta$  is the detector quantum efficiency taken to be 0.5,  $h$  is the Planck's constant,  $\nu$  is the optical frequency (850 nm in our case),  $k$  is the Boltzmann's constant,  $T_e$  is the absolute temperature (with a value of 1160),  $\Delta \nu$  is the bandwidth (which is  $6.37 \times 10^8$  for a modulation frequency of 500 MHz, is our minimum stipulated frequency), and  $R_L$  is the load resistance, is calculated to be 83.3 ohms [12].

$P_s$  is the minimum signal power needed to exceed the signal-to-noise ratio of 11.89 [11]. This signal power is calculated to be  $2.43 \times 10^{-5} \text{ W}$ . The worst case output efficiency for an optimized device is calculated to be 6.3% from simulation results, for a five channel device [13]. So the minimum modulated input power required is  $2.43 \times 10^{-5} / 0.63 = 0.4 \text{ mW}$ . The maximum unmodulated optical power at our disposal is measured to be only 130  $\mu\text{W}$ . Thus, there is a lack of sufficient power budget for the successful operation of the device.

## 5.6 Experimental Results

In this report, we present a bi-directional optical backplane bus for a high performance multi-processor system, operating at 850 nm. The backplane bus employs arrays of multiplexed polymer-based waveguide holograms in conjunction with a waveguiding plate within which 7 substrate guided waves for 56 (7x8) cascaded fanouts, are generated. Data transfer of 1.2 Gbit/sec is demonstrated. Packaging-related issues such as transceiver size and misalignment are embarked upon, to provide a reliable system with a wide bandwidth coverage.

Figure 5-6 shows the functionality of the bi-directional optical backplane bus. A transceiver can be attached at each channel so that each channel can send and receive signals as well. There needs to be bi-directional signal flow between the backplane and the transmitter/receiver boards, where the multichip modules (MCMs) are located. Multiplexed waveguide holograms are employed to facilitate two-way communication between boards that are connected to the backplane.

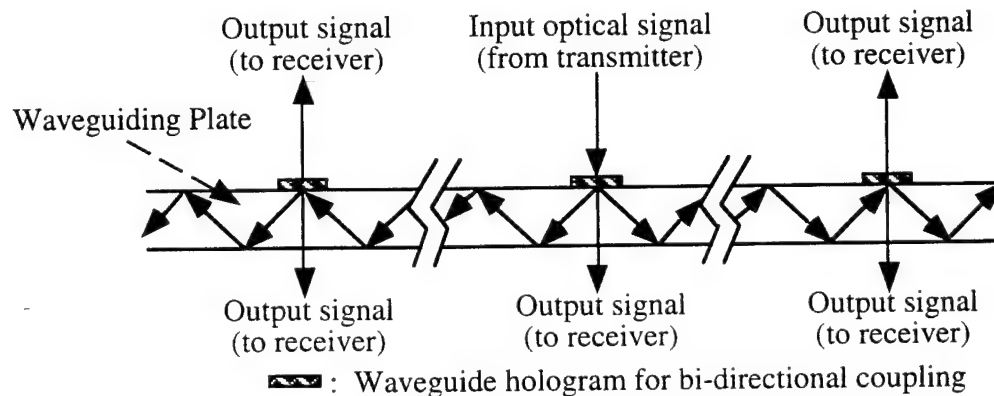


Figure 5-6  
Demonstration of the Functionality of Bi-Directional Optical Backplane Bus

The physical layer of the optical backplane bus is essentially a thin waveguide plate with an array of multiplexed holograms integrated on its surface. The substrate serves as the light-guiding medium. Dichromated gelatin (DCG) film is spin-coated on the surface of the substrate. For each bus line, two hologram arrays are recorded on the substrate afterward to provide the required bi-directional surface-normal coupling. The recording wavelength used is 488 nm. The fabrication process is optimized to provide reconstruction wavelength at 850 nm.

A schematic demonstrating the diffraction mechanisms of the bi-directional optical backplane bus is given in Figure 5-7. After having recorded the two sets of hologram arrays, two grating vectors,  $\vec{K}_1$  and  $\vec{K}_2$ , are formed in the film (Figure 5-7(a)). A surface-normal light beam with a wave vector  $\vec{k}$  is incident onto the holographic gratings. If the Bragg diffraction conditions are met, two diffracted light beams will be generated by the two holographic gratings and converted into substrate modes in two opposite directions (Figure 5-7(b)). During the subsequent transmission processes, whether the light beams hit a grating and the Bragg condition is met, part of the light beams will be diffracted surface-normally out of the backplane, while the remaining beams continue to propagate in the waveguiding plate (Figure 5-7(c)).

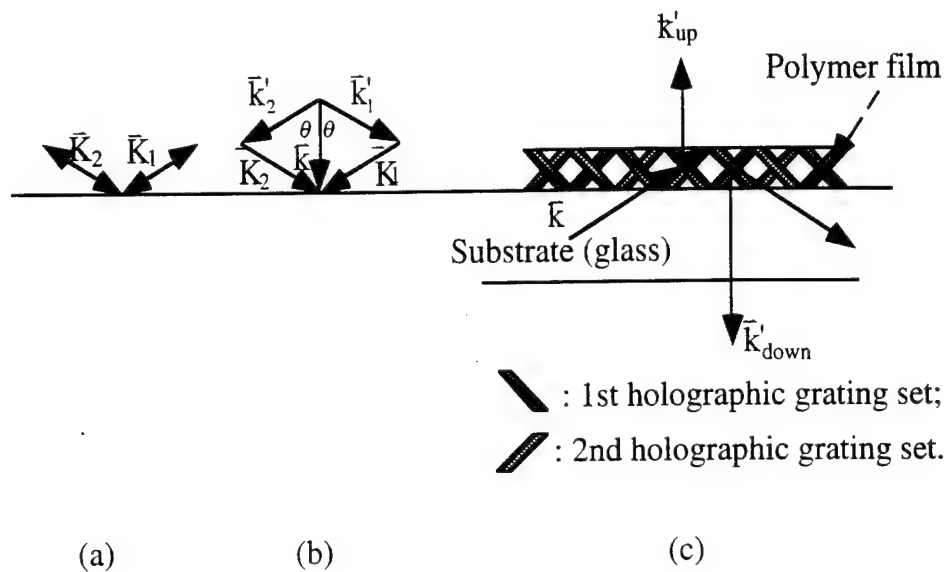


Figure 5-7  
Diffraction Mechanism of Light in by Two Sets of Hologram Gratings Recorded on a Glass substrated. (a) Two grating vectors recorded; (b) Light diffraction geometry by the gratings; and (c) Light transmission, diffraction and reflection inside the bi-directional backplane bus.

The main advantage of a bi-directional bus, as mentioned in the previous section, is its ability to provide a means for cascaded fan-out with signal flow in both directions. This concept is well illustrated in Figure 5-8. This figures shows an array of photographs taken from the bi-directional bus, in the surface-normal direction. These photographs are taken with one MCM board generating signals and all other eight boards serve as receivers. Various input/output combinations are delineated. Note that the input beam is not shown in Figure 5-8.



Figure 5-8  
An array of pictures of the fanout configurations, taken on the signal-incident side of the backplane, with the (a) 1st, (b) 2nd, (c) 3rd, and (d) 4th channel as the input coupler in the 1-to-7 bi-directional cascaded fanout optical backplane bus.

The final integrated demonstration setup containing the transmitter and the receiver is shown in Figure 5-9. In this figure, optical signal from a transmitter (FTM-8500) is coupled into a fiber and then is converted into a plane wave by a 1/4 pitch GRIN lens. After coupled out of the bi-directional optical backplane bus, the signal is coupled into another fiber using a fiber coupling stage and then is detected by a receiver (FRM-8500).

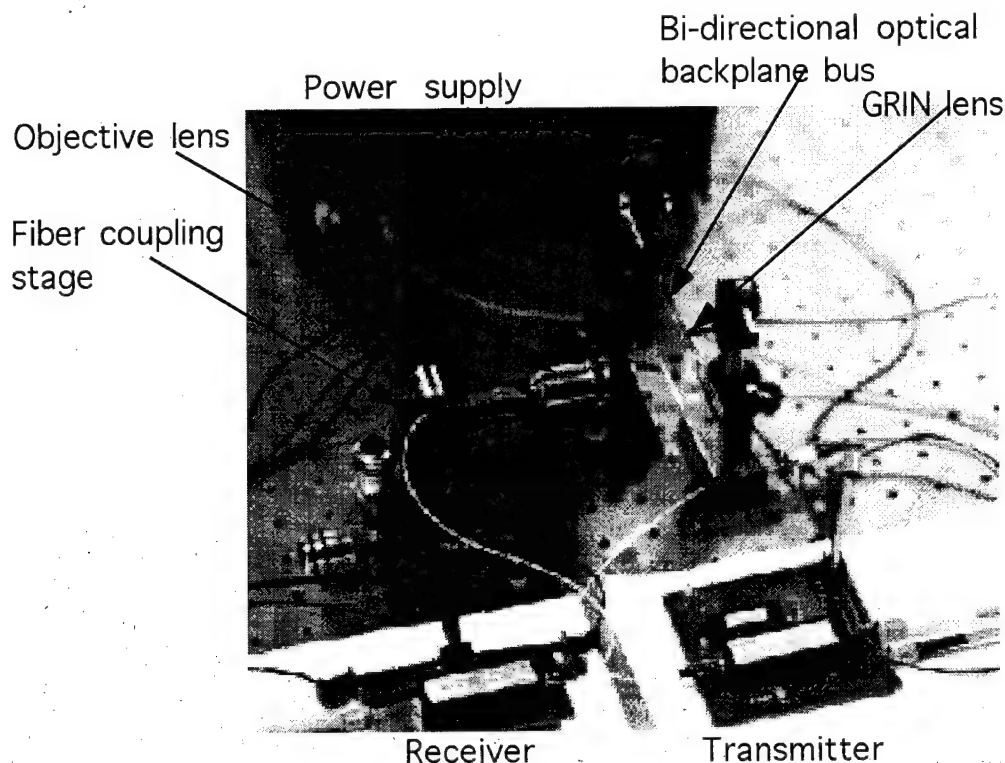


Figure 5-9  
Experimental Setup with the Bi-Directional Optical Backplane Bus Integrated with Transmitter and Receiver

A square wave input can illustrate the device performance in the digital domain. Figure 5-10 is a photograph of the device output with the input being a 600 MHz square wave or a 1.2 Gbit/sec digital signal. The input data is differential ECL and is obtained from a high speed pulse generator. A high speed sampling head is used in conjunction with an oscilloscope to display the output.

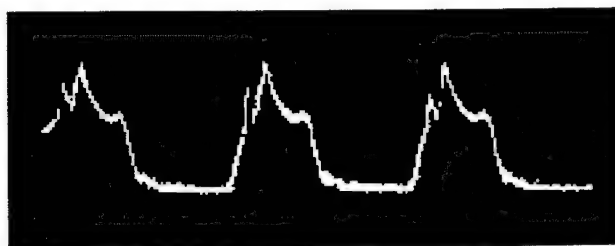


Figure 5-10  
Receiver Output From the Setup in Figure 5-9 for a 1.2 Gbit/s Input Signal

The change in intensity as a function of the fluctuation of the input coupling angle, from the input laser beam to the backplane bus plate, is measured. In our experiment, the angular fluctuation is defined as the angular coverage for 1 dB off the maximum intensity. This value, rather than the 3 dB points, is selected to provide a more reliable power budget for the system. Figure 5-11 shows the theoretical and experimental plots quantifying the

normalized intensity (efficiency) as a function of the angular misalignment. For the theoretical case, the overall efficiency is the product of the efficiencies of the input coupler and of the fanout hologram. This results in a closer resemblance to the experimental data, where the incident light encounters two gratings before fanout.

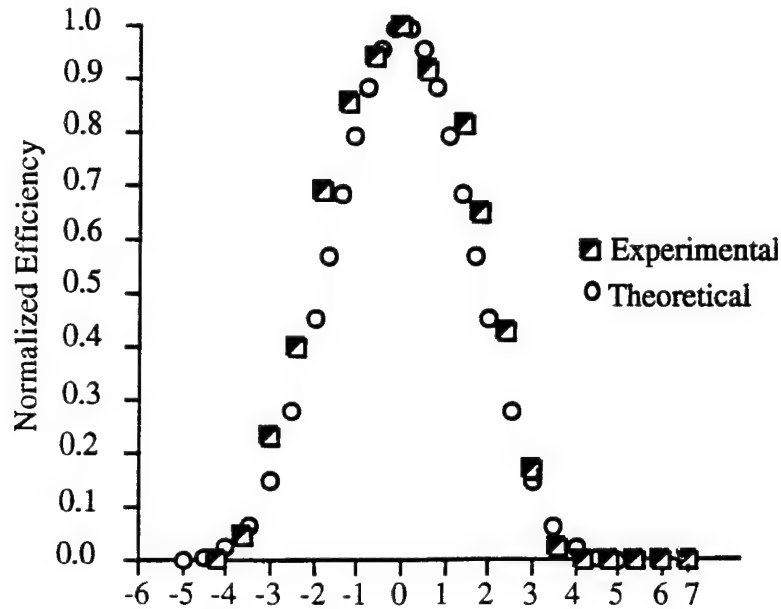


Figure 5-11  
Experimental and Theoretical Plots Showing the Relationship Between Angular Misalignment and Diffraction Efficiency.

In high speed digital optical systems, the active area of a photodetector is inversely proportional to the modulation speed of the signal beam. In our experiment, the radius of the active area is 100  $\mu\text{m}$ . The diffracted beam may traverse upto a radius of the active area of the detector. The beam strikes the center of the detector and then moves along the radius as the input angle  $q$  changes. To determine the relationship between the diffracted beam deviation and the radius of the active area of the detector, as indicated in Figure 5-12, we further derive the following equation:

$$\delta r = 2DN(\tan \phi_1 - \tan \phi_2) \quad (5-20)$$

where  $\delta r$  represents the radius of the active area of the detector, which is 100  $\mu\text{m}$  in our case.  $D = 3000 \mu\text{m}$  (substrate thickness),  $N = 4$  (4th fanout) and  $\phi_1$  is the input diffraction angle, which is  $45^\circ$  in our case. From Eq. (5-20),  $\phi_2$  can be calculated and  $\phi_1 - \phi_2$  shown in Figure 5-12 are the maximum deviation for a detector with an active area radius of 100  $\mu\text{m}$  ( $\phi_1 - \phi_2 = \delta\phi$ ). Figure 5-12 shows the limitation of the detector area size on the maximum deviation of the diffracted beam. The input angular misalignment will cause a shift in the diffraction angle. The shift in diffraction angle (and thus the wavelength deviation) is

$$\delta\phi = -(\cos\theta / n \cos\theta)\delta\theta \quad (5-21)$$

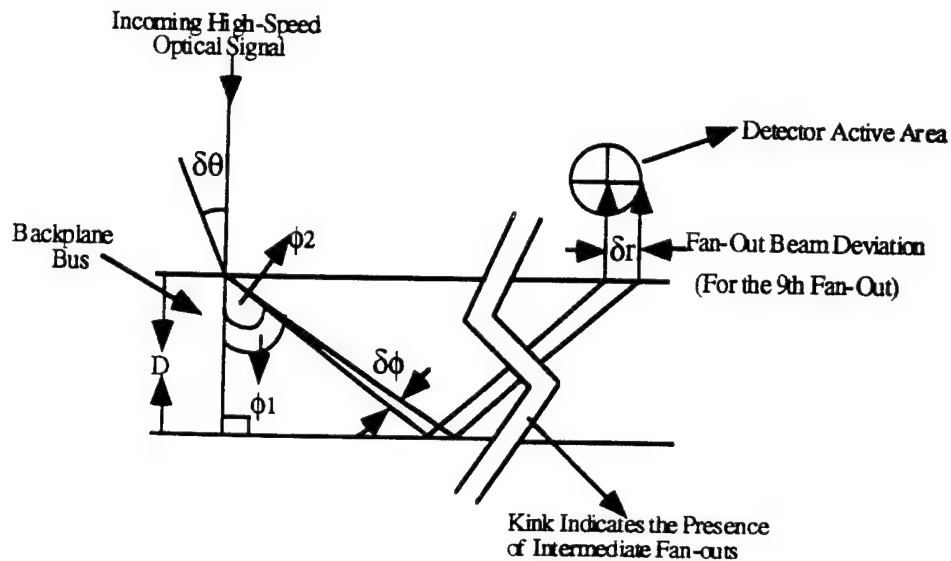


Figure 5-12  
Schematic Showing the Related Parameters for Surface-Normal and Intra-Guiding-Plate Optical Interconnects

The bandwidth coverage caused by the angular shift of TIR beams has been determined to be 5 nm. This clearly indicates that the detector size limits the bandwidth of a system that incorporates the bus, though the bus itself has a bandwidth two orders of magnitude higher. The frequency shift associated with this bandwidth is 0.89 THz.

## 6.0 DEMONSTRATION OF THE MICROPRISM ARRAY-BASED OPTOELECTRONIC INTERCONNECT SYSTEM

As briefly mentioned in Section 3.4, POC has demonstrated the proposed microprism array-based optoelectronic interconnect for the application of video image transmission. In this demonstration, 3 video data sources were used as input channels in an effort to show the crossbar switching capability using the proposed microprism array-based optoelectronic interconnect system. Figure 6-1 shows the schematic diagram of the demonstration system architecture.

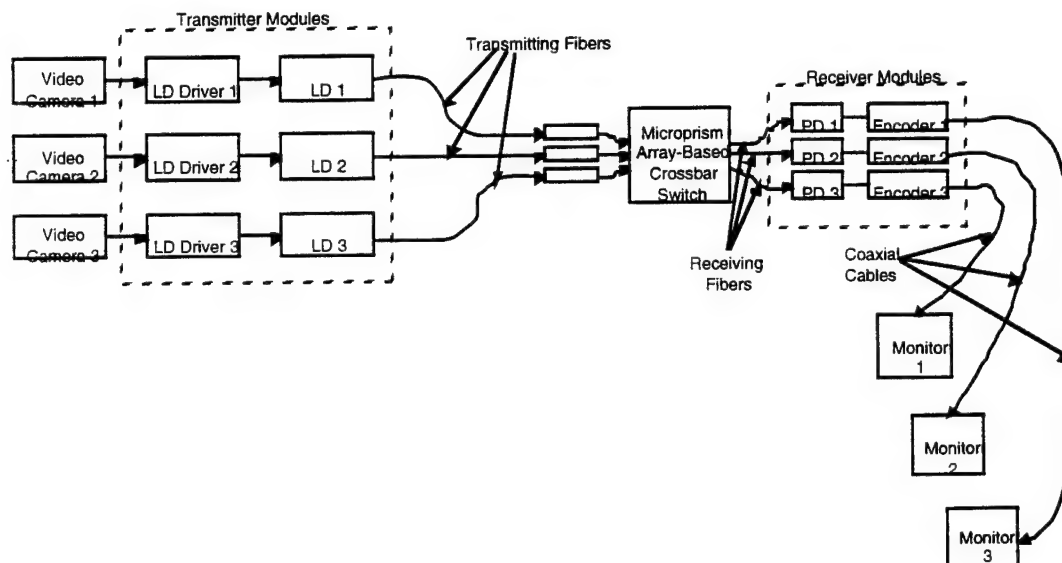


Figure 6-1  
Schematic Diagram of the Demonstration Architecture

## 6.1 Fabrication of the Microprism-Based Optical Crossbar Switch

The core of the demonstration system is the microprism-based optical crossbar switch. In Figure 6-2, schematic diagrams of the microprism-based optical crossbar switch are shown. The major components of the switch are passive optical elements (such as collimating GRIN lenses, holographic gratings, microprisms, and collimating lenses). Liquid crystal is the only active optical element needed to provide the programmability function.

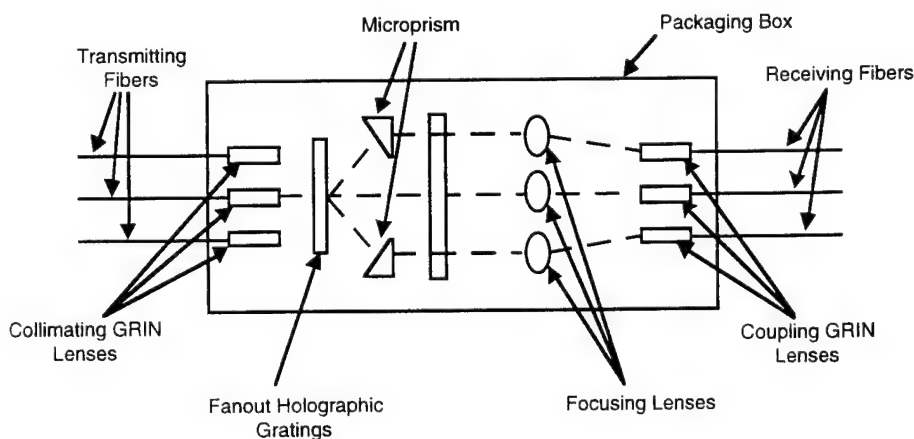


Figure 6-2  
Schematic Diagram of the Microprism-Based Optical Crossbar Switch (Top View)

The experimental demonstration includes video signal delivery and switching. The key component of the system is an all-optical crossbar router based on microprism technology.

The crossbar router can provide non-blocking interconductivity between 3 inputs and 3 outputs, as seen in Figure 6-3.

Figure 6-4 shows the 3x3 optical crossbar switching router. Shown are the input fibers, diffraction, grating micropism, collimating lenses, focusing lenses and the coupling GRIN lens attached to the output fibers.

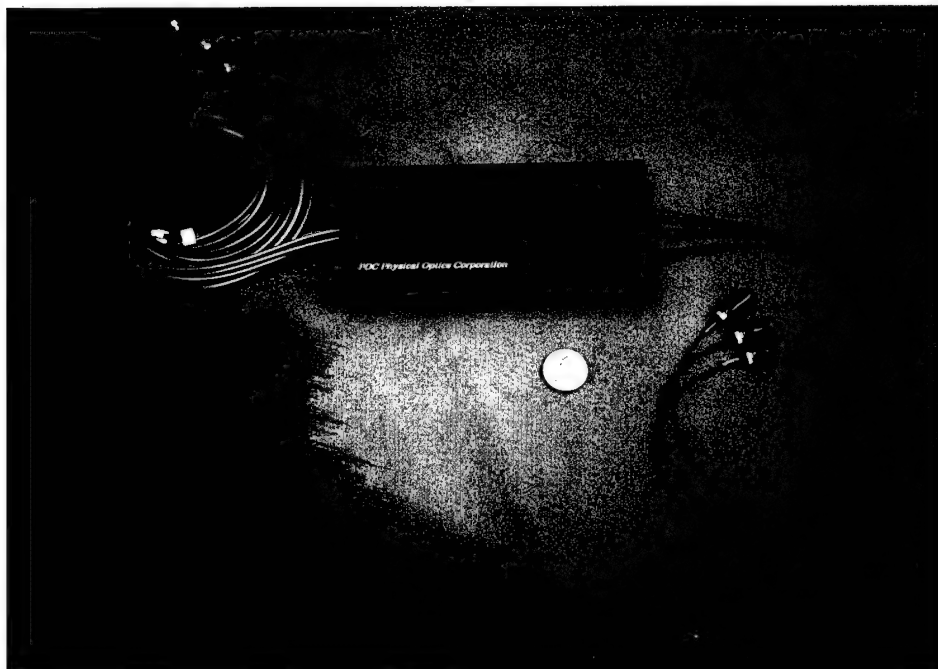


Figure 6-3

Optical Crossbar Router. 3 input fibers (orange) can carry optical information to be rerouted into 3 output fibers (blue). The crossbar router has been thoroughly tested using standard bit-error test measurement.



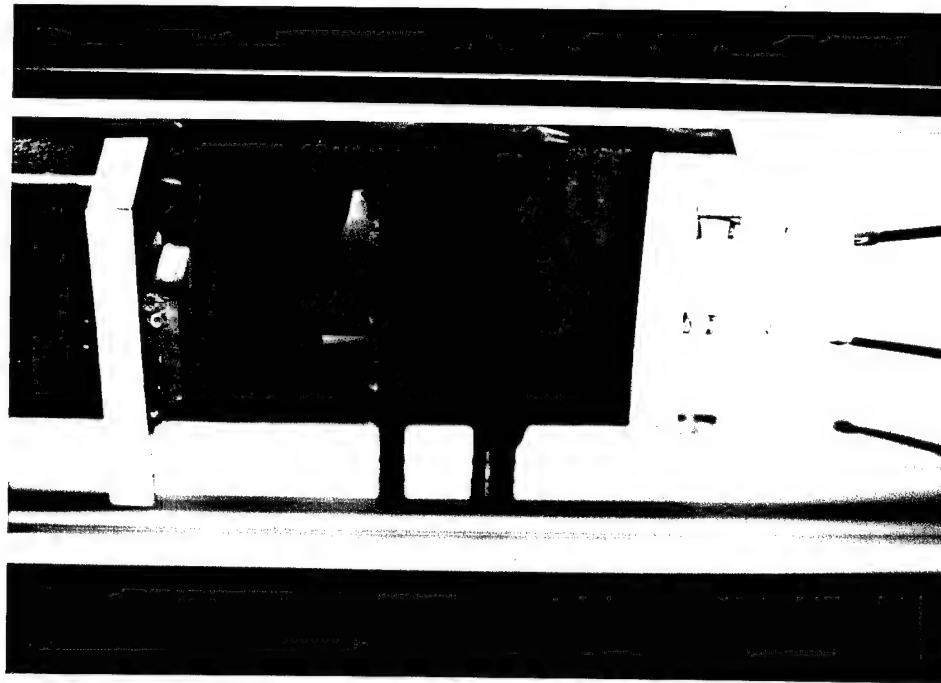


Figure 6-4  
Photograph of the 3x3 Optical Router

The overall crossbar switching mechanism of the fabricated microprism-based optical crossbar switch is as follows:

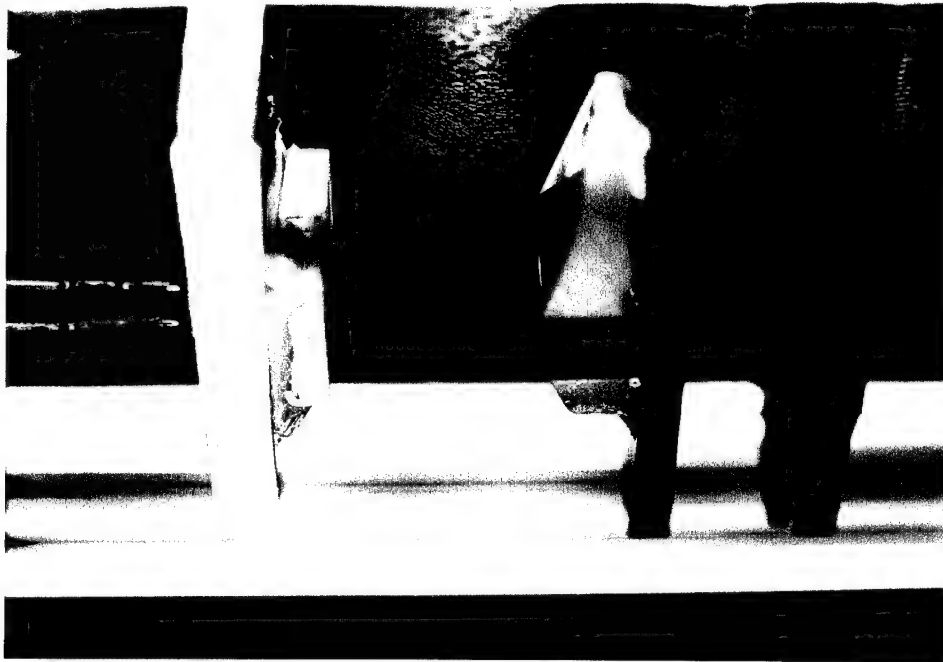
1. A video signal is converted into an optical signal by the transmitter shown in Figure 6-1 and is transmitted to the microprism-based optical crossbar switching system through the transmitting fiber. The core diameter of the fiber is  $62.5\text{ }\mu\text{m}$ .
2. The optical signal is collimated by the collimating GRIN lens. In this stage, the guided and collimated optical signal is converted into collimated free-space optical signals. The transmitting fiber and GRIN lens are attached together using epoxy. The pitch and diameter of the GRIN lens are .25 and 1 mm, respectively.
3. The collimated optical signals pass through the fan-out holographic gratings and split into many duplicated signals. In this case, only the  $0^{\text{th}}$ ,  $-1^{\text{st}}$  and  $1^{\text{st}}$  orders are used, since a 3x3 crossbar switching was demonstrated. The  $0^{\text{th}}$  order passes along the free-space and arrives at the SLM. While the  $1^{\text{st}}$  and  $-1^{\text{st}}$  orders are redirected the corresponding microprism and travels in parallel to the optical axis (the path of the  $0^{\text{th}}$  order). Finally, they are reached at the SLM. The input fibers attached to the diffraction grating are shown Figure 6-5.
4. The SLM provides programmability to the crossbar switch. The overall diagram of the SLM configuration is shown in Figure 6-6.

As shown in Figure 6-6, the SLM contains 9 square-blocks, each block with a unique switching operation based on "on" and "off" operation.

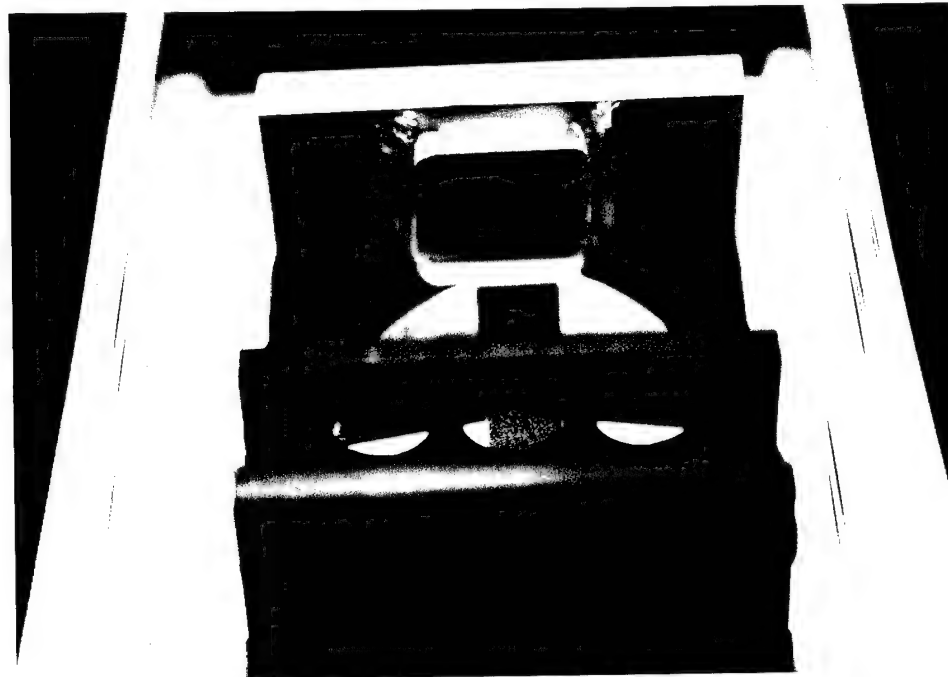
In this program, we used the  $-1^{\text{st}}$  order for output channel 1, the  $0^{\text{th}}$  order for output channel 2, and the  $1^{\text{st}}$  order for output channel 3, respectively. Meanwhile, we assigned the upper left block of the SLM for input channel 1, the upper right block for input channel 2, and the lower middle block for input channel 3.

The ordered pair (a, b) represents the switching configuration, where 'a' represents the input channel and 'b' represents the output channel. For example, if input channel 3 is connected to output channel 3, and input channel 2 is connected to the output channel 1, the configuration of the SLM should be as shown in Figure 6-7(a). In Figure 6-7(b), input channel 2 is simultaneously connected to output channels 1, 2, and 3.

In Figure 6-8, the experimental results of fanout of input channel 2 to output channels 1, 2, and 3 is shown. In the top of the photograph, three points spacing at the same distance are the SLM switching fanout, as shown in Figure 6-7(b)



(a)



(b)

Figure 6-5

(a) Photograph of the input fibers attached to the diffraction gratings; and (b) the three diffractor gratings forratted as the input fibers.

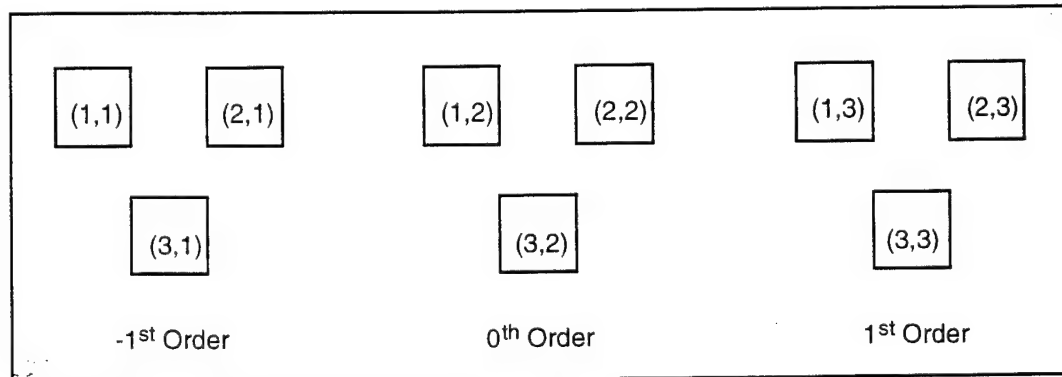
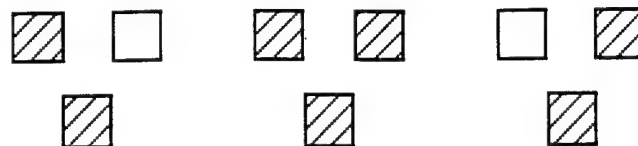
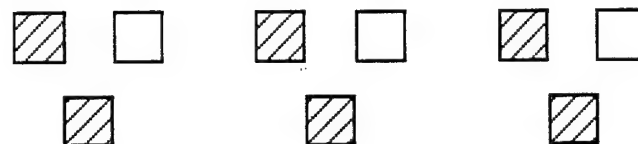


Figure 6-6

The Crossbar Switching Diagram by the SLM



(a)



(b)

Figure 6-7  
SLM Switching Configuration. (a) input channel 1 to output channel 3 and input channel 2 to output channel 1; and (b) input channel 2 to output channels 1, 2, and 3.



Figure 6-8  
Results of Fan-Out Broadcasting Interconnect

5. The optical video signal routed by the SLM is focused by the focusing lens and transmitted to the output coupling GRIN lenses. On the left side of Figure 6-9, the focusing lens together with the SLM switch configuration is shown.

6. Finally, the routed optical video signal is coupled into the output fiber through the coupling GRIN lens, and travels through the output fiber to the receiver, which converts the optical signal back to the electronic video signal. On the right side of Figure 6-9, the output fiber with the coupling GRIN lens is shown.

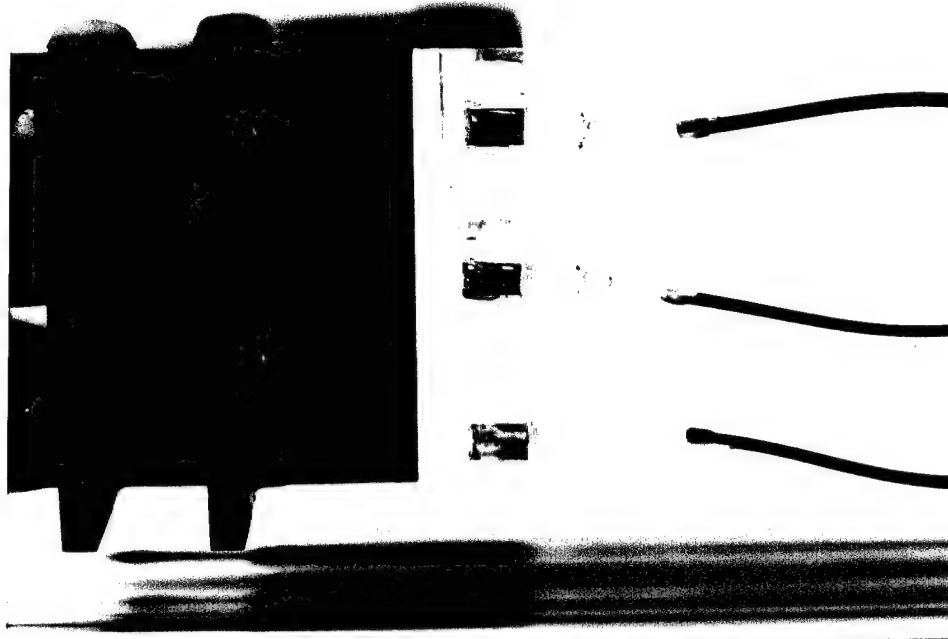


Figure 6-9  
Photograph of the focusing lens with SLM and output fiber attached with coupling GRIN lens.

## 7.0 CONCLUSION

In this program, a microprism-based optical communication/switching system was studied and fabricated. This system successfully resolved the bottlenecks of state-of-the-art electronic board-to-board interconnects, such as wide interconnection time bandwidths, large clock skew, and large RC time constants.

As a result of this two year effort, POC has designed and built electronic transceiver modules, designed on optical interconnect system, designed and demonstrated the bi-directional optical backplanes bus, and finally built and demonstrated a 3x3 microprism-based optical crossbar switch.

## 8.0 REFERENCES

1. M. Fukuma and J. Noda, Appl. Opt., 19, 591 (1980).
2. T. Li, edited by, Topics in Lightwave Transmission Systems, Academic Press, Inc. San Diego, CA (1991).

3. R. Chen, "Polymer-Based Optical Data Bus for Highly Parallel System-Wide Communications," Final Technical Report, Grant No. DE FG03-91-ER81255.
4. K. Lau and A. Yariv, "Gbit/s Rate Bipolar Pulse Modulation of Semiconductor Injection Lasers," *Optics Communications*, Vol. 35, No. 3, pp. 337-341 (December 1980).
5. Y. H. Lo, P. Grabbe, M. Z Iqbal, R. Bhat, J. L. Gimlett, J. C. Young, P. S. D. Lin, A. S. Gozdz, M. A. Koza, and T. P. Lee, "Multigigabit/s 1.5  $\mu\text{m}$   $\lambda/4$ -Shifted DFB OEIC Transmitter and its use in Transmission Experiments," *IEEE Photonics Technology Letters*, Vol. 2, No. 9 (September 1990).
6. F. Bosch, G. Palmer, C. Sallada, and C. Burke Swan, "Compact 1.3 mm Laser Transmitter for the SL Undersea Lightwave System," *Journal of Lightwave Technology*, Vol. LT-2, No. 6, pp. 952-959 (December 1984).
7. A. Husain, T. Lane, C. Sullivan, J. Bristow, and A. Guha, "Optical Backplanes for Massively Parallel Processors and Demonstration in the Connection Machine," Presented at GOMAC, Las Vegas, NV (November 1990).
8. W. Gamboji, A. Weber, and T. Trout, "Advances and Applications of DuPont Holographic Photopolymers," *SPIE Vol. 2043*, pp. 2-13 (1993).
9. S. Tang, and R. Chen, "Surface Normal 1-to-27 Optical Fanout Using Substrate Guided Waves in Conjunction with Two Dimensional Waveguide Hologram Array," *Integrated Photonics Research*, Vol. 3, pp. 277-279 (1994).
10. T. Gaylord and M. Moharam, "Analysis and Applications of Optical Diffraction by Gratings," *Proc. IEEE* 73, 840 (1985).
11. E. Pinney and D. McWilliams, Management Science: An Introduction to Quantitative Analysis for Management, Harper & Row Publishers, New York, NY (1982).
12. A. Yariv, Introduction to Optical Electronics, 2nd edition, McGraw-Hill, New York, NY (1976).
13. C. Zhao, R. Chen, and S. Natarajan, "System Power Budget Considerations of Backplane Bus with High Speed Cascaded Broadcasting," presented at the 1995 SPIE Conference on Optoelectronic Interconnects.

## APPENDIX A

### Fresnel Number and Aperture Diffraction

In general, the aperture diffraction can be ignored when the Fresnel number,  $F$ , is much larger than unity. The Fresnel number is

$$F = \frac{kr^2}{2z} \quad (A-1)$$

where  $r$  is aperture radius,  $z$  is distance and  $\lambda$  is wavelength. Thus, the above condition has the following approximate form

$$\frac{r^2}{\lambda z} \geq 10 \quad (A-2)$$

For equality in Eq. (A-2)

$$z = z_0 = \frac{D^2}{10\lambda} \quad (A-3)$$

i.e., assuming  $l$  and  $r$  are fixed, for  $z > z_0$  the aperture diffraction effects are significant. Let us assume  $\lambda = 1\mu$ , then  $z_0 = 100 r^2$  [mm]. This is illustrated in the table below

$r$ [mm]	0.1	0.5	1.0	10	$10^3$
$z_0$	1 mm	2.5 cm	10 cm	10 m	100 km

We can see that the aperture diffraction effects are significant for very small apertures (on the order of 1 mm). This is the case of fiber-optic/free-space interconnects.

## APPENDIX B

### Integral Transformation for Poynting Vector in Geometrical Optics

Many problems in geometrical optics are related to ray-tracing and energy density formalism. Hence, the integral transformation for Poynting vector is important. We can see that such a transformation is automatically used in the ray-tracing formalism. Let us consider a quasi-homogenous planar source in a plane  $z = 0$ , and observation plane  $z > 0$ ;  $\vec{r}$  and  $\vec{r}_0$  are 2D position vectors located in planes  $z > 0$ , and  $z = 0$ , respectively. Hence, according to Figure B-1, the position vector  $\vec{R}$  has the form

$$\begin{aligned}\vec{R} &= \vec{r} + \hat{n}z \\ \vec{R}_0 &= \vec{r}_0\end{aligned}\tag{B-1}$$

where  $\hat{n}$  is the unit vector parallel to  $z$ -axis.

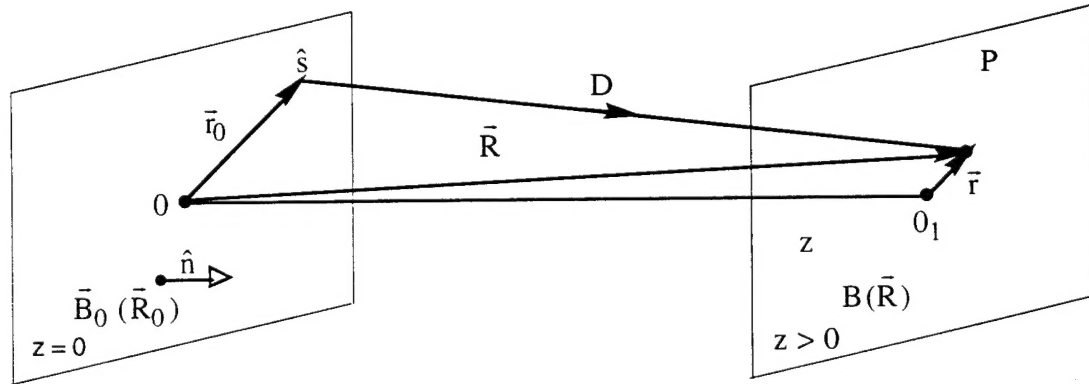


Figure B-1  
Geometry of the Problem

According to basic definitions in radiometry

$$\vec{S}(\vec{R}) = \int B(\vec{R}, \hat{s}) \hat{s} d\Omega\tag{B-1}$$

where  $\hat{s}$  is unit vector of observation and  $d\Omega$  is solid angle element. According to the basic law of radiometry

$$B(\vec{R}, \vec{s}) = B_0(\vec{R} - D\hat{s}, \hat{s})\tag{B-2}$$

where  $D$  is distance between the equivalent points. To compute  $D$ , we write the simple identity  $\vec{r}_0 \cdot \hat{n} = 0$ , or

$$(\vec{R} - D\hat{s}) \cdot \hat{n} = 0\tag{B-3}$$

hence



$$D = \frac{\bar{\mathbf{R}} \cdot \hat{\mathbf{n}}}{\hat{\mathbf{s}} \cdot \hat{\mathbf{n}}} \quad (\text{B-4})$$

and Eq. (B-2) can be rewritten in the form

$$B(\bar{\mathbf{R}}, \hat{\mathbf{s}}) = B_0 \left( \bar{\mathbf{R}} - \frac{\hat{\mathbf{s}} (\bar{\mathbf{R}} \cdot \hat{\mathbf{n}})}{\hat{\mathbf{s}} \cdot \hat{\mathbf{n}}} \right) \quad (\text{B-5})$$

hence instead of Eq. (B-1), we have

$$\bar{\mathbf{S}}(\bar{\mathbf{R}}) = \int B_0 \left[ \bar{\mathbf{R}} - \frac{\hat{\mathbf{s}} (\bar{\mathbf{R}} \cdot \hat{\mathbf{n}})}{\hat{\mathbf{s}} \cdot \hat{\mathbf{n}}}, \hat{\mathbf{s}} \right] \hat{\mathbf{s}} d\Omega \quad (\text{B-6})$$

Additionally, for emittance  $E$ , or  $z$ -component of Poynting vector, we have

$$E = S_z = \bar{\mathbf{S}} \cdot \hat{\mathbf{n}} = \int B_0 \left[ \bar{\mathbf{R}} - \frac{\hat{\mathbf{s}} (\bar{\mathbf{R}} \cdot \hat{\mathbf{n}})}{\hat{\mathbf{s}} \cdot \hat{\mathbf{n}}}, \hat{\mathbf{s}} \right] \cos \theta d\Omega \quad (\text{B-7})$$

where  $\cos \theta = \hat{\mathbf{n}} \cdot \hat{\mathbf{s}}$ . Also, because of

$$ds_x ds_y = \cos \theta d\Omega \quad (\text{B-8})$$

we have the third version of basic formula

$$E(\bar{\mathbf{R}}) = \int B_0 \left[ \bar{\mathbf{R}} - \frac{\hat{\mathbf{s}} (\bar{\mathbf{R}} \cdot \hat{\mathbf{n}})}{\hat{\mathbf{s}} \cdot \hat{\mathbf{n}}}, \hat{\mathbf{s}} \right] ds_x ds_y \quad (\text{B-9})$$

This formula has been used intuitively during ray-tracing, in the case of a Labertian source ( $B_0 = \text{const.}$ ). However, the general formula is necessary, for example, in the case of horizontally-non-uniform sources (including holograms).

The validity of formulas (B-6), (B-7), or (B-9) holds for the condition:

$$H = \frac{z}{\lambda} \left( \frac{\lambda}{\delta} \right)^2 \ll 1 \quad (\text{B-10})$$

where  $z$  is the distance between the source and observation planes,  $\delta$  is sthesize of the smallest detail of the planar source intensity non-uniformities, and  $\lambda$  is the wavelength.

For  $\lambda = 1 \mu\text{m}$ ,  $\delta = 1 \text{ mm}$ , and  $z = 10 \text{ cm}$ , we obtain  $H = 10^{-1}$ , i.e., acceptable distances are on the order of 10 cm.